Modelling and Operation of Diesel Engine Exhaust Gas Cleaning Systems

Åberg, Andreas

Publication date:
2017

Document Version
Publisher's PDF, also known as Version of record

Modelling and Operation of Diesel Engine Exhaust Gas Cleaning Systems

Andreas Åberg

PhD Thesis

January 2017

DTU Chemical Engineering
Department of Chemical and Biochemical Engineering

Technical University of Denmark

PhD Thesis

Modelling and Operation of Diesel Engine Exhaust Gas Cleaning Systems

Andreas Åberg

2017-01-31

DTU Chemical Engineering
Department of Chemical and Biochemical Engineering

Technical University of Denmark
Anker Engelundsvej 1
Building 101A
DK-2800, Kgs. Lyngby
Denmark
CVR-nr. 30 06 09 46
Phone: (+45) 45 25 25 25
Email: dtu@dtu.dk
www.dtu.dk

Printed by GraphicCo

Preface

This thesis is submitted as a partial fulfilment of the requirements for obtaining a Doctor of Philosophy (PhD) degree at the Technical University of Denmark. The PhD project has been conducted at the CAPEC-PROCESS Research Centre at the Department of Chemical and Biochemical Engineering, under the supervision of Associate Professor Jakob Kjøbsted Huusom and Associate Professor Jens Abildskov from DTU, and Dr. Anders Widd from Haldor Topsoe A/S.

The journey towards a PhD is certainly a very special experience that includes many challenges, but is also rewarding on many levels. The people I would like to thank for helping me reach the end of the project are too many to mention here, so I will have to make do with a special few. I would first of all like to thank my supervisors, Jakob and Jens. I am very grateful to have had such excellent support throughout the project, and our weekly meetings and discussions has certainly increased the quality of the work. I would also like to thank Anders, for making time for me and really being a part of the project. Without his input and our discussions I am certain that the project would have been less successful.

The collaboration with Haldor Topsoe A/S has made it possible for me to use experimental data and conduct engine tests that has improved the quality of the work in ways that were not possible without the collaboration. For this, the organisers of the NEXT project deserves a special thanks.

The collaboration between the PhD students in the NEXT project, of which I have been part, has been valuable professionally, but even more so socially. I would therefore like to thank Kasper, Thomas, and Ian, who I hope I will remain in contact with wherever we end up after the PhD. A special thanks goes to Kasper for always having time for one of our productive meetings, discussing results and the steps ahead.

A large part of the success of a PhD project comes down to the day-to-day office environment, which is an area where I have had unusual luck. I would like to thank all colleagues in CAPEC-PROCESS for providing a friendly working environment. A special thanks goes to both former and current office mates Thomas, Hannah, and Lukazs. Going to the office has been a pleasure even during challenging periods.

Finally I would like to thank my family, who has always been supporting me in my studies.

Andreas Åberg
Kgs. Lyngby, 2017

Summary

Diesel engine exhaust gases contain several harmful substances. The main pollutants are carbon monoxide (CO), hydrocarbons (HC), particulate matter (PM), and nitrous gases such as nitrogen oxide (NO) and nitrogen dioxide (NO_2) (together NO_x). Reducing the emission of these pollutants is of great importance due to their effect on urban air quality, and because of new legislation. In modern heavy-duty applications, the exhaust gases are typically treated with four different catalysts: a Diesel Oxidation Catalyst (DOC) which oxidises HC and CO into H_2O and CO_2, and NO into NO_2, a Diesel Particulate Filter (DPF) which filters PM, a Selective Catalytic Reduction (SCR) catalyst which removes NO and NO_2 through reaction with NH_3, and an Ammonia Slip Catalyst (ASC) which removes excess ammonia (NH_3) before the gases are released to the atmosphere.

SCR is a widely used technology to reduce NOx to N_2. Challenges with this technology include dosing the appropriate amount of urea to reach sufficient NO_x conversion, while at the same time keeping NH_3- slip from the exhaust system below the legislation. This requires efficient control algorithms.

The focus of this thesis is modelling and control of the SCR catalyst. A single channel model for a heavy-duty SCR catalyst was derived based on first principles. The model considered heat and mass transfer between the channel gas phase and the wash coat phase. Four simplified models were derived, with simplifications related to mass and heat transfer. The model parameters were estimated using bench-scale monolith isothermal data. Validation was done by simulating the output from a full-scale SCR monolith that was treating real engine gases from the European Transient Cycle (ETC). Results showed that the models were successfully calibrated, and that some of the models could predict the ETC output satisfactorily. The models' predictive capabilities were investigated in relation to the simplifica-

tions, and results showed that the simplifications related to mass transfer resulted in the smallest information loss.

A methodology to analyse the NOx-NH_3 trade-off for different urea dosing controllers was developed, and applied to P, PI, PD, and PID controllers, both with and without Ammonia-NOx-Ratio (ANR) based feedforward. Simulation results showed that the PI controller with feedforward had the best NOx-NH_3 trade-off, and that feedforward coupled with feedback outperformed the other control structures. The results were experimentally verified by implementing the tested controllers on a full-scale engine setup, and the results showed that coupling feedback with ANR based feedforward was yielding better performance. The PD controller showed good performance in the experimental validation.

Finally, a methodology for creating a modular simulation tool was developed. The methodology goes through the steps that are required to integrate individual models so that they can be used for the tool. The methodology is demonstrated by applying it to four models from literature, and simulating the system.

Resumé

Dieselmotorers udstødningsgasser indeholder flere skadelige stoffer. De vigtigste forurenende stoffer er kulilte (CO), kulbrinter (HC), partikler (PM), og nitrøse gasser såsom nitrogenoxid (NO) og kvælstofdioxid (NO_2) (sammen NOx). Reduktion af emissionen af disse forudenende stoffer er af stor betydning på grund af dered indvirkning på luftkvaliteten i byerne, og på grund af ny lovgivning. I moderne tunge applikationer, er udstødningsgasserne behandles typisk med fire forskellige katalysatorer: en Diesel oxidationskatalysator (DOC), som oxidered HC og CO i H_2O og CO_2, og NO i NO_2, en dieselpartikelfilter (DPF), som filtrerer PM, en Selective Catalytic Reduction (SCR) katalysator, som fjerner NO og NO_2 ved reaktion med NH_3, og en Ammoniak Slip Catalyst (ASC) som fjerner overskydende ammoniak (NH_3), før gasserne frigives til atmosfæren.

En udbredte teknologi til fjernelse af NOx er baseret på SCR. Udfordringer med denne teknologi omfatter dosering med passende mængde urinstof for at nå tilstrækkelig NOx konvertering, mens på samme tid at holde NH_3 slip ud fra systemet under lovgivningen. Dette kræver en effektiv kontrol algoritme.

Fokus for denne afhandling er modellering og kontrol af SCR-katalysatorn. En enkelt kanal model for en SCR katalysator blev udledt på basis af de grundlæggende principper. Modellen anser varme- og masseoverførsel mellem kanalen gasfase og solid fase. Fire forenklede modeller blev afledt, med forenklinger relateret til masse og varmeoverførsel. Modellens parametre blev estimeret ved hjælp af bench-skala monolit isotermiske data. Validering blev udført ved at simulere output fra en fuld skala SCR monolit, der var at behandle reelle motor gasser fra European Transient Cycle (ETC). Resultaterne viste, at modellerne blev kalibreret med succes, og at nogle af modellerne kunne forudse ETC output tilfredsstillende. Modellernes prædiktive kapaciteter blev undersøgt i forhold til de forenklinger, og resultaterne

viste, at de forenklinger, relateret til massetransport resulterede i den mindste informations tab.

En metode til at analysere NOx-NH_3 trade-off for forskellige urinstof dosering controllere er blevet præsenteret, og anvendt på P, PI, PD, og PID regulatorer, både med og uden ANF baseret feedforward. Simulations resultaterne viste, at PI controller med feedforward havde den bedste NOx-NH_3 trade-off, og at feedforward kombineret med feedback udkonkurrerede at kun bruge ANF baseret feedforward. Resultaterne blev eksperimentelt verificeret ved at bruge de testede regulator på en fuldskala motor setup, og resultaterne viste, at feedback med ANF baseret feedforward stadig klarer sig bedre. PD regulatorn viste gode resultater i den eksperimentelle validering.

Endelig er en metode til at skabe et modulært simuleringsværktøj blevet fremlagt. Metodologien går gennem de trin, der kræves for at integrere enkelte modeller, så de kan anvendes til værktøjet. Metoden demonstreres ved at anvende det til fire modeller fra litteraturen, og simulering af systemet.

Contents

Chapter 1

Thesis Introduction and Overview

This chapter presents an introduction and overview of the thesis. It focuses on the background of the automotive diesel engine, and presents the contributions and motivates why the work is needed. An overview of the diesel engine and the automotive exhaust gas cleaning system is presented, together with some of the current challenges in the field. The objective of the thesis, an outline and publications during the project are presented.

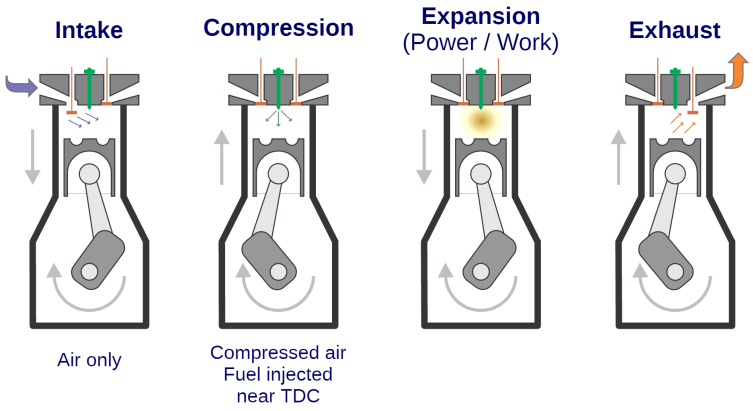

Figure 1.1. The four steps of a four-stroke diesel engine. Figure from [91]

1.1 Background and Motivation

This section will give a background on the diesel engine and its emissions. The exhaust gas aftertreatment system will be presented as well.

1.1.1 Diesel Engine Fundamentals

The diesel engine is an internal combustion engine first developed in the end of the 19th century. An internal combustion engine uses the products of combustion of a fuel-air mixture as the working fluid. Two main types of internal combustion engines exists, the spark-ignition engine and the compression-ignition engine. The diesel engine belongs to the compression-ignited engines.

The definition of a diesel engine has changed as the engine developed. One of the first definitions was based on Purdays definition[99], and while the first step of the definition still holds true today, the rest are not necessarily true. Today different sorts of diesel engines exists. Two of the major classifications are two-stroke cycle or four-stroke cycle. The four-stroke cycle is by far the most common, and two-stroke engines are mainly used in naval applications. The four stroke diesel steps can be seen in Figure 1.1.

As the name suggests, the four-stroke engine requires four strokes to complete a cycle. The first stroke is the intake stroke, where the cylinder is filled with air as the piston moves down. In the second stroke the air is compressed to a temperature that is higher than the auto-ignotion temperature of the fuel that is used. If the fuel is injected at the end of the compression stage directly into the cylinder, the engine is operating with what is called direct injection. If the fuel has been injected

into a pre-chamber connected to the cylinder, the engine is operating according to indirect injection, since the fuel is not injected directly into the main combustion chamber. In indirect injection the combustion typically starts in the pre-chamber, where the fuel is mixed with the air. Direct injection however normally has a much higher thermal efficiency. In the third stroke, the fuel is ignited and the piston is forced to move due to the explosion. This is the stage where work is extracted from the engine. In the fourth and final stroke, the exhaust gases from the combustion is evacuated from the cylinder [91]. The composition of the exhaust gases will be explained in Section 1.1.2.

1.1.2 Diesel Engine Emissions

During the combustion of the diesel fuel several emissions are formed, some more harmful than others. The majority of the produced gas is made up of CO_2, which accounts for around 2-12%, H_2O, which accounts for around 2-12%, O_2 around 3-17%, and N_2 from the intake air to balance. The emissions of these substances is normally unregulated, with the exception of CO_2, because of its global warming potential. With regards to minimizing CO_2, the diesel engine plays an important role due to its higher efficiency compared to a petrol engine. Figure 1.2 shows a comparison between emitted CO_2 for passenger cars by weight for diesel and petrol engines following the New European Driving Cycle (NEDC), according to the European Environment Agency (EEA). It can be noted that as the weight of the cars increases, the advantage of using diesel increases. The same is true for heavy-duty applications, the motivation for using diesel in the heavy applications becomes clear, from a CO_2 point-of-view. The lower CO_2 emissions and higher thermal efficiency for diesel has also been reported by Schindler [108].

Besides the major exhaust gas components presented previously, a number of both regulated and unregulated pollutants appear as a results of the combustion. The most commonly regulated pollutants are carbon monoxide (CO), hydrocarbons (HC), particulate matter (PM), and nitrous gases such as nitrogen oxide (NO) and nitrogen dioxide (NO_2) (together NO_x) [126]. Reducing the emission of these pollutants is of great importance due to their effect on urban air quality, and because of new legislation [39, 47], which will be discussed in Section 1.1.2.1. The health effects of these different substances are to some extent known, for example particulate matter has been shown to be carcinogenic [1]. Some of the well known health effects has been reported by the Health Effects Institute[1]: CO is highly toxic to humans since it blocks oxygen uptake. Nitrogen oxides is a precursor to ozone, and

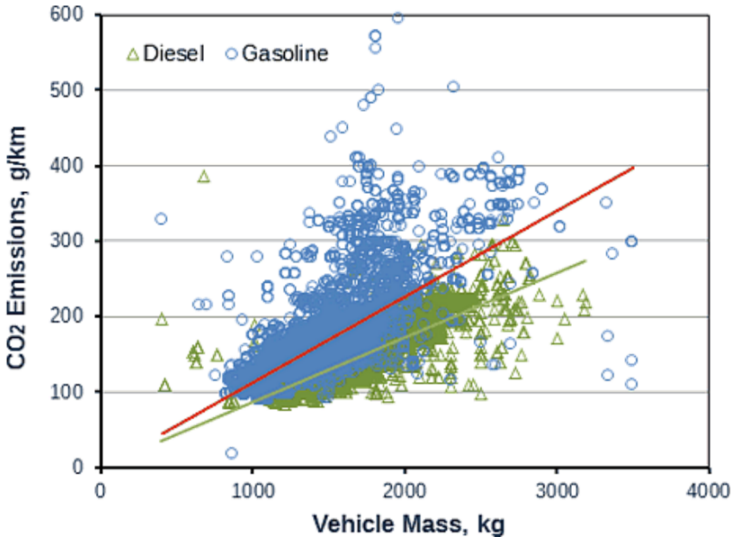

Figure 1.2. Comparison of CO_2 emissions from gasoline and diesel engines during NEDC during 2013 by EEA. Figure from [91]

is a respiratory tract irritant. The nitrogen oxide can react into nitric acid, which causes acid rain. HCs is a broad group of organic compounds, however some of the effects include it being a respiratory tract irritant. The lower order alkanes are a precursor to ozone, and some higher order alkenes are carcinogenic.

Due to the relatively undefined chemical composition of diesel fuel, the amount of unregulated emissions is long. Examples are sulfur oxides, soluble organics, aldehydes, formaldehyde, and phosphorus [126]. Depending on the lubricant oil that is used, the list of chemicals appearing in the exhaust gases can be more or less extensive [2].

1.1.2.1 Legislation

To reduce the amount of harmful pollutants, governments has been introducing stricter legislation for emission limits over time. Figure 1.3 shows the evolution of the European emission standards for heavy-duty diesel trucks, which has been delivered in the Euro packages [24]. The latest and current emission standard is the Euro VI, which was put into effect 2013. As can be seen, the emission levels for especially NOx has been reduced dramatically since the introduction, requiring truck manufacturers to be increasingly innovative in their solutions. Unique for the Euro VI emission standard is that it also includes limits for the Particulate Number

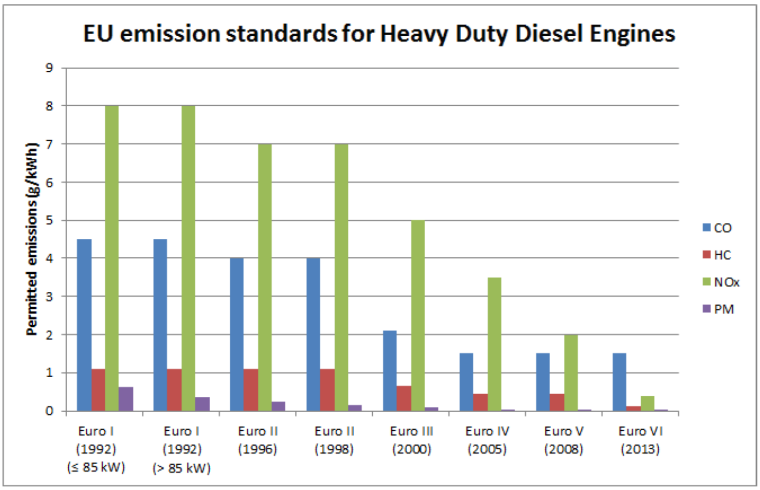

Figure 1.3. Development of the European mission standards for CO, HC, NOx, and PM, for heavy-duty diesel engines.

(PN). Limits has also been introduced on NH_3, which is added to the system in order to remove NOx. This will be explained more in detail in Section 1.1.3.

To pass the emission standards, truck manufacturers has to prove that their exhaust system fulfils the emission limits in different tests. These test can be both of a steady-state nature and transient nature. The transient test levels that has to be passed are naturally slightly higher than the steady-state levels, however since a truck driving on a road normally has to stop for red lights, encounters traffic, hills, and different speed limits, the transient tests likely presents a more realistic driving scenario than the steady-state tests. The work in this thesis will mostly focus on simulating transient tests, which therefore requires a dynamic model. For Euro VI, the World Harmonized Transient Cycle (WHTC) is the transient cycle that defines the emission limits, and for Euro III to Euro V, the European Transient Cycle (ETC) [32] was the cycle for transient tests. The ETC is divided into three sections that each represents different driving conditions; urban, rural, and motorway. The urban section represents city driving with a maximum speed of 50 km/h, with frequent starts, stops, and idling. The rural section includes a steep acceleration, and has an average speed of 72 km/h. The motorway section is the least transient section, and has an average speed of 88 km/h [32].

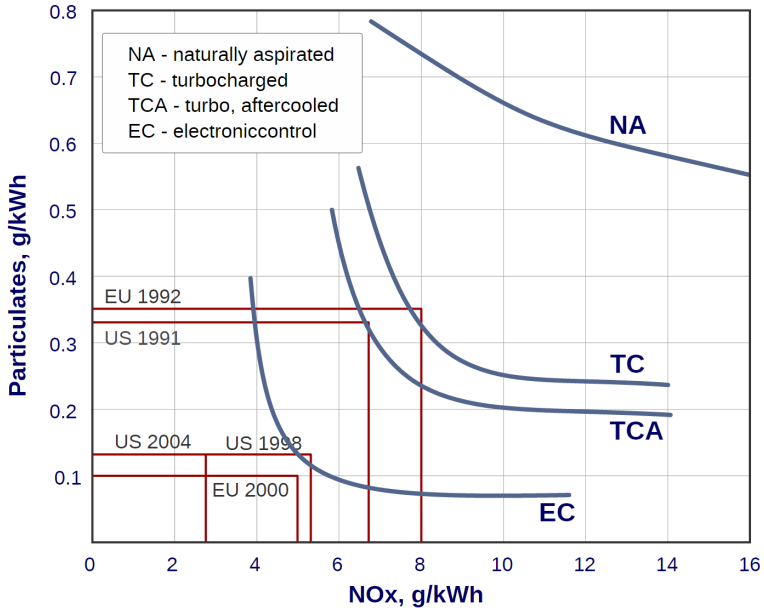

Figure 1.4. Trade-off between NOx and PM for different engine modifications, in comparison with the level for some emission standards. Figure from: [92]

1.1.3 Reducing the Amount of Pollutants

To reach the emission levels described in Section 1.1.2.1, truck manufacturers has implemented several methods. One possible solution is engine modification and optimisation. Engine design parameters that has improved overall emission limits are for example fuel injection timing [57], increased fuel injection pressure [119], and turbo charging [9]. Several of these methods can be combined under the concept of engine control [16].

The simultaneous minimisation of NOx and PM is made difficult by the NOx-PM trade-off. An increased combustion temperature has a tendency to produce more NOx, due to the reaction that combines the N_2 with O_2 becoming more prominent, while at the same time decreasing PM levels because of a more complete combustion. One way to control this is by Exhaust Gas Recirculation (EGR) [4, 141, 54], in which a portion of the exhaust gases are recirculated and mixed with the engine intake air. Increasing the EGR decreases the peak burned gas temperature, and reduces NOx at the cost of increased PM [49]. The NOx-PM trade-off can be seen in Figure 1.4, which also shows how different engine technologies has reduced the trade-off.

As seen, as emission standards became stricter, the need for additional methods

to reduce tail pipe emissions was increased, which is why the catalytic exhaust gas treatment system was developed. The three-way catalyst that was highly successful with gasoline engines is not suitable with diesel applications due to its lean burning conditions, meaning that it operates with high air/fuel conditions [11]. Instead, new catalytic systems has been developed, and a typical Euro VI based exhaust gas treatment system can be seen in Figure 1.5. In a modern EU VI exhaust gas treatment system for heavy duty diesel applications, the exhaust gases are typically treated with four different catalysts: a Diesel Oxidation Catalyst (DOC) which oxidises HC and CO into H_2O and CO_2, and NO into NO_2, a Diesel Particulate Filter (DPF) which filters PM, a Selective Catalytic Reduction (SCR) catalyst which reduces NO and NO_2 to N_2, and an Ammonia Slip Catalyst (ASC) which removes excess ammonia (NH_3) before the gases are released to the atmosphere. The catalytic units are often based on a ceramic honeycomb monolithic substrate, that includes many parallel channels running in the axial direction. The support material lacks catalytic activity, and the catalytic material is coated on the monolith walls. The use of monolith based catalysts has several advantages, such as relatively low pressure drop, and thus a low impact on fuel economy. The exception is the DPF, which typically has a wall-flow design to entrain the soot particulates, thus increasing pressure drop. Disadvantages with depending on a catalyst to meet emission standards are for example that they are highly dependent on temperature. At engine start-up conditions, the catalytic system is cold and ineffective. The catalyst can be deactivated over time from poisoning. For example sulphur has been shown to decrease activity over time. The catalyst can also introduce undesired reactions, thereby forming chemical compounds that would otherwise not have been present.

The focus of this work is related to the removal of NOx. A promising and widely used technology for removing NOx is based on SCR, with NH_3 in the form of hydrolyzed urea as a reducing agent [65, 128, 41]. Challenges with this technology include dosing the appropriate amount of urea to reach sufficient NO_x conversion, while at the same time keeping NH_3- slip from the exhaust system below the legislative limit. As can be seen in Figure 1.5, the injection of urea to the SCR catalyst is the only location in the exhaust system where a control action is possible. The development of models and control algorithms is therefore a crucial part in meeting the legislative limits.

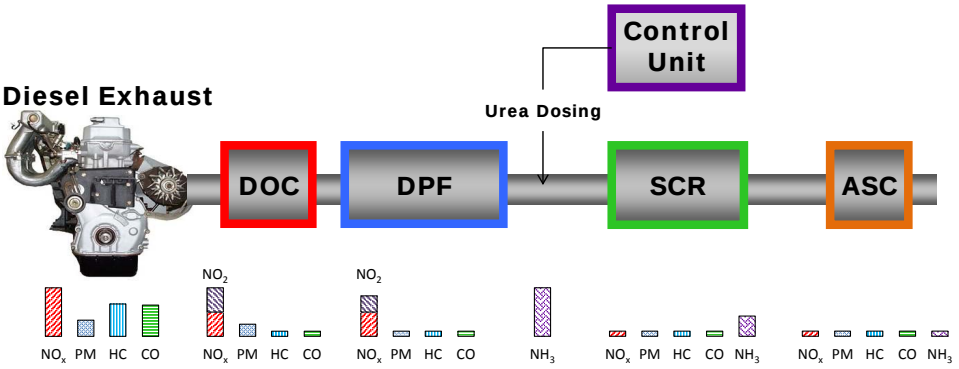

Figure 1.5. The standard Euro VI diesel engine exhaust gas cleaning system. The bars below the catalysts represent the effect each catalyst has on the composition of the exhaust gases.

1.2 Objectives

The area of automotive SCR technology is a rapidly expanding research topic due to new increasingly tough legislation being implemented world wide on a regular basis. Theoretical work related to modelling and control of the SCR catalyst is a well studied subject in literature, however there are areas that still requires additional research to gain insight. For example, one area that to our knowledge requires additional insight is how the structure and complexity of the monolith channel model affects its predictive performance, specifically related to simplifications on the mass and energy balances. In state estimation and model based control it is of high importance that the models are kept as simple as possible if they are to be fast enough to be used in the real application. Overly complicated simulation models can result in situations where model parameters are uncertain and the increased complexity does not improve the model prediction, but rather only increase simulation time.

Kinetic model calibration is another subject that requires additional insight. Robust model calibration that does not depend on overly complicated experimental data, and still results in accurate kinetic parameters, is of high importance in order to decrease experimental effort. There are also situations where the available data is not ideal, meaning that calibration methodologies has to be able to cope with this.

The area of most importance for the performance of the SCR catalyst, besides the catalytic material, is the urea dosing strategy. In literature many innovative control strategies has been developed, from structurally simple feedback controllers

to complex Model Based Control (MPC). Contributions in literature often focus on optimising a single control structure for a given system, rather than a full analysis of how different control structures can improve the performance of the SCR catalyst.

The above will be handled by working on the following topics:

1. **Modelling:** A model based on first principles will be developed for a SCR monolith provided by Haldor Topsoe A/S. The model should include enough physical phenomena that it can accurately describe the dynamics of a transient test cycle. Additional simplified models should be derived based on the first model. The simplifications should be related to the channel model physics.

2. **Calibration:** A kinetic model should be calibrated together with the developed channel models using experimental data from a small scale monolith supplied by Haldor Topsoe A/S. The methodology should produce kinetic parameters that accurately predict the behaviour of the SCR monolith.

3. **Validation:** The channel models together with the kinetic model should be validated. This should be done by simulating the European Transient Cycle (ETC). The model output should be compared with experimental data from a full-scale SCR monolith. The monolith should be treating real engine gases.

4. **Model Analysis:** The predictive performance of the different models should be analysed using appropriate methods. To achieve information about both the importance of the physical phenomena, and the kinetic parameters, the models should first be analysed using the same kinetic parameters, from one of the calibrations. The analysis should also be done with kinetic parameters unique to each model.

5. **Control:** A methodology should be developed that allows the user to graphically analyse the performance of different control structures. The methodology will be applied by testing relatively simple feedback controllers, such as P, PI, PD, and PID. Feedforward based controllers should also be tested. The analysis will thus both include a methodology that is generic for analysing controllers, and be a comprehensive analysis of the performance of some simple controllers that are common in industry.

1.3 Outline

The thesis is divided into chapters with the following content:

Chapter 2 - Overview of the SCR Technology: A literature review of the SCR technology is presented. The reactions that are typical for the SCR catalyst are presented. Special focus is given to previous channel modelling of the SCR monolith, with both a historical overview of early work, as well as recent publications. The problem of calibrating and validating the SCR monolith models is also investigated, and methodologies that has been used previously are presented. An overview of previous work of controlling the urea dosing is also given.

Chapter 3 - Modelling the SCR Monolith: The model that contains the least simplifications in this thesis is derived in full. Based on this, four other models, that include simplifications related to the mass and energy balances are derived. The kinetic model that has been adopted from literature is presented. The methodologies used to implement and solve the models are presented and exemplified.

Chapter 4 - Estimation of Kinetic Parameters for the SCR Catalyst: The kinetic parameters related to the kinetic model are calibrated using a sequential parameter estimation methodology. The small-scale monolith experimental data that has been used for calibration is presented and discussed. The results are analysed and conclusions are drawn related to the different model simplifications.

Chapter 5 - Validation of the SCR Monolith Models: The calibrated models are validated using full-scale engine data following the European Transient Cycle (ETC), and the results are analysed.

Chapter 6 - Analysis of the SCR Monolith Models: The validated models are analysed with respect to their predictive performance of a full-scale ETC cycle. The models are analysed with regards to predicting the NOx monolith output, both using the kinetic parameters of one of the models, and kinetic parameters specific to each model. The time it takes to simulate the ETC cycle is analysed for the different models, and related to their complexity.

Chapter 7 - Controlling the Urea Dosing: A methodology to analyse the NOx-NH_3 trade-off graphically is presented. The methodology is exemplified by testing P, PI,

PD, and PID controller, both with and without ANR based feedforward. The chapter thus reports both a useful methodology, and a comprehensive study of simple feedback and feedforward controllers. The methodology is validated experimentally by conducting full-scale engine tests where the controllers are used for urea dosing.

Chapter 8 - System Wide Modelling of the Exhaust Gas Cleaning System: A methodology that can be used to develop a modular simulation tool for the exhaust gas cleaning system is presented. The methodology proposes a simulation tool structure that enables the program to simulate a broad variety of systems. Four different models for the different monoliths in the standard Euro VI exhaust system are presented and used to create a modular simulation tool, which is used to simulate the system under different conditions.

1.4 Publications

The scientific publications produced during the PhD are listed below. Distinction is made between journal papers, conference proceedings, and abstracts. Papers are classified as either published, submitted, or in preparation.

1.4.1 Journal Papers

1. A. Åberg, A. Widd, J. Abildskov, J. K. Huusom. Parameter Estimation and Analysis of an Automotive Heavy-duty SCR Catalyst Model. Chemical Engineering Science 161 (2017) 167-177.

2. A. Åberg, A. Widd, J. Abildskov, J. K. Huusom. Estimation of Kinetic Parameters in an Automotive SCR Catalyst Model. Topics in Catalysis 59 (2016) 945-951.

4. A. Åberg, A. Widd, J. Abildskov, J. K. Huusom. Pareto Front Analysis of Automotive SCR Control. Submitted to Control Engineering Practice, 2017.

3. T. Christiansen, J. Sydney, A. Åberg, J. Abildskov, J. K. Huusom. Methodology for Developing a Diesel Exhaust After Treatment Simulation Tool. Submitted to SAE Technical Papers, 2016.

1.4.2 Conference Proceedings

1. A. Åberg, T. K. Hansen, K. Linde, A. K. Nielsen, R. Damborg, A. Widd, J. Abildskov, A. D. Jensen, J. K. Huusom. A Framework for Modular Modeling

of the Diesel Engine Exhaust Gas Cleaning System. Computer Aided Chemical Engineering 37 (2015) 455-460.

2. A. Åberg, A. Widd, J. Abildskov, J. K. Huusom. Methodology for Analysing the NOx-NH_3 Trade-off for the Heavy-duty Automotive SCR Catalyst. Submitted to The 20th World Congress of the International Federation of Automatic Control, 2017, Toulouse, France.

1.4.3 Abstracts

1. A. Åberg, A. Widd, J. Abildskov, J. K. Huusom. Modeling the Automotive SCR Catalyst. Book of Abstracts of 19th Nordic Process Control Workshop. On the Coastal Steamer "Richard With" from Trondheim to Bodø.

2. A. Åberg, A. Widd, J. Abildskov, J. K. Huusom. Model Based Evaluation of Control Algorithms for the Automotive SCR Catalyst. Book of Abstracts of International Symposium on Modeling of Exhaust-Gas After-Treatment (MODEGAT IV) 13th - 15th September 2015, Bad Herrenalb/Karlsruhe, Germany.

3. A. Åberg, A. Widd, J. Abildskov, J. K. Huusom. Modeling and Control of the Heavy Duty Automotive SCR Catalyst. Book of Abstracts of 2015 AIChE Annual Meeting, November 8th - 13th, Salt Lake City, USA.

4. A. Åberg, A. Widd, J. Abildskov, J. K. Huusom. Pareto Front Based Design of Controllers for the Automotive SCR Catalyst. Book of Abstracts of 20th Nordic Process Control Workshop, 25th - 26th August 2016, Sigtuna Stiftelsen, Stockholm.

Chapter 2

Overview of the SCR Technology

This chapter will present an overview of the SCR technology. The historical and current uses of the technology, along with the SCR reactions will be shown. Previous modelling of the SCR catalyst, both monolith channel modelling, and kinetic modelling, will be presented, along with previous efforts to control the urea dosing. The main focus is on vanadium based SCR catalysts.

2.1 Selective Catalytic Reduction

Ammonia based SCR has been used for stationary exhaust gas applications since the 1970s in Japan. The first applications were related to gas, coal, and oil-powered powerplants, which were equipped with SCR catalysts in order to reduce NOx emissions. The SCR catalyst were based on vanadium/titania and achieved a NOx removal efficiency of 90-95% [8, 60]. Ammonia was used as a reducing agent. In the 1980s the technology was introduced in Europe, with similar success. In the 1990s the technology was investigated as potential NOx removal system for mobile sources, such as the heavy-duty truck sector, which faced increasingly tough legislative NOx emission limits [104]. The application of SCR catalysis in a mobile application introduces several challenges. The exhaust temperature of stationary sources tend to be higher compared to mobile sources, where the SCR catalyst has a higher activity [70]. The mobile applications also have a broader operational span, with highly transient inlet conditions. Another problem is that compared to the stationary applications that used ammonia directly as a reducing agent, the automotive industry required a different ammonia delivery system that would not pose dangers in an accident. The alternative that became standard was a urea-water solution called AdBlue [46], which consists of 32.5 mass-% urea. The concentration was chosen because of a freezing point minimum at this concentration. When the urea solution is injected into the warm exhast gas stream, the water in the AdBlue solution evaporates, and the urea decomposes according to (R 2.1) and (R 2.2) [64].

$$NH_2 - CO - NH_2 \rightarrow HNCO + NH_3 \quad \text{(R 2.1)}$$

$$HNCO + H_2O \rightarrow NH_3 + CO_2 \quad \text{(R 2.2)}$$

One of the first investigations of applying the technology to mobile applications was done by Koebel et al. [66], who studied the removal of NOx from a heavy-duty diesel engine. They identified that the main challenges were related to the urea dosing due to the transient nature of the diesel engine. Havenith and Verbeek [45] used different urea dosing strategies to show that the SCR catalyst could be used to meet Euro IV emission limits. A significant problem with the urea SCR technology was that the system depended on a separate tank of water and urea solution that was used a the reductant. This required that an infrastructure was available, so that road-going vehicles could refill the urea tank when needed [84]. Due to this, other technoligies were proposed as alternatives, such as the HC-SCR

[109] and lean NOx adsorbers. These technologies used the diesel fuel as reductant, and therefore eliminated the need for a new urea infrastructure. The urea SCR technology however had other advantanges, such as higher NOx conversion. This in combination with the fact that good knowledge about the urea-SCR technology had been achieved in the stationary applications, urea-SCR became the leading technology for the reduction of NOx for mobile applications.

2.1.1 Main Reactions

The SCR catalyst has three main reactions that are the basis for its NOx reducing capabilities. These are the standard SCR reaction (R 2.3), the fast SCR reaction (R 2.4), and the slow SCR reaction (R 2.5) [121]. These reactions are the same for the different catalysts that will be presented in Section 2.1.3, while the side-reactions presented in Section (2.1.2) can differ depending on the catalyst.

$$4NH_3 + 4NO + O_2 \rightarrow 4N_2 + 6H_2O \quad \text{(R 2.3)}$$

$$2NH_3 + NO + NO_2 \rightarrow 2N_2 + 3H_2O \quad \text{(R 2.4)}$$

$$8NH_3 + 6NO_2 \rightarrow 7N_2 + 12H_2O \quad \text{(R 2.5)}$$

The standard SCR reaction is typically the main reaction occurring in the catalyst [22]. The reaction consumes equimolar amounts of NH_3 and NO. The composition of the engine out diesel exhaust gases can vary depending on engine settings, however under normal operation the outlet NOx is typically 90% NO, and 10% NO_2 [59]. The catalysts that are placed before the SCR catalyst will also affect the ratio of NO/NO_2. The Diesel Oxidation Catalyst (DOC) will oxidise some of the NO to NO_2, while the Diesel Particulate Filter (DPF) will use NO_2 for regeneration [80]. The initial high NO content of the NOx gases however results in that the standard SCR reaction is the main reaction of the process. Dumesic et al. suggested a detailed kinetic mechanism in 1996 to describe the reaction steps occurring on a V_2O_5 based catalyst. Figure 2.1 shows a schematic view of the steps. Steps 1 and 2 describe the adsorption and activation of NH_3 on the acidic V^{5+}-OH sites. Step 3 describes the reduction of NO to N_2, where NO is gaseous or weakly adsorbed. Steps 4 through 6 describe the reoxidation of the catalyst. The activation energy for the standard SCR reaction depends on the catalyst, however it normally lies around 80-90 kJ/mol [135, 73].

In the presence of NO_2 the reaction speed is increased significantly due to the fast SCR reaction. The reaction gets its name from the fact that it has a faster reaction rate than the standard SCR reaction [27, 75]. Equimolar amounts of NO

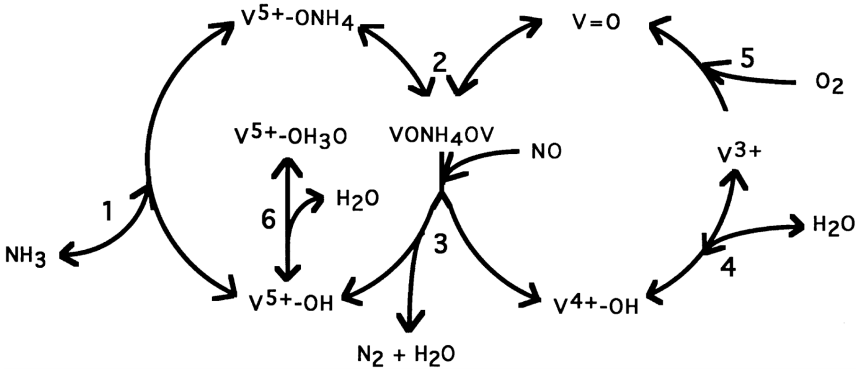

Figure 2.1. Schematic view of the reaction mechanism of the standard SCR reaction over a V_2O_5 catalyst. Figure from [35]

and NO_2 reacts with equimolar amounts of NH_3 to form N_2. Since it is faster than the other reactions, it is desirable to have the same levels of NO and NO_2 in the SCR catalyst to achieve the highest NOx conversion, especially at low temperatures.

If the NO_2/NO ratio goes above 1, the reaction known as the slow SCR becomes prominent [58]. The reaction is substantially slower than the other two SCR reactions [67, 25], and it is therefore undesirably to have a system that operates at NO_2/NO ratios above 1 in the SCR monolith.

2.1.2 Side Reactions

This section presents the possible side reactions. There is a large number of possible reactions that can occur in the SCR catalyst, but the focus here is on the most common.

2.1.2.1 Ammonia Oxidation

Ammonia oxidation reactions are generally problematic under normal SCR conditions, due to the lean atmosphere present in the exhast gases. To achieve good SCR performance, the reduction of NOx has to prevail over the reduction of O_2. Several different ammonia oxidation reactions are possible. Some of them are [76]:

$$4NH_3 + 3O_2 \rightarrow 2N_2 + 6H_2O \quad \text{(R 2.6)}$$

$$4NH_3 + 4O_2 \rightarrow 2N_2O + 6H_2O \quad \text{(R 2.7)}$$

$$4NH_3 + 5O_2 \rightarrow 4NO + 6H_2O \quad \text{(R 2.8)}$$

$$4NH_3 + 7O_2 \rightarrow 4NO_2 + 6H_2O \quad \text{(R 2.9)}$$

Some of the reactions are more likely than others under typical SCR conditions. Vanadium based catalysts has been reported to be highly selective towards N_2 at low temperatures, while at high temperatures favour NO [76]. Reaction (R 2.7) has been reported to be inhibited by the presence of H_2O, which is always present in diesel exhaust gases [120]. Duffy et al. [34] also reported that reaction (R 2.7) is not a significant N_2O contributor in vanadium based catalysts.

2.1.2.2 N_2O Formation

The formation of N_2O is currently not regulated by nitrogen oxides legislation. It is however regulated under greenhouse gas emissions, due to its greenhouse gas properties, and its influence on stratospheric ozone [101]. N_2O can be formed both from NO and, with intermediate steps, through NO_2 [76, 68]

$$4NH_3 + 4NO + 3O_2 \rightarrow 4N_2O + 6H_2O \quad \text{(R 2.10)}$$

$$2NH_3 + 2NO_2 \rightarrow N_2 + NH_4NO_3 + H_2O \quad \text{(R 2.11)}$$

$$NH_4NO_3 \rightarrow N_2O + 2H_2O \quad \text{(R 2.12)}$$

Reaction (R 2.10) is normally not considered in global kinetic models for N_2O formation, however Duffy et al. [34] reported that the reaction is occurring, atleast in situations when NO_2 is not present. Reaction (R 2.11) occurs at temperatures below 200^oC, when NH_3 is not able to reduce nitrates [68]. If NO_2 is in excess, Reaction (R 2.12) occurs at high temperatures, thereby producing N_2O. However, if NO and NH_3 is available, the ammonium nitrate can proceed to react according to the fast SCR reaction (R 2.4). Nitrates has been identified as a key intermediate for the fast SCR reaction, and has resulted into the reaction knows as The Enhanced SCR Reaction [38, 37].

$$2NH_3 + 2NO + NH_4NO_3 \rightarrow 3N_2 + 5H_2O \quad \text{(R 2.13)}$$

Reaction (R 2.13) requires that ammonium nitrate is supplied to the system, for example in an aqueous solution. The reaction results in a high NOx conversion at low temperature, which is similar to what the fast SCR reaction achieves.

2.1.3 Catalysts

As previously stated, the first industrial SCR applications were based on vanadium SCR catalysts, and because of the previous experiences with vanadium SCR, it was natural that these also were the first catalysts in mobile applications. The most common vanadium based SCR catalyst contains 1-3% V_2O_5 as the active component.

The catalyst is normally impregnated on a TiO_2 support material together with around 10% WO_3 to stabilise the vanadia and increase thermal stability [36, 65]. The active material can either be washcoated onto the monolith substrate or extruded, so that the monolith walls consists of the active material through the entire wall. Figure 2.2 shows an overview of the two design methods and their differences. The vanadium based catalyst has a maximum NOx conversion typically between 250-450^{o}C. Below 250^{o}C the light-off for the standard SCR reaction has not occurred, and above 450^{o}C the selectivity towards the SCR reactions is lowered due to NH_3 oxidation becoming prominent [83]. The light-off temperature for the standard SCR reaction can be modified by changing the composition of the catalyst. For example it has been reported that if the V_2O_5 content was increased from 0.78% to 1.4%, the light-off temperature was decrease from 267^{o}C to 207^{o}C [36]. The vanadium based SCR catalyst has a high resistance to sulfur poisoning, which is a problem in diesel fuels especially in some developing countries. The sulphur level has been reported to be as high as 2000 ppm in some regions. The catalyst has therefore been identified as especially important in these regions in order to reduce NOx emissions [43]. A disadvantage with the vanadium based SCR catalyst is that it suffers from low thermal stability, compared to zeolite based catalysts. If the exhaust gas treatment system is equipped with a DPF, it might be required to use active regeneration techniques to remove the deposited soot. This is done by injecting fuel into the exhaust system, which ignites and drastically increases the temperature of the gases [69]. A catalyst that suffers from low thermal stability can in these instances be destroyed.

In recent years significant research has been done related to zeolite-based catalyst. The zeolites are exchanged with metal ions, primarily Cu and Fe [77, 14]. Several different types of zeolites has been investigated in literature, with varying properties. Automotive applications has mainly been based on BEA and SAPO-34. The main SCR reactions presented in Section 2.1.1 are the same for zeolite catalysts, however due to the different chemical properties of the zeolite catalysts, the reaction mechanisms are different. The zeolite based catalysts are attractive because they do not rely on precious metals, and have good SCR activity over a broad range of temperatures. The major difference between Cu and Fe exchanged zeolites is the optimal temperature region. Fe zeolites generally operate at a higher temperature, while Cu zeolites are better at low temperatures [61]. This can be seen in Figure 2.3, where the NOx conversion for the vanadium based SCR, and the Fe and Cu exchanged zeolites are compared based on the reaction temperature. Compared to the vanadium based catalysts, they are more sensitive to sulfur posion-

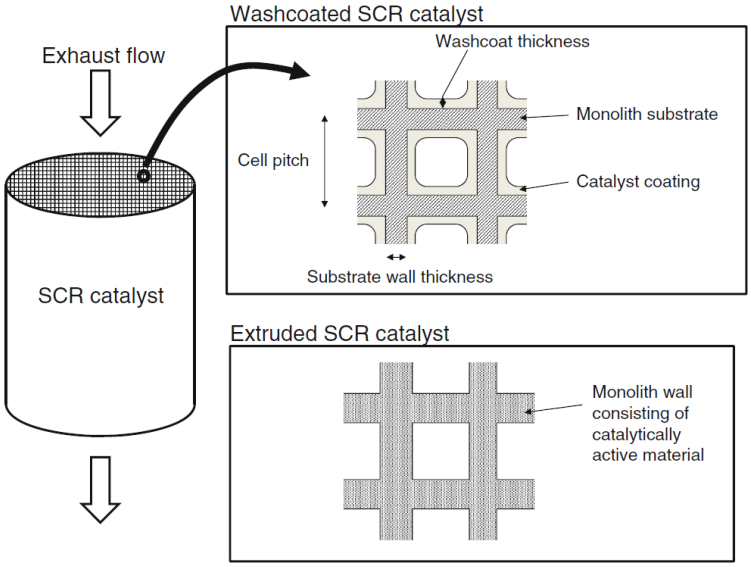

Figure 2.2. Comparison between the two major design methods for creating SCR monoliths. Figure from [59]

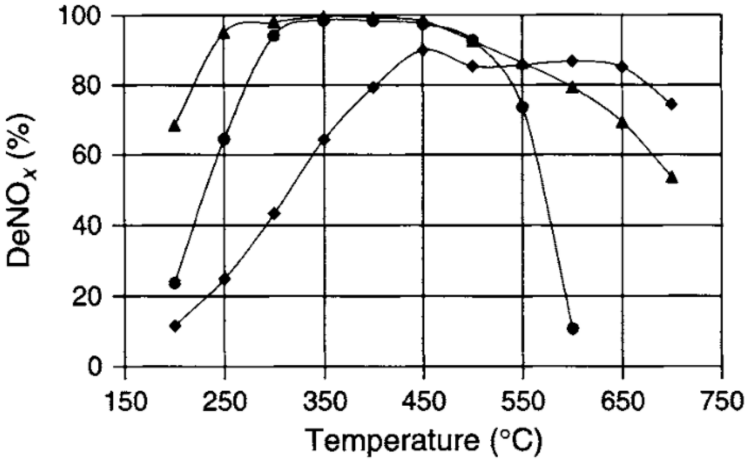

Figure 2.3. NOx conversion against reaction temperature for vanadium based catalyst (●), Fe zeolite (♦), and Cu zeolite (▲). Figure from [70]

ing, making them more appropriate for markets in developed countries [43]. They are also significantly more stable at DPF regenerations temperatures above 650^{o}C. It has been reported that small-pore copper exchaged zeolites can maintain high NOx reduction capabilities even after prolonged exposure to 800^{o}C [56]. Given the low light-off temperature the Cu exchanged zeolite is a good alternative for future emission standards. The current World Harmonized Transient Cycle (WHTC) has long sections where the gas temperature is low [132], requiring a catalyst that can achieve a high NOx reduction even at low temperatures. New innovative diesel engine designs are also moving towards lower exhaust temperatures, making this property increasingly important.

2.2 Modelling the SCR Catalyst

This section presents previous modelling results on the SCR catalyst and monolith, both related to the channel model, and the kinetic model. Calibration of kinetic parameters, along with validation of the models, will also be discussed.

2.2.1 Channel Modelling

Modelling of the SCR catalyst is a well studied area, with many examples in literature, both of models that are based on first-principles, and data-driven models. The main focus of this section will be on models based on first principles. The SCR monolith is in the majority of cases a flow through reactor, that consists of several parallel channels. The majority of models assume that one of these channels is representative for the entire monolith, so called single-channel-models. The channel models are in a majority of cases one dimensional, however there are reports of multi-dimensional modelling, also for the SCR monolith, which will be discussed briefly.

The first models related to the exhaust aftertreatment system were for the three-way-catalyst. Since many of the physical properties that were introduced in these models still are valid for SCR models, a overview of these will be given. One of the first cases of one-dimensional modelling for exhaust aftertreatment was proposed in the 1960s by Vardi and Biller [127], who examined the thermal behaviour of a catalytic converter. The authors argued that the thermal conduction and thermal accumulation were insignificant for the gas phase, and that the thermal conduction in the solid phase was insignificant, and arrived at the following equations to

describe the temperature dynamics of the monolith:

$$\frac{\partial T_s}{\partial t} = a_s h(T_g - T_s) \tag{2.1}$$

$$\frac{\partial T_g}{\partial z} + \frac{a_s h L}{G C_g}(T_g - T_s) = 0 \tag{2.2}$$

where T_s is the solid phase temperature, a_s is the specific area, h is the heat transfer coefficient, T_g is the gas phase temperature, and L is the length of the monolith. The authors simulated various driving conditions, and analysed the dynamics of the temperature, which was in satisfactory agreement with experimental data.

Kuo et al. continued the one-dimensional modelling with a tanks-in-series model that included reaction heat and the propagation of the chemicals through the channel [71]. The model also included heat losses to ambient. The model was developed through a trial and error approach, where simplifications were added and removed in relation to how well the model could predict the monolith outlet. The simulation was carried out on the Federal Test Procedure (FTP), which includes several transient sections, which the model was able to accurately predict. The model did however not include any film-transfer for the chemical species to the catalyst surface, but the species equations were instead a simple form of a mass balance:

$$\frac{G}{(60)(359.05)}(x_{i-1}^j - x_i^j) = \left(\frac{1-\varepsilon}{12^3}\right) V_i r_i^j \tag{2.3}$$

where G is the flow, x is the fraction of species i, ε is the porosity of the washcoat, and r is the reaction rate. The flow characteristics and film-transfer were later added by Harned in 1972 [44].

Out of the classical models for automotive catalytic converters, the model that is closest to what is often seen in current literature, is the model reported by Oh and Cavendish [88]. The model considered convective gas flow through the channel, with mass and heat film transfer to the solid phase. The model considered accumulation of energy in the gas and solid phase, as well as accumulation of mass in the gas phase. It also included a more complicated reactions scheme than had been

included in previous work. The model equations were:

$$\varepsilon \frac{\partial c_{g,i}}{\partial t} = -v \frac{\partial c_{g,i}}{\partial x} - k_{m,i} S (c_{g,i} - c_{s,i}) \tag{2.4}$$

$$\varepsilon \rho_g C_{pg} \frac{\partial T_g}{\partial t} = -v \rho_g C_{pg} \frac{\partial T_g}{\partial x} + hS(T_s - T_g) \tag{2.5}$$

$$a(x) R_i(c_s, T_s) = \frac{P_{tot}}{R_g T_g} k_{m,i} S (c_{g,i} - c_{s,i}) \tag{2.6}$$

$$(1-\varepsilon)\rho_s \frac{\partial (C_{ps} T_s)}{\partial t} = \lambda_s (1-\varepsilon) \frac{\partial^2 T_s}{\partial x^2} + hS(T_g - T_s) + a(x) \sum_{i=1}^{4} (\Delta H)_i R_i(c_s, T_s) \tag{2.7}$$

where c_g is the gas phase concentration, ε is the fraction of open area in the cross-section of the channel, v is the linear gas velocity, k_m is the mass transfer coefficient, S is the specific surface, c_s is the concentration in the solid phase, ρ is the density, C_p is the heat capacity, h is the heat transfer coefficient, R is the reaction rate, P_{tot} is the total pressure, T is the temperature, and λ is the thermal conductivity. As seen, the model also included axial heat conduction in the solid phase, which was shown to have an effect on the wall temperature profile. The model was not tested against experimental data, but was used to test the effects different catalyst design parameters and operating conditions had on the light off behaviour.

The presented models has acted as the basis for automotive catalyst modelling and has proven successful at describing their dynamic behaviour. When the SCR monolith is modelled, the differences compared to the presented models are more related to the reaction kinetics rather than the underlying physical model. Tronconi et al. presented a 1D SCR monolith model for a washcoated vanadium based catalyst [122]. The model physics are similar to what was described by [88]. NO and NH_3 were the species considered, and the equations were:

$$\frac{\partial C^b_{NH_3}}{\partial t} = -\frac{v}{L} \frac{\partial C^b_{NH_3}}{\partial z} - \frac{4}{d_h} k_{mat,NH_3} (C^b_{NH_3} - C^W_{NH_3}) \tag{2.8}$$

$$\frac{\partial C^b_{NO}}{\partial t} = -\frac{v}{L} \frac{\partial C^b_{NO}}{\partial z} - \frac{4}{d_h} k_{mat,NO} (C^b_{NO} - C^W_{NO}) \tag{2.9}$$

$$k_{mat,NH_3} (C^b_{NH_3} - C^W_{NH_3}) = sr^{eff}_{NH_3} \tag{2.10}$$

$$k_{mat,NO} (C^b_{NO} - C^W_{NO}) = sr^{eff}_{NO} \tag{2.11}$$

$$\rho^g c^g_p \frac{\partial T^g}{\partial t} = -\frac{\rho^g c^g_p v}{L} \frac{\partial T^g}{\partial z} - h \frac{4}{d_h} (T^g - T^s) \tag{2.12}$$

$$\rho^s c^s_p \frac{\partial T^s}{\partial t} = \frac{h}{s} (T^g - T^s) + (-\Delta H_r) r^{eff}_{NO} \tag{2.13}$$

$$\Omega (1 - x^*) \frac{\partial \theta}{\partial t} = r^{eff}_{NH_3} - r^{eff}_{NO} \tag{2.14}$$

where the symbols are as previously, and Ω is the total storage capacity of NH_3, and θ is the coverage of NH_3. The model included no accumulation of mass in the solid phase, except for in Equation (2.14), which is important to note. The equation describes the amount of available adsorbed NH_3, which is used in the SCR reactions. This will be described more in detail in Section 2.2.2. The model considered NO and NH_3, and thus only the standard SCR reaction. The authors had previously reported a 2D model [123], however they noted that they achieved the same accuracy with the 1D model, together with a significant decrease in simulation time. The authors fitted the model to a variety of transient NO reduction data that had been collected from commercial SCR monoliths.

Chatterjee et al. argued that the model presented by Tronconi was only suitable for washcoated SCR monoliths, and presented a 1D+1D model that included washcoat diffusion, to make it appropriate for extruded monoliths [17]. The model equations were the same as presented by Tronconi in Equations (2.8) through (2.14), however also included an equation to account for the washcoat diffusion:

$$0 = D_{eff,j}\frac{\partial^2 C_j}{\partial x^2} + S_W^2 R_j \tag{2.15}$$

The fact that the model considers spatial resolution both along the axis of the channel, and through the monolith wall makes it a 1D+1D model.

In relation to recent literature, the model structure has not changed compared to the models presented above, although different authors use different assumptions, thereby leading to models of slightly different structure. Examples of more recent publications can be found for example in [6, 5, 95, 15, 115, 21, 114].

In situations where the inlet conditions to the monolith are not uniform, it can be necessary to consider 2D or 3D models [62]. When the monolith is modelled in multiple dimensions, the equations describing the mass and heat balances are the same, however additional equations are added that represents the additional dimensions. Additional physical properties are also included in some works, for example by Chen and Tan [19].

2.2.2 Kinetic Modelling

This section will focus on the kinetic models that previously has been developed for the vanadium based SCR catalyst. The main focus is on global kinetic schemes, which in many cases are not different for vanadium and zeolite based catalysts. For example, the global reaction scheme for a Cu-zeolite by Ohlson et al. [89] has served as a global kinetic model for vanadium based catalysts as well [79],

and has showed good results in predicting the catalyst dynamics. Several kinetic studies and models has been published related to vanadium based SCR catalyst. Examples are [18, 15, 124, 72, 135, 73]. In the following subsections the focus will be on comparing two different kinetic models, reported by Ohlson et al. [89] and Chatterjee et al. [18].

2.2.2.1 Ammonia Adsorption and Desorption

The most important reactions for describing the SCR catalyst dynamics are the reactions related to NH_3 adsorption and desorption, which could also be seen in the standard SCR reaction mechanism in Figure 2.1. The use of this Eley-Rideal mechanism has seen broad use in literature, since it was suggested by Miyamoto et al in the 1970s [82]. The mechanism assumes that NH_3 is adsorbed to the catalyst surface, and the adsorbed NH_3 reacts with the other reactants. The rates of all other SCR reactions are therefore dependent on the amount of NH_3 that is adsorbed on the surface [78]. The adsorption and desorption of NH_3 can be written as:

$$S + \mathrm{NH_3} \leftrightarrow \mathrm{S - NH_3} \tag{R 2.14}$$

where S represents an empty catalyst side and $\mathrm{S - NH_3}$ represents an adsorbed NH_3 molecule. In most cases, the catalyst is assumed to have one global adsorption site representing all possible sites of different nature. The activation energy for the adsorption reaction is often assumed to be 0, and the reaction for the adsorption reaction can be written:

$$r_{ads} = k_{ads} c_{NH_3} (1 - \theta) \tag{2.16}$$

where θ represents the fraction of sites that are currently inhabited by an NH_3 molecule. For the desorption reaction, a Tempkin dependency is used for the activation energy [7]:

$$r_{des} = k_{0,des} \exp\left(\frac{-E_{des,0}(1 - \alpha\theta)}{RT}\right)\theta \tag{2.17}$$

Multi-site approaches are also possible, where the NH_3 molecules can adsorb to different sites on the catalyst surface. This is however more common for the zeolite based catalysts, as they have different acidic sites where adsorption can occur [102].

2.2.2.2 SCR Reactions

Several different models for describing the global SCR reactions are suggested in literature. For example, Ohlson et al. reported standard Arrhenius based kinetics

with first order reactions, which can be seen in Equations (2.18) through (2.20) [89].

$$r_{standard} = k_{standard} * \exp\left(\frac{-E_{standard}}{RT}\right) c_{NO}\theta \tag{2.18}$$

$$r_{fast} = k_{fast} * \exp\left(\frac{-E_{fast}}{RT}\right) c_{NO}c_{NO_2}\theta \tag{2.19}$$

$$r_{slow} = k_{slow} * \exp\left(\frac{-E_{slow}}{RT}\right) c_{NO_2}\theta \tag{2.20}$$

Even though the reaction kinetics are modelled in a simplistic manner, the model proved successful at predicting the dynamics of a Cu exchanged zeolite.

A more detailed kinetic model was presented by Chatterjee et al., where it was assumed that NH_3 could block the sites for NO activation, and that the reoxidation of such a site was the rate limiting step [18]. The adsorption of NH_3 was also in competition with the adsorption of ammonium nitrate. The rate of the standard SCR reaction was therefore limited by the NH_3 coverage and increased by a higher O_2 concentration. The fast SCR reaction revolved around the intermediate formation of NH_4NO_3 and HNO_3 from NO_2. The reaction equations were:

$$r_{standard} = k^0_{standard} \exp\left(\frac{-E_{standard}}{RT}\right) \gamma_{NO} C_{NO} \theta_{NH3} \left(\frac{P_{O_2}}{0.02}\right)^{\beta} \tag{2.21}$$

$$\gamma_{NO} = \frac{1}{1 + K_{LH} \frac{\theta_{NH_3}}{1-\theta_{NH_3}-\theta_{NH_4NO_3}}} \tag{2.22}$$

$$r_{fast} = k^0_{fast} \exp\left(\frac{-E_{fast}}{RT}\right) \gamma_{fast} \left(C_{NO} c_{HNO_3} - \frac{C_{NO_2} C_{HNO_2}}{K_{eq,fast}}\right) \tag{2.23}$$

$$\gamma_{fast} = \frac{1}{1 + K_{LH2} \frac{\theta_{NH_3}}{1-\theta_{NH_3}-\theta_{NH_4NO_3}}} \tag{2.24}$$

The equation for the slow SCR reaction was the same as Equation (2.20).

2.2.2.3 Side Reactions

In the work of Ohlson et al., only ammonia oxidation to N_2 was included [89]. A simple Arrhenius based expression that incorporated the adsorbed NH_3 and O_2 concentration was adopted:

$$r_{ox} = k_{ox} \exp\left(\frac{-E_{ox}}{RT}\right) C_{O_2}\theta \tag{2.25}$$

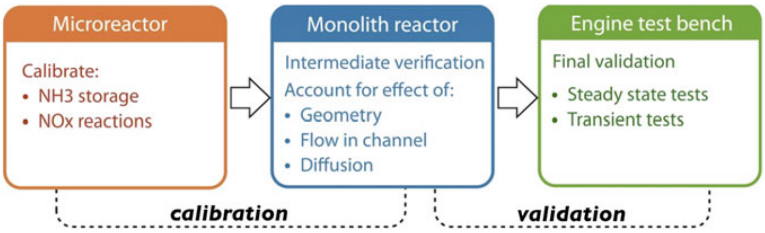

Figure 2.4. Overview of a typical calibration and validation methodology for a global reaction scheme. Figure from [62]

The work by Chatterjee et al. also only included ammonia oxidation to N_2, however with a different dependence on oxygen than previously.

$$r_{ox} = k_{ox}^{0} = \exp\left(\frac{-E_{ox}}{RT}\right)\left(\frac{P_{O_2}}{0.02}\right)^{\beta}\theta_{NH_3} \tag{2.26}$$

For the formation of N_2O, there are no differences between the works, and a Arrhenius based first order reaction was chosen:

$$r_{N_2O} = k_{N_2O}\exp\left(\frac{-E_{N_2O}}{RT}\right)C_{N_2O}\theta_{NH_3} \tag{2.27}$$

2.2.3 Calibration and Validation

The parameter estimation of the kinetic parameters is an essential step in a model that should be used for the application. Applying kinetic parameters that has been calibrated using experimental data from another system, can result in mass transfer conditions being different, and therefore the same fit with data cannot be achieved. Depending on the complexity of the kinetic model, more or less advanced experimental tests may be required. Another critical element of the calibration process is to validate the model in the conditions were it is intended to be used. According to D. Karamitros and G. Koltsakis [62], a typical methodology to calibrate and validate a global kinetic model is to use microreactor experiments to calibrate the NH_3 storage reactions and the SCR reactions. A small-scale monolith reactor should be used as an intermediate calibration and validation step, and finally a full-scale engine test bench should be used for final validation, where for example transient tests can be evaluated. An overview of the methodology can be seen in Figure 2.4.

The reason that microreactor experiments are conducted is because these can remove any mass transfer limitations that are present. The kinetic parameters are therefore intrinsic, and are easier to use for different models. Microreactor experiments for calibration of the kinetic parameters has for example been done in

[18, 137, 17]. There are however situations were microreactor experiments are not possible, and there are several reported cases in literature where the kinetic model has been calibrated using experiments on a small-scale monolith [89, 78, 115].

To obtain an optimal fit for the parameters related to each reaction, a sequential parameter estimation method is often used. One way to organise the sequence is as done by Sharifian et al. [113]. The first step is to estimate the parameters related to the ammonia adsorption and desorption reactions. This is done without NO in the feed gas stream, to avoid influence from the SCR reactions. A common method is to also use a Temperature Programmed Desorption (TPD) experiment. NH_3 is sent to the reactor at a constant temperature until steady-state is achieved. The temperature is then gradually increased, allowing the NH_3 to desorb from the catalyst surface. This provides a better estimation of the desorption parameter. However, for example Tronconi et al. [124] reported an estimation procedure where they did not use a TPD to estimate the desorption kinetics. If NO oxidation to NO_2 is included in the kinetic model, this should be estimated in a second calibration step, where only NO is sent to the reactor. In the last step, the remaining parameters are calibrated using the available $NO/NO_2/NH_3$ data. As an example of how the experiments can be designed to be able to achieve the most amount of information, the experimental design of Song et al. is recommended [115]. Figure 2.5 shows an overview of the experiments. The experiment design, along with a TPD test, allowed the authors to fit a large number of reactions to the experimental data.

After the kinetic parameters has been estimated the last step is the validation of the model. This should be done under the conditions where the model will be used, and in this application this is often a full-scale monolith treating real engine gases, from a full-scale engine. The engine can be following for example a transient cycle such as the European Transient Cycle (ETC), which was done by Tronconi et al [124]. The validation was carried out for the first 500 s of the ETC, where the model showed good correspondence with experimental data. The models predictive capabilities regarding NH_3 were however not validated.

2.3 Controlling the Urea Dosing

Compared to the stationary applications, a major obstacle for the automotive applications is the highly transient nature of the diesel engine [52]. This leads to large uncertainties in the inlet conditions to the monolith. Other problems are the non-linear dynamics of the SCR process, the difficulty of measuring some key states in the catalyst, such as the amount of adsorbed ammonia, and the cross-sensitivity to

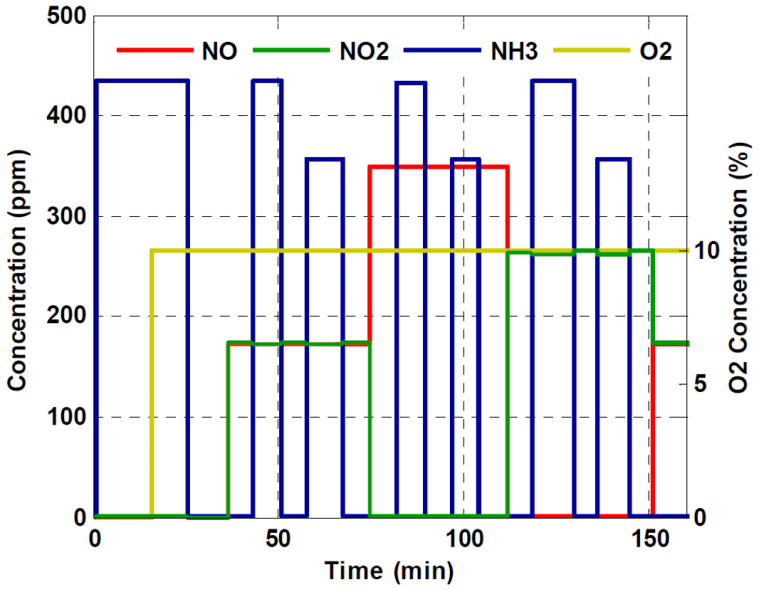

Figure 2.5. Overview of a possible experiment design to isolate information for different reactions. Figure from [115]

NH_3 for NOx sensors. Legislation before Euro VI did not include limitations on the NH_3 slip, meaning that the control problem as such was not necessarily difficult to meet. Common practice was however to introduce mean NH_3 slip limits around 25 ppm, as engineering targets, even though it was not a formal part of the legislation. [132].

Feedforward based methods has been reported to give high NOx conversion together with an acceptable NH_3 slip. Open-loop systems has been reported to primarily be built on look-up tables that were based on different factors in the system. The system measured the current engine situation, and dosed an appropriate amount of urea based on the look-up table. The open-loop control system used in a normal BOSCH aftertreatment system was reported by Seher et al. [110]. It has however been noted that these methods does not perform well when the urea dosing is inaccurate, or the catalyst is suffering from aging processes [134]. Willems et al. reported that feedforward based methods were not enough to meet future emission standards, and that closed-loop control strategies were required [134].

Feedback control based on NOx sensors has been proposed for example in [21, 105, 31], however it was also reported that with NOx sensors alone, it would be difficult to meet future legislative emission limits, due to cross-sensitivity issues [31].

To cope with this, NH_3 sensor based control has been suggested by for example Devarakona et al. [30]. The authors concluded that the analysis based on NH_3 sensor feedback performed very similar to using a NOx sensor based strategy. It was however still concluded that the method showed promise as a potential alternative to using a NOx sensor. Other work related to NH_3 sensor based feedback has been reported for example by Herman et al. [48], where the authors showed a control design that was robust against system disturbances.

A promising methodology is to base the control action on the amount of stored NH_3 on the catalyst surface. If the fraction of coverage is kept below a certain level, temperatures spikes in the inlet will not necessarily lead to significant desorption of NH_3, and the slip can therefore be kept low. Hsieh and Wang presented a controller based on ammonia surface control for a two-cell SCR system [51]. The first SCR cell was designed to have a high coverage ratio, while the second cell was designed to have a low coverage ratio. This ensured that the second cell had a high adsorption capability through-out the tests. The control design showed that the system was able to maintain a high SCR conversion while having a low NH_3 slip. Stadlbauer et al. presented a Adaptive Nonlinear Model Predictive Control (Adaptive NMPC) system that controlled the NH_3 coverage. The model also included adaptive elements to account for aging processes such as urea aging [117].

MPC has in general been identified as a promising technology for the application, however the model is a critical part of these control systems [117]. The first application of MPC to the automotive SCR system was presented by McKinley in 2010 [79]. The MPC was based on a first principles model which was reduced to a first order linear model. Zanardo et al. presented a grey-box model coupled with a linear data-based output error model intended for control applications [140]. The output error model was used to overcome the assumptions that the grey-box model were based on, such as only including the fast SCR reaction, out of the SCR reactions. Considering the very low computational effort to solve the model, the predictive results were impressive. The model was applied by Stadlbauer et al. in an NMPC designed to control the ammonia coverage [116]. Stadlbauer et al. also presented a NMPC based on a black box SCR model [118] intended for small combustion engines. The authors argued that the features of the smaller SCR monoliths used for small engines resulted in faster dynamics, and phenomena such as NH_3 storage were less pronounced. Therefore a purely data based model was satisfactory for such an application.

For the current Euro VI legislation in Europe, a new transient test cycle was in-

troduced that includes a cold start procedure. Future control therefore has to be able to cope with urea dosing at lower temperatures, which is made difficult by the fact that urea decomposition is slow and incomplete below 200^oC [138]. Since the main low temperature issue is caused by physical limitations of the system, the solution is related to improving the system configuration rather than improved dosing control. Innovative new system design are proposed in literature, such as combining units and placing the SCR catalyst closer to the engine outlet gases [125]. There are however challenges related to the urea dosing control at low-temperature as well. At low temperatures, the NOx conversion efficiency is low and the NH_3 storage capacity is high, and the model of the system becomes and integrator with reduced damping, where small errors can increase over time [138]. The accuracy of the NH_3 adsorption and desorption model is therefore more critical at low temperatures. The previously described NH_3 storage control systems are promising for coping with these new challenges [138].

Chapter 3

Modelling the SCR Monolith

This chapter presents five models used in the thesis. The model including the most physical phenomena is derived in full, and based on this, the remaining simplified models are presented. The simplified models includes simplifications related to mass and heat transfer. The kinetic models that is coupled with the channel models is also presented. The methodology that has been used to implement the models is shown using an example. The main contribution of this chapter is published in two articles (A. Åberg, A. Widd, J. Abildskov, J. K. Huusom. Parameter Estimation and Analysis of an Automotive Heavy-duty SCR Catalyst Model. Chemical Engineering Science 161 (2017) 167-177), and (T. Christiansen, J. Sydney, A. Åberg, J. Abildskov, J. K. Huusom. Methodology for Developing a Diesel Exhaust After Treatment Simulation Tool, Submitted to SAE Technical Papers, 2016). Early work related to this chapter was presented at the Nordic Process Control Workshop, 2015.

3.1 Introduction

The purpose of this chapter is to present and derive the developed models that have been used throughout the thesis. A description of the modelled monolith will be given, and after that, the models will be presented in the following sections.

Five different models will be presented that are based on different assumptions on the physical nature of the monolith. All of the models are based on modelling one single channel of the monolith. The monolith contains many parallel channels, and a common assumption during modelling is that one channel is representative of all. The most complex model will be derived in full, in order to explain most of the underlying phenomena occurring inside the monolith. The rest of the models are based on simplifications related to mass and heat transfer, which are the two most important phenomena occurring in the monolith, besides the reactions. The model that will be used primarily in this thesis is model 2, which offers a good trade-off between complexity and simulation accuracy. The kinetic model that is coupled with the channel models is also be presented. This will not be changed throughout the thesis.

The modelled monolith is a vanadium based catalyst and is made up from several small channels. Two different phases exist inside the channel, the bulk phase and the wash coat phase. The channel walls are made from wash coat, which is where the active catalytic material is located. Due to porous walls, diffusion between the channels can occur. The shape of the channels are sinusoidal and the channel density is 270 Cells Per Square Inch (CPSI). The catalyst is a full-body catalyst on a corrugated substrate. A picture of a typical SCR monolith can be seen in Figure 3.1.

As was seen in Chapter 2, modelling of the SCR catalyst is a well studied area. The motivation for dedicating a chapter to modelling in this work is that an accurate model was needed for the specific monolith used here. The lack of contributions in literature that investigates which phenomenons that are important to include in a model in order to describe the monolith dynamics motivates why several models are developed. A structured analysis on how different simplifications affects the prediction of the model is of interest for example in control applications, where the model structure has to be as simple as possible for computational reasons, while at the same time be able to describe the dynamics accurately.

Figure 3.1. A typical full-scale SCR monolith. Courtesy of Haldor Topsoe A/S.

3.2 Model 1 - Wash Coat Diffusion Model

This section will present the derivation of the model including the most physical phenomena. All steps of the model derivation will be shown in full. The models that are presented later will be based on simplifications of this model, and will therefore not be derived in full.

A single monolith channel can be represented schematically as in the top of Figure 3.2, together with the quantities used in the model. The physical quantities at the channel entrance are a volumetric flow Q, a concentration of species i, $c_{in,i}$, a temperature T_{in}, a molar dispersive flow $N_{in,i}$, and a dispersive energy flow W_{in}. The corresponding quantities leaving the channel are Q, $c_{out,i}$, T_{out}, N_{out}, and W_{out}. The molecules migrate through a stagnant film from the gas phase to the wash coat phase, where they diffuse and react in contact with the active sites. To reduce the complexity of the model the following assumptions were made:

M1.A1 Square channels

M1.A2 Fully hydrolysed urea at the SCR inlet

M1.A3 Identical monolith channels and uniform inlet conditions

M1.A4 No pressure drop in the channel

M1.A5 No diffusion in channel bulk phase

M1.A6 No volumetric gas changes inside the channel

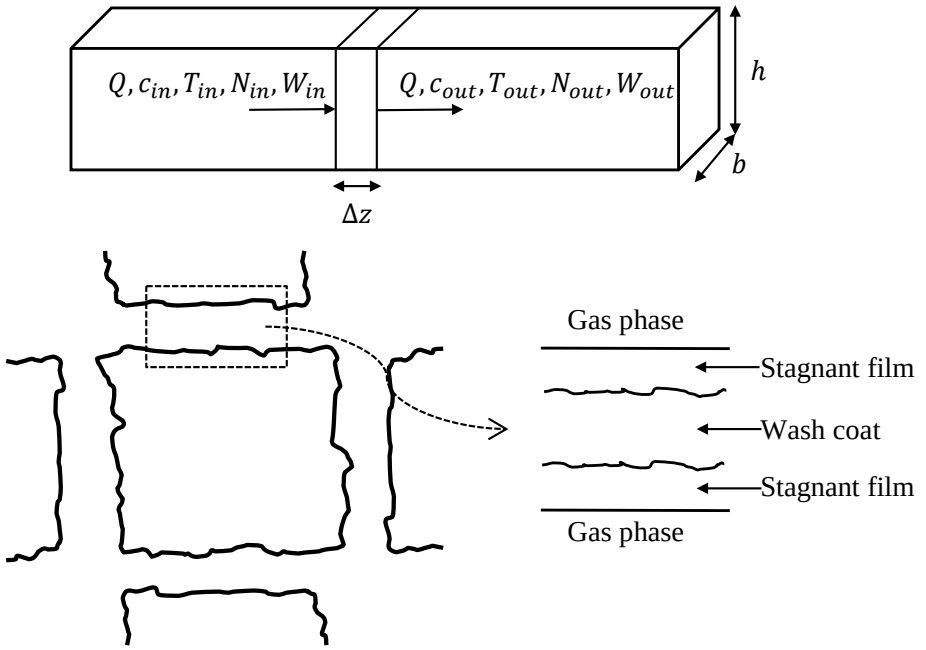

Figure 3.2. Top: Representation of a single monolith channel with physical quantities. Bottom: Representation of the channel bulk phase, stagnant film, and washcoat.

M1.A7 No convective flow in the wash coat

As described previously, the modelled catalyst is made up of sinusoidal shaped channels. M1.A1 is made to avoid modelling the complicated geometry. It will mostly affect the mass and heat transfer in the monolith. The assmumption will however only be made regarding the modelled geometry. With regards to the calculation of the heat and mass transfer coefficients, that will be shown in Section 3.8, the infinite Sherwood and Nusselt numbers will still be taken for sinusoidal channels. This will ensure that the mass transfer coefficients have correct values, even if the channels are modelled as squares.

M1.A2 influences the amount of available NH_3 in the catalyst. The assumption is valid for calibration data, explained in Chapter 4, since NH_3 was injected directly into the system. In full-scale engine conditions, that were used for model validation, the hydrolisation may affect the amount of available NH_3 [33]. The validity of the assumption also depends on the temperature that the system is operating at. The conversion of urea to NH_3 contains three steps that are all occurring more rapidly with an increased temperature. Evaporation of the urea solution, and the

two reaction steps that decomposes the urea into NH_3. Because of this, it is normal to only dose urea at temperatures above 180 ^{o}C. Another factor that affects the validity is how far before the catalyst the urea is injected. A greater distance gives a more complete hydrolisation, and better mixing. The assumption was included because it was desired to have as few reactions as possible, to minimize calibration effort. Any urea that is not hydrolysed in the inlet of the catalyst, will quickly be converted to NH_3.

M1.A3 can be expanded into underlying assumptions; there is no temperature difference between the channels, which means that no heat loss to the ambient is present. This is a better approximation in an insulated monolith. It also implies perfect NH_3 mixing before the SCR inlet, thus a uniform inlet concentration. This highly depends on the geometry and mixing devices of the dosing pipe. It is believed that this assumption will not introduce any significant error.

The effect of M1.A4 is that the volumetric flow rate will not change throughout the monolith channel, because of pressure changes. If the effect was included, the pressure would decrease as the gas passes through the channel, leading to an increase in the volumetric flow rate, and therefore velocity. The pressure drop is a linear function of the velocity and the length of the channel [136], and can be in the order of 10000 Pa [42] for a combined silencer and SCR catalyst.

M1.A5 concerns dispersion of the gases. While this is present, it is expected to be of little influence on the system. The system operates at gas velocities ranging from 3 m/s up to 20 m/s during normal operation. Considering that a normal SCR monolith is around 20-30 cm long, the residence time for the gas is very low, and therefore diffusion in the bulk phase has little time to affect the dynamics of the monolith.

M1.A6, as M1.A4, affects the velocity of the ingoing gases. The main effect of the velocity is the mass transfer coefficients. The effect will however be minor, and is not expected to influence results significantly.

M1.A7 is a realistic assumption since the modelled catalyst is of flow-through type. No gas is being forced into the wash coat, and therefore no convective flow is present.

Based on the described monolith, the physical phenomena, and the assumptions M1.A1 through M1.A7, the model was derived. The starting point for the derivation was the conservation of mass and energy. From this follows

$$\text{In} + \text{Production} = \text{Out} + \text{Accumulation} \tag{3.1}$$

Equation (3.1) states that what comes into the system and what is produced, is equal to what goes out of the system and that which is accumulated. This will be applied for the two sub systems bulk and wash coat.

3.2.1 Bulk phase

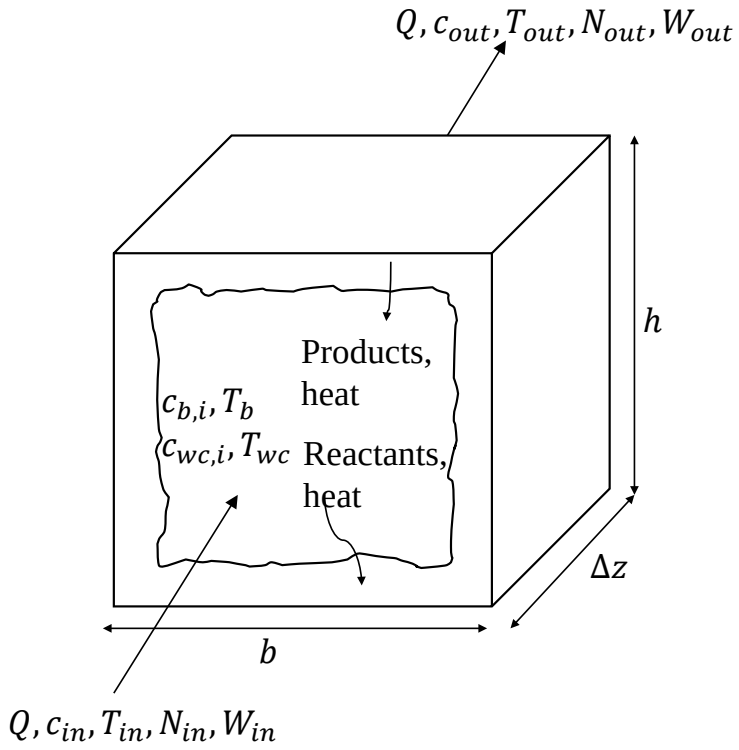

Figure 3.3. Representation of the control volume for the bulk phase, including model variables, that was used to derive the model.

Figure 3.3 shows a picture of the control volume and the different phenomena occurring. Gas with a concentration $c_{b,i}$ of species i, and a temperature of T_b, enters the control volume through convection. Energy and mass transport through a stagnant film into the wash coat. When the reactants have reacted in the wash coat, the products transport back into the bulk phase. The direction of the mass and heat transport depends on the gradient. The different terms in Equation 3.1 will be as follows.

In: $Qc_{in,i}\Delta t$

This term describes the amount of species i that enters the control volume through convective flow during time Δt, where Q is the volumetric flow rate.

Production:
The reactions take place at the active sites in the wash coat. Therefore no production is included in the bulk phase equations.
Out: $Qc_{out,i}\Delta t + 4b\Delta z k_g(c_{b,i} - c_{wc,s,i})\Delta t$
The first term is the amount of species i that is transported out through the control volume through convective flow during time Δt, and the second term is the film transport of species i from the bulk phase to the wash coat phase through the stagnant film. k_g is the mass transfer coefficient, $c_{wc,s,i}$ is the wash coat concentration at the surface, b is the side-length of the channel, and Δz is the length of the control volume.
Accumulation: $\Delta z b^2 \left(c_{b,i}\big|_{t+\Delta t} - c_{b,i}\big|_t \right)$
This term describes the change in moles of species i during time Δt inside the control volume. The above terms are inserted into Equation (3.1):

$$Qc_{in,i}\Delta t = Qc_{out,i}\Delta t + 4b\Delta z k_g(c_{b,i} - c_{wc,s,i})\Delta t + \Delta z b^2 \left(c_{b,i}\big|_{t+\Delta t} - c_{b,i}\big|_t \right) \tag{3.2}$$

This can be rearranged to

$$\frac{(c_{b,i}\big|_{t+\Delta t} - c_{b,i}\big|_t)}{\Delta t} = \frac{1}{b^2}\frac{Q(c_{in,i} - c_{out,i})}{\Delta z} - \frac{4k_g}{b}(c_{b,i} - c_{wc,s,i}) \tag{3.3}$$

Letting $\Delta z \to 0$, $\Delta t \to 0$, and applying assumption M1.A6 gives the final equation for the bulk phase concentration

$$\frac{\partial c_{b,i}}{\partial t} = -u\frac{\partial c_{b,i}}{\partial z} - \frac{4k_g}{b}(c_{b,i} - c_{wc,s,i}) \tag{3.4}$$

where u is the linear channel gas velocity, and the rest is as previously stated. Equation (3.4) is a first order Partial Differential Equation (PDE) and requires a Boundary Condition (BC) and Initial Conditions (IC) to be solved. These can be written as:

$$c_{b,i}(t,0) = c_{in,i}(t) \tag{3.5}$$

$$c_{b,i}(0,z) = c^0_{b,i}(z) \tag{3.6}$$

Equation (3.5) is the boundary condition, and states that the inlet concentration to the monolith has a certain value. The boundary condition is time dependent in for example a transient simulation, where the inlet conditions vary over time. Equation (3.6) is the initial condition, which states that at the start of a simulation, the monolith has a certain concentration of species i.

For the energy equation the same methodology is used.

In: $Q\rho_b C_{p,b} T_{b,in} \Delta t$

This term describes the thermal energy that enters the control volume through convective flow during time Δt. ρ_b is the bulk gas density, and $C_{p,b}$ is the bulk gas heat capacity.

Production:

As in the mass balance, no reactions take place in the bulk phase.

Out: $Q\rho_b C_{p,b} T_{b,out} \Delta t + 4b\Delta z h_{heat} (T_b - T_{wc,s})$

The first term is the energy leaving the control volume through convective transport, and the second term is the exchange of energy with the wash coat through film transfer. h_{heat} is the heat transfer coefficient, and $T_{wc,s}$ is the wash coat temperature at the surface.

Accumulation: $\Delta z b^2 \rho_b C_{p,b} \left(T_b|_{t+\Delta t} - T_b|_t \right)$

This term describes the change in energy during time Δt inside the control volume.

The above terms are inserted into Equation (3.1):

$$Q\rho_b C_{p,b} T_{b,in} \Delta t = Q\rho_b C_{p,b} T_{b,out} \Delta t + 4b\Delta z h_{heat} (T_b - T_{wc,s} + \Delta z b^2 \rho_b C_{p,b} \left(T_b|_{t+\Delta t} - T_b|_t \right) \tag{3.7}$$

This can be rearranged to

$$\frac{(T_b|_{t+\Delta t} - T_b|_t)}{\Delta t} = \frac{1}{b^2} \frac{Q\left(T_{b,in} - T_{b,out}\right)}{\Delta z} - \frac{4h_{heat}}{b\rho_b C_{p,b}} (T_b - T_{wc,s}) \tag{3.8}$$

Letting $\Delta z \to 0$, $\Delta t \to 0$, and applying assumption M1.A6 gives the final equation for the bulk phase temperature

$$\frac{\partial T_b}{\partial t} = -u \frac{\partial T_b}{\partial z} - - \frac{4h_{heat}}{b\rho_b C_{p,b}} (T_b - T_{wc,s}) \tag{3.9}$$

Equation (3.9) is also a first order PDE and requires BC and IC to be solved. These can be written as:

$$T_b(t,0) = T_{in}(t) \tag{3.10}$$

$$T_b(0,z) = T_b^0(z) \tag{3.11}$$

Equation (3.10) is the boundary condition, and states that the inlet gases to the monolith has a certain temperature. The boundary condition is time dependent in for example a transient simulation, where the inlet conditions vary over time. Equation (3.11) is the initial condition, which states that at the start of a simulation, the monolith has a certain temperature.

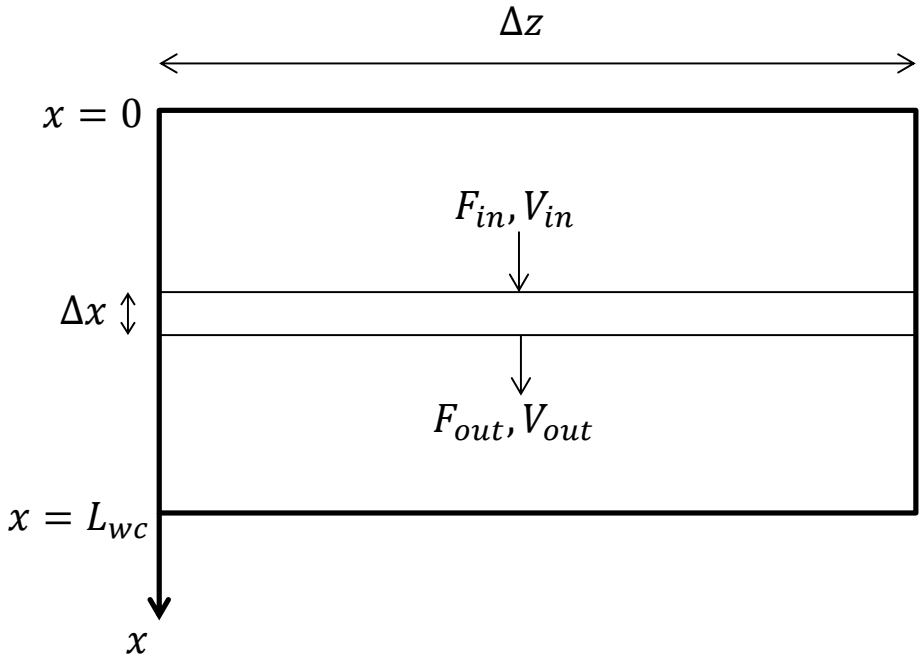

Figure 3.4. Representation of the control volume for the wash coat phase, including model variables, that was used to derive the model.

3.2.2 Wash coat phase

Figure 3.4 shows a picture of the control volume for the wash coat and the different phenomena occuring. The control volume has a thickness of Δx and a width of Δz. The wash coat is made up of pores, which the species diffuse in. A diffusive mass flux $F_{in,i}$, and energy flux W_{in} enters the control volume, and a corresponding mass and energy flux, F_{out} and W_{out}, leaves the control volume. The general conservation principle in Equation (3.1) is used as in Section 3.2.1.

In: $AF_{in,i}\Delta t$

The term describes the diffusive flow into the control volume of species i during time Δt. A is the cross-sectional area of the wash coat.

Production: $A\Delta x\Delta t\sum_i r_i$

Reactions take place on the active sites in the wash coat, and the net production of species i is described by the term above, where r_i is the rate of reaction.

Out: $AF_{out}\Delta t$

The term describes the diffusive flow of species i out from the control volume during time Δt.

Accumulation: $(1-\varepsilon_{wc})A\Delta x\left(c_{wc,i}|_{t+\Delta t} - c_{wc,i}|_t\right)$

This term describes the accumulated energy inside the control volume. $c_{wc,i}|_{t+\Delta t}$ is the wash coat concentration of species i at time $t+\Delta t$, and ε_{wc} is the porosity of the wash coat.
The above terms are inserted into Equation (3.1)

$$AF_{in,i}\Delta t + A\Delta x\Delta t\sum_i r_i = AF_{out,i}\Delta t + (1-\varepsilon_{wc})A\Delta x(\,c_{wc,i}|_{t+\Delta t} - c_{wc,i}|_t) \tag{3.12}$$

This can be arranged

$$\frac{(\,c_{wc,i}|_{t+\Delta t} - c_{wc,i}|_t)}{\Delta t} = \frac{1}{(1-\varepsilon_{wc})}\frac{(F_{in,i}-F_{out,i})}{\Delta x} + \frac{1}{(1-\varepsilon_{wc})}\sum_i r_i \tag{3.13}$$

Letting $\Delta z \to 0$, $\Delta t \to 0$ gives

$$\frac{\partial c_{wc,i}}{\partial t} = -\frac{1}{(1-\varepsilon_{wc})}\frac{\partial F_i}{\partial x} + \frac{1}{(1-\varepsilon_{wc})}\sum_i r_i \tag{3.14}$$

The term $\frac{\partial F_i}{\partial x}$ can be rewritten using Ficks first law, as in Equation (3.15).

$$F = D\frac{\mathrm{d}c}{\mathrm{d}x} \tag{3.15}$$

where D is the diffusion coefficient, and c is the concentration. Applying Ficks first law to Equation (3.14) gives the final mass balance equation for the wash coat

$$\frac{\partial c_{wc,i}}{\partial t} = \frac{1}{(1-\varepsilon_{wc})}D_{wc}\frac{\partial^2 c_{wc,i}}{\partial x^2} + \frac{1}{(1-\varepsilon_{wc})}\sum_i r_i \tag{3.16}$$

Equation (3.16) is a second order PDE and requires two BCs, and IC to be solved. These can be formulated as

$$\left.\frac{\partial c_{wc,i}}{\partial x}\right|_{x=0} = -\frac{k_g}{D_{wc,i}}(c_{b,i} - c_{wc,s,i}) \tag{3.17}$$

$$\left.\frac{\partial c_{wc,i}}{\partial x}\right|_{x=L_{wc}} = 0 \tag{3.18}$$

$$c_{wc,i}(0,x) = c^0_{wc,i}(x) \tag{3.19}$$

where $D_{wc,i}$ is the wash coat diffusion coefficient for species i. Equations (3.17) and (3.18) are the boundary conditions. The first one ensures that conservation of mass is kept at the bulk-wash coat interface, and the second states that a zero gradient is present at the bottom of the wash coat. The modelled catalyst is an extruded vanadium based catalyst, in which there is no clear distinction between the monolith wall and wash coat. It is in principle possible for species to diffuse from one channel to another. Under assumption M1.A3, this means that there is a

zero gradient at the end of the wash coat. Equation (3.19) are the ICs. These state that the wash coat concentration initially takes a certain value.

For the energy equation the same methodology is used.

In: $AV_{in}\Delta t$

The flow entering the wash coat control volume is the diffusive energy during time Δt.

Production: $A\Delta x\Delta t\sum_i \Delta H_i r_i$

The production of heat in the wash coat is the result of the reactions taking place. ΔH_i is the reaction heat for reaction i.

Out: $AV_{out}\Delta t$

The diffuse energy flow is the only term going out from the control volume during time Δt.

Accumulation: $A\Delta x(1-\varepsilon_{wc})\rho_{wc}C_{p,wc}\left(T_{wc}|_{t+\Delta t} - T_{wc}|_t\right)$

The accumulation term describes the change in energy during time Δt. ρ_{wc} is the wash coat density, and $C_{p,wc}$ is the wash coat heat capacity. Inserting the above into Equation (3.1) gives

$$AV_{in}\Delta t + A\Delta x\Delta t\sum_i \Delta H_i r_i = AV_{out}\Delta t + A\Delta x(1-\varepsilon_{wc})\rho_{wc}C_{p,wc}\frac{(T_{wc}|_{t+\Delta t} - T_{wc}|_t)}{\Delta t} \tag{3.20}$$

This can be rearranged to

$$\frac{(T_{wc}|_{t+\Delta t} - T_{wc}|_t)}{\Delta t} = \frac{1}{(1-\varepsilon_{wc})\rho_{wc}C_{p,wc}}\frac{(V_{in}-V_{out})}{\Delta x} + \frac{1}{(1-\varepsilon_{wc})\rho_{wc}C_{p,wc}}\sum_i \Delta H_i r_i \tag{3.21}$$

Letting $\Delta z \to 0$, $\Delta t \to 0$ gives

$$\frac{\partial T_{wc}}{\partial t} = -\frac{1}{(1-\varepsilon_{wc})\rho_{wc}C_{p,wc}}\frac{\partial V}{\partial x} + \frac{1}{(1-\varepsilon_{wc})\rho_{wc}C_{p,wc}}\sum_i \Delta H_i r_i \tag{3.22}$$

The term $\frac{\partial V}{\partial x}$ can be rewritten using Fouriers law in Equation (3.23)

$$V = -\lambda\frac{\mathrm{d}T}{\mathrm{d}x} \tag{3.23}$$

This gives the final equation for the wash coat temperature

$$\frac{\partial T_{wc}}{\partial t} = \frac{\lambda_{wc}}{(1-\varepsilon_{wc})\rho_{wc}C_{p,wc}}\frac{\partial^2 T_{wc}}{\partial x^2} + \frac{1}{(1-\varepsilon_{wc})\rho_{wc}C_{p,wc}}\sum_i \Delta H_i r_i \tag{3.24}$$

Equation (3.24) is a second order PDE and requires two BCs, and ICs to be solved.

$$\left.\frac{\partial T_{wc}}{\partial x}\right|_{x=0} = -\frac{h_{heat}}{\lambda}(T_b - T_{wc,s}) \tag{3.25}$$

$$\left.\frac{\partial T_{wc}}{\partial x}\right|_{x=L_{wc}} = 0 \tag{3.26}$$

$$T_{wc}(0,x) = T_{wc}^0(x) \tag{3.27}$$

Equations (3.25) and (3.26) are the BCs. The first one ensures that the conservation of energy is maintained at the bulk-wash coat interface. The second states that at the bottom of the wash coat, there is no temperature gradient. The reason for this is the same as for the BC in Equation (3.18). Equation (3.27) is the IC for the system. It states that at the beginning, the wash coat has a certain temperature.

3.2.3 Summary of Model 1

To conclude Section 3.2, and make an overview easier for the reader, all model equations, boundary conditions, and initial conditions are given for Model 1.

$$\frac{\partial c_{b,i}}{\partial t} = -u\frac{\partial c_{b,i}}{\partial z} - \frac{4k_g}{b}(c_{b,i} - c_{wc,s,i}) \tag{3.28}$$

$$\frac{\partial T_b}{\partial t} = -u\frac{\partial T_b}{\partial z} - -\frac{4h_{heat}}{b\rho_b C_{p,b}}(T_b - T_{wc,s}) \tag{3.29}$$

$$\frac{\partial c_{wc,i}}{\partial t} = \frac{1}{(1-\varepsilon_{wc})}D_{wc}\frac{\partial^2 c_{wc,i}}{\partial x^2} + \frac{1}{(1-\varepsilon_{wc})}\sum_i r_i \tag{3.30}$$

$$\frac{\partial T_{wc}}{\partial t} = \frac{\lambda_{wc}}{(1-\varepsilon_{wc})\rho_{wc}C_{p,wc}}\frac{\partial^2 T_{wc}}{\partial x^2} + \frac{1}{(1-\varepsilon_{wc})\rho_{wc}C_{p,wc}}\sum_i \Delta H_i r_i \tag{3.31}$$

$$c_{b,i}(t,0) = c_{in,i}(t) \tag{3.32}$$

$$c_{b,i}(0,z) = c^0_{b,i}(z) \tag{3.33}$$

$$T_b(t,0) = T_{in}(t) \tag{3.34}$$

$$T_b(0,z) = T^0_b(z) \tag{3.35}$$

$$\left.\frac{\partial c_{wc,i}}{\partial x}\right|_{x=0} = -\frac{k_g}{D_{wc,i}}(c_{b,i} - c_{wc,s,i}) \tag{3.36}$$

$$\left.\frac{\partial c_{wc,i}}{\partial x}\right|_{x=L_{wc}} = 0 \tag{3.37}$$

$$c_{wc,i}(0,x) = c^0_{wc,i}(x) \tag{3.38}$$

$$\left.\frac{\partial T_{wc}}{\partial x}\right|_{x=0} = -\frac{h_{heat}}{\lambda}(T_b - T_{wc,s}) \tag{3.39}$$

$$\left.\frac{\partial T_{wc}}{\partial x}\right|_{x=L_{wc}} = 0 \tag{3.40}$$

$$T_{wc}(0,x) = T^0_{wc}(x) \tag{3.41}$$

3.3 Model 2 - Convection Model

This section will present Model 2, that includes more simplifications than Model 1. The assumptions are the ones presented in assumption list M1 in Section 3.2, and additionally:

M2.A1 No internal mass and heat transfer limitations.

M2.A1 includes both temperature and concentration gradients. Even though the modelling of the SCR monolith has been studied extensively, no consensus has been reached if it is important to include the concentration gradient inside the wash

coat in the model. Colombo et al. [26] shows that under some conditions, the wash coat gradients in an SCR catalyst layer are minor. The temperature gradients are, due to the much higher heat conduction than mass diffusion, smaller than the concentration gradients. To make an initial analysis of the accuracy of the assumption, the thiele modulus and efficiency factor for NO in the standard SCR reaction will be analysed. The thiele modulus for a first order reaction is [40]:

$$\phi = L\sqrt{\frac{k}{D_{eff}}} \tag{3.42}$$

where L is the thickness of the monolith wash coat, k is the reaction rate as defined in (3.78), and D_{eff} is the effective diffusion coefficient. The studied catalyst has a wash coat thickness of $L = 0.0002$ m, and a porosity of $\varepsilon = 0.4$, and a tortuosity $\tau = 3$. D_{eff} can be approximated as:

$$D_{eff} = \frac{\varepsilon}{\tau} D \tag{3.43}$$

where D is the diffusion coefficient for NO in air at 300 ^{o}C, estimated using the Wilke and Lee method [98]. Using parameter values for the standard SCR reaction from Table 4.2, $k = 352.3$ s^{-1} at 300 ^{o}C. Using (3.42) with the specified values gives a thiele modulus of $\phi = 0.77$. From this, the efficiency factor η can be calculated for a slab as:

$$\eta = \frac{\tanh\phi}{\phi} \tag{3.44}$$

which gives $\eta = 0.84$. A efficiency factor close to one means that nearly all available catalyst is being used, and thus limited internal mass transfer limitations are expected during typical operating conditions. It should be noted that the above analysis is based on the kinetic parameters that already include mass transfer limitations. The thiele modulus is however small, and the effect will be minor. Assump-

tions M1.A1 - M1.A7 and M2.A1, gives the following model

$$\frac{\partial c_{b,i}}{\partial t} = -u\frac{\partial c_{b,i}}{\partial z} - \frac{4k_g}{b}\left(c_{b,i} - c_{wc,i}\right) \tag{3.45}$$

$$\frac{\partial c_{wc,i}}{\partial t} = \frac{4k_g}{b}\left(c_{b,i} - c_{wc,i}\right) + \sum_i r_i \tag{3.46}$$

$$\frac{\partial T_b}{\partial t} = -u\frac{\partial T_b}{\partial z} - \frac{4h_{heat}}{b\rho_b c_{p,b}}\left(T_b - T_{wc}\right) \tag{3.47}$$

$$\frac{\partial T_{wc}}{\partial t} = \frac{4h_{heat}}{b\rho_{wc} c_{p,wc}}\left(T_b - T_{wc}\right) + \sum_i \Delta H_{r,i} r_i \tag{3.48}$$

$$c_{b,i}(t,0) = c_{in,i}(t) \tag{3.49}$$

$$T_b(t,0) = T_{in}(t) \tag{3.50}$$

$$c_{b,i}(0,z) = c^0_{b,i}(z) \tag{3.51}$$

$$c_{wc,i}(0,z) = c^0_{wc,i}(z) \tag{3.52}$$

$$T_b(0,z) = T^0_b(z) \tag{3.53}$$

$$T_{wc}(0,z) = T^0_{wc}(z) \tag{3.54}$$

The system of equations is made up of two PDEs and two Ordinary Differential Equations (ODE). The PDEs are first order and requires one BC each to be solved. All of the equations requires ICs to be solved. If Equations (3.45) to (3.48) are compared to Model 1 Equations (3.4) to (3.24), it can be seen that the two equations describing the bulk states are the same for the two models. The equations for the wash coat states have changed, and Equations (3.46) and (3.48) no longer have the mass diffusion term and the heat conduction term. The wash coat is being treated as a surface. To ensure that the conservation of mass is still valid, the film transfer terms in (3.45) and (3.47), that for Model 1 appeared in the BCs for the wash coat equations, now appear in Equations (3.46) and (3.48). By reducing Equations (3.16) and (3.24) to ODEs, the model has been reduced substantially in complexity. Model 2 will be the primary model of focus throughout this thesis, because of its proven usefulness at predicting SCR dynamics, and that it has reasonable simulation times for transient test cycles.

3.4 Model 3 - No Mass Transfer Model

This section will present Model 3, which includes additional simplifications compared to Model 2. In addition to the assumptions presented in lists M1 and M2, the following assumption is added:

M3.A1 Instantaneous mass transfer from bulk phase to wash coat

The effect of M3.A1 is that there is no difference in concentration between the bulk phase and wash coat phase, and they can be considered the same. The reaction rates will be calculated according the bulk concentration instead of the wash coat concentration. The impact of the simplification depends on the importance of mass transfer. If $k_g \to \infty$ in Equation (3.46), the derivative term will take a large value, and the difference in concentration between the wash coat and bulk disappears. The reaction term can be moved to Equation (3.45), which gives the final Model 3:

$$\frac{\partial c_{b,i}}{\partial t} = -u\frac{\partial c_{b,i}}{\partial z} + \sum_i r_i \tag{3.55}$$

$$\frac{\partial T_b}{\partial t} = -u\frac{\partial T_b}{\partial z} - \frac{4h_{heat}}{b\rho_b c_{p,b}}(T_b - T_{wc}) \tag{3.56}$$

$$\frac{\partial T_{wc}}{\partial t} = \frac{4h_{heat}}{b\rho_{wc} c_{p,wc}}(T_b - T_{wc}) + \sum_i \Delta H_{r,i} r_i \tag{3.57}$$

$$c_{b,i}(t,0) = c_{in,i}(t) \tag{3.58}$$

$$T_b(t,0) = T_{in}(t) \tag{3.59}$$

$$c_{b,i}(0,z) = c^0_{b,i}(z) \tag{3.60}$$

$$T_b(0,z) = T^0_b(z) \tag{3.61}$$

$$T_{wc}(0,z) = T^0_{wc}(z) \tag{3.62}$$

3.5 Model 4 - No Heat Transfer and Thermal Mass Model

This section will present a model that considers no difference between wash coat and bulk phase temperature. The model does not consider the wash coat to have any thermal mass either. The effect of this simplification is that reaction rates are calculated using the gas phase temperature. The temperature difference between the wash coat and gas that might be prominent during very transient behaviour, does not exist, which can lead to an inaccurate reaction temperature. The simplification also removes the smoothing of the temperature throughout the monolith channel, leading to substantial temperature variations inside the monolith during a transient simulation. The effect of reducing the thermal mass of the wash coat means that the accumulation of energy will only be in the gas phase. The additional assumptions compared to Model 2 are:

M5.A1 Instantaneous heat transfer from bulk to wash coat

M5.A2 Wash coat has no thermal mass

M5.A3 No reaction heat

The model can be summarized as:

$$\frac{\partial c_{b,i}}{\partial t} = -u\frac{\partial c_{b,i}}{\partial z} - \frac{4k_g}{b}\left(c_{b,i} - c_{wc,i}\right) \tag{3.63}$$

$$\frac{\partial c_{wc,i}}{\partial t} = \frac{4k_g}{b}\left(c_{b,i} - c_{wc,i}\right) + \sum_i r_i \tag{3.64}$$

$$\frac{\partial T_b}{\partial t} = -u\frac{\partial T_b}{\partial z} \tag{3.65}$$

$$c_{b,i}(t,0) = c_{in,i}(t) \tag{3.66}$$

$$T_b(t,0) = T_{in}(t) \tag{3.67}$$

$$c_{b,i}(0,z) = c^0_{b,i} \tag{3.68}$$

$$c_{wc,i}(0,z) = c^0_{wc,i} \tag{3.69}$$

$$T_b(0,z) = T^0_b \tag{3.70}$$

The difference from Model 2 is that the equation for wash coat temperature no longer exists. The transfer term in the gas phase temperature equation has been removed. It can also be seen that when comparing to Model 4, the energy balance here does not include the mass of the wash coat.

3.6 Model 5 - No Mass Transfer, Heat Transfer, and Thermal Mass Model

This section presents the most simplified model. The model does not consider any gradients between the wash coat and the bulk phase, nor any thermal mass. The effect of the simplifications will be the combined effects from Models 3 and 5. The additional assumptions compared to Model 2 are:

M6.A1 Instantaneous mass transfer from bulk phase to wash coat

M6.A2 Instantaneous heat transfer from bulk to wash coat

M6.A3 Wash coat has no thermal mass

M6.A4 No reaction heat

The model can be summarized as:

$$\frac{\partial c_{b,i}}{\partial t} = -u\frac{\partial c_{b,i}}{\partial z} + \sum_i r_i \tag{3.71}$$

$$\frac{\partial T_b}{\partial t} = -u\frac{\partial T_b}{\partial z} \tag{3.72}$$

$$c_{b,i}(t,0) = c_{in,i}(t) \tag{3.73}$$

$$T_b(t,0) = T_{in}(t) \tag{3.74}$$

$$c_{b,i}(0,z) = c^0_{b,i} \tag{3.75}$$

$$T_b(0,z) = T^0_b \tag{3.76}$$

3.7 Kinetic Model

In this work a global kinetic model approach was adopted, where the major reactions influencing the chemistry were:

$$NH_3 + S \leftrightharpoons S - NH_3 \tag{R1}$$

$$2S - NH_3 + 5/2O_2 \rightarrow 2NO + 3H_2O + 2S \tag{R2}$$

$$4S - NH_3 + 4NO + O_2 \rightarrow 4N_2 + 6H_2O + 4S \tag{R3}$$

$$2S - NH_3 + NO + NO_2 \rightarrow 2N_2 + 3H_2O + 2S \tag{R4}$$

$$2S - NH_3 + 2NO_2 \rightarrow N_2 + N_2O + 3H_2O + 2S \tag{R5}$$

where (R1) is the adsorption/desorption equlibrium reaction, (R2) is the NH_3 oxidation into NO, (R3) is the standard SCR reaction, (R4) is the fast SCR reaction, and (R5) is the N_2O formation reaction. S represents an empty catalyst site, and S-NH_3 an adsorbed ammonia molecule. For the adsorption/desorption mechanism, the commonly used Eley-Rideal mechanism was adopted. In (R2) it was assumed that NH_3 was only oxidised into NO. This was done to explain the fact that NO is present in the outlet of the catalyst when only diluted NH_3 is in the inlet. The frequently used NH_3 oxidation reaction that only produces N_2 was not included in this work, to reduce the calibration effort, and the fact that it was not needed to achieve good calibration results. Due to limitations in experimental data that will be explained in Chapter 4, it was decided to exclude the reaction refered to as the slow SCR, which converts NO_2 into N_2. This is not expected to reduce the predictive capabilities substantially. There are conditions where the exhaust system runs at NO_2/NO ratios over 1, this is however normally not desired, and under the normal Euro VI setup as seen in Figure 1.5, a DPF is placed in front of the SCR, thereby reducing the NO_2 levels through passive filter generation [81].

The reaction rates were modelled as:

$$r_j = k_j \cdot \prod_{i=1}^{N} c_i \tag{3.77}$$

where N is the number of relevant species c_i in reaction r_j, from Table 3.1. The parameter k_j was modelled according to the Arrhenius equation.

$$k_j = k_{0,j} \exp\left(\frac{-E_{a,j}}{RT}\right) \tag{3.78}$$

where $k_{0,j}$ is the pre exponential factor of reaction j, $E_{a,j}$ is the activation energy of reaction j, R is the universal gas constant, and T is the reaction temperature. A potential problem with the Arrhenius expression is that there often is a strong correlation between the pre-exponential factor and the activation energy. This problem can be reduced and sometimes removed by centering the expression around a temperature T_0. This was adopted here:

$$k = k_0 \exp\left(\frac{-E_a}{RT}\right) \tag{3.79}$$

$$= k_0 \exp\left(\frac{-E_a}{RT_0}\right) \cdot \exp\left(\frac{-E_a}{R}\left(\frac{1}{T} - \frac{1}{T_0}\right)\right) \tag{3.80}$$

$$= k_{0,ref} \exp\left(\frac{-E_a}{R}\left(\frac{1}{T} - \frac{1}{T_0}\right)\right) \tag{3.81}$$

where T_0 is the temperature around which the expression is centered. T_0 was in this work chosen as 300 ^{o}C. The kinetic parameters presented in Chapter 4 have been recalculated to k_0. This was done for all Arrhenius expressions except for the desorption equation.

The activation energy for the desorption reaction was chosen to be coverage dependent, as done in [115, 90, 124].

$$E_{a,des} = E_{a,0,des}(1 - \alpha\theta) \tag{3.82}$$

where $E_{a,0,des}$ is the independent activation energy for the desorption reaction, α is the coverage dependency factor, and θ is the coverage ratio. The use of coverage dependent activation energies is not necessarily physically true for oxide based catalysts, due to individual adsorption sites, but has been used for example in [87]. The application here has however been successful. The time dependent coverage ratio was modelled as:

$$\frac{d\theta}{dt} = \frac{1}{\Omega_{max}} \sum_{j=N_A} r_j \tag{3.83}$$

where Ω_{max} is the maximum coverage capacity at 150 ^oC in mol/m^3, and N_A are the reactions where adsorbed NH_3 is involved, which in this model are all listed in

Table 3.1. Kinetic model equations that are used together with a physical model. The table shows the reaction name, the equation for calculating the reaction speed, and the kinetic parameters that need to be estimated.

Reaction	**Equation**	**Kinetic parameters for calibration**
Adsorption	$k_{ads}(1-\theta)c_{NH_3,wc}$	k_{ads}
Desorption	$k_{des}\exp(-E_{des}(1-\alpha\theta)/RT)\theta$	k_{des}, E_{des}, α
Standard SCR	$k_{standard}\exp(-E_{standard}/RT)c_{NO,wc}\theta$	$k_{standard}, E_{standard}$
Fast SCR	$k_{fast}\exp(-E_{fast}/RT)c_{NO,wc}c_{NO_2,wc}\theta$	k_{fast}, E_{fast}
NH_3 oxidation	$k_{ox}\exp(-E_{ox}/RT)\theta$	k_{ox}, E_{ox}
N_2O formation	$k_{N_2O}\exp(-E_{N_2O}/RT)c_{NO_2}\theta$	k_{N_2O}, E_{N_2O}

Table 3.1. The full kinetic model is shown in Table 3.1. As seen, the model includes 12 kinetic parameters that needs to be calibrated, which is explained in Chapter 4.

3.8 Model Parameters

The models presented in Sections 3.2 to 3.7 contains many parameters that needs to be estimated with various methods. The parameters related to the kinetic model in Section 3.7 will not be presented here, but in Chapter 4, together with the calibration methodology. Parameters that does not need to be estimated are presented in Table 3.2.

Table 3.2. Physical parameters used in the model.

Parameter	**Value**
Hydraulic diameter, d_{hyd} (b) [mm]	1.16
Gas phase density, ρ_b [kg/m^3] (at 0 ^{o}C, updated with T)	1.276
Average gas heat capacity, $C_{p,b}$ [kJ/kg/K]	1.0
Wash coat density, ρ_{wc} [kg/m^3]	700
Heat capacity wash coat, $C_{p,wc}$ [kJ/kg/K]	1.0

3.8.1 Diffusion Coefficients

This section will present the estimation procedure of the gas diffusion coefficients, and the wash coat diffusion coefficients.

3.8.1.1 Gas Diffusion

The diffusion coefficients are estimated using the Wilke and Lee method [98]. This equation is valid for diffusion coefficients in gas systems at low pressures. The diffusion of species A in B (or equivalently B in A) is:

$$D_{AB} = \frac{[3.03 - (0.98\sqrt{M_{AB}}]10^{-3})T^{3/2}}{P\sqrt{M_{AB}}\sigma_{AB}^2\Omega_D} \tag{3.84}$$

where

$$\begin{aligned}
D_{AB} &= \text{binary diffusion coefficient } [\text{cm}^2/\text{s}] \\
T &= \text{temperature [K]} \\
M_A, M_B &= \text{molecular weights of A and B [g/mol]} \\
M_{AB} &= 2\left[1/M_A + 1/M_B\right]^{-1} \\
P &= \text{pressure [bar]} \\
\sigma_A &= 1.18V_b^{1/3} \\
\sigma_{AB} &= \frac{\sigma_A + \sigma_B}{2} \\
V_b &= \text{liquid molar volume at boiling point(1 atm) temperature } [\text{cm}^3/\text{mol}]
\end{aligned}$$

σ_A is the characteristic Lennard-Jones length for species A, and σ_{AB} is the average characteristic Lennard-Jones length for species A and B. Ω_D is determined from:

$$\Omega_D = \frac{1.06036}{(T^*)^{0.15610}} + \frac{0.19300}{\exp(0.47635T^*)} + \frac{1.03587}{\exp(1.52996T^*)} + \frac{1.76474}{\exp(3.89411T^*)} \tag{3.85}$$

where

$$T^* = k_B T/\varepsilon_{AB} \tag{3.86}$$

$$\varepsilon_{AB} = \sqrt{\varepsilon_A \varepsilon_B} \tag{3.87}$$

and ε_A is the characteristic Lennard-Jones energy and k_B is the Boltzmann constant

3.8.1.2 Wash Coat Diffusion

There are several methods to estimate the wash coat diffusion coefficients, that depend on what kind of pores that are present in the wash coat. If the pores are of micro scale, it is common to use the porosity ε, and tortuosity τ [85]:

$$D_{eff} = D_{AB}\frac{\varepsilon}{\tau} \tag{3.88}$$

which is the method that has been used in this work. If the pores are smaller, such that the length scale of the pore diameter is comparable to the mean free path of the particles, Knudsen diffusion can be used:

$$D_{K,A} = 48.5 d_p \sqrt{\frac{T}{M_A}} \tag{3.89}$$

where

$$\begin{aligned} D_{K,A} &= \text{knudsen diffusion coefficient for A [m}^2\text{/s]} \\ d_p &= \text{pore diameter [m]} \\ T &= \text{temperature [K]} \\ M_A &= \text{molecular mass [g/mol]} \end{aligned}$$

If the wash coat contains a broad variety of pore sizes, a combination of the methods can be used.

3.8.2 Viscosity

The viscosity is needed to estimate the heat conduction, which is in turn needed to estimate the heat transfer coefficients. A method based on a reduced, dimensionless viscosity is used [98]:

$$\eta_r = \xi \eta = f(T_r) \tag{3.90}$$

where T_r is the reduced temperature, and ξ is the reduced, inverse viscosity

$$T_r = \frac{T}{T_c} \tag{3.91}$$

$$\xi = 0.176 \left(\frac{T_c}{M^3 P_c^4} \right)^{1/6} \tag{3.92}$$

where

$$\begin{aligned} T_c &= \text{critical temperature [K]} \\ M &= \text{molecular weight [g/mol]} \\ P_c &= \text{critical pressure [bar]} \end{aligned}$$

The viscosity can thus be estimated using the reduced viscosity, and the reduced temperature. $\xi\eta$ is estimated as:

$$\xi\eta = \left[0.807 T_r^{0.618} - 0.357 \exp(-0.449 T_r) + 0.340 \exp(-4.058 T_r) + 0.018 \right] F_P^o F_Q^o \tag{3.93}$$

where F_P^0 and F_Q^0 are correction terms to account for polarity and quantum effects. F_Q^0 is used for quantum gases He, H_2 and D_2, and is of no interest in this application. F_P^0 is determined as:

$$F_P^o = 1 \qquad 0 \leq \mu_r < 0.022 \tag{3.94}$$

$$F_P^o = 1 + 30.55(0.292 - Z_c)^{1.72} \qquad 0.022 \leq \mu_r < 0.075 \tag{3.95}$$

$$F_P^o = 1 + 30.55(0.292 - Z_c)^{1.72}\,|0.96 + 0.1(T_r - 0.7)| \qquad 0.075 \leq \mu_r \tag{3.96}$$

where

$$Z_c = \frac{P_c V_c}{R T_c} \tag{3.97}$$

$$\mu_r = 52.46 \frac{\mu^2 P_c}{T_c^2} \tag{3.98}$$

The viscosity can now be estimated as:

$$\eta = \frac{\xi \eta}{\xi} \tag{3.99}$$

where the viscosity η will have the unit μP.

3.8.3 Heat Capacity

The heat capacity is estimated at constant pressure as:

$$\frac{C_p}{R} = a_0 + a_1 T + a_2 T^2 + a_3 T^3 + a4 T^4 \tag{3.100}$$

where the constants a_i, $i = 0, 1, .., 4$ are specific to the gas and can be found in [98].

3.8.4 Heat Conduction

To estimate the axial heat conduction, a modified Eucken model is used [98]:

$$\frac{\lambda M}{\eta C_v} = 1.15 + \frac{2.03}{C_v / R} \tag{3.101}$$

where

$$\lambda = \text{thermal conductivity [W/m} \cdot \text{K]}$$

$$M = \text{molecular weight [kg/mol]}$$

$$\eta = \text{viscosity [Pa} \cdot \text{s]}$$

$$C_v = \text{heat capacity at constant volume [J/mol} \cdot \text{K]}$$

$$R = \text{ideal gas constant [J/mol} \cdot \text{K]}$$

If the gas is assumed idea, C_p can be calculated from C_v:

$$C_v = C_p - R \tag{3.102}$$

3.8.5 Reaction Heat

The heat of reaction is calculated from the heat of formation of the separate species taking part in the reaction, as in:

$$\Delta H_r = \Delta H_{f,Products} - \Delta H_{f,Reactants} \tag{3.103}$$

The reaction heat for the adsorption and desorption reactions has been assumed to be zero.

3.8.6 Film Transfer Coefficients

The mass and heat transfer coefficients are calculated using the Sherwood number Sh and the Nusselt number Nu, respectively. This comes from the following relations:

$$k_g = \frac{Shd_{hyd}}{D} \tag{3.104}$$

$$h_{heat} = \frac{Nu\lambda}{L} \tag{3.105}$$

where the symbols are as previously explained.

The Sherwood and Nusselt number needs to be approximated, and there are a broad variety of methods for this. For laminar flow, it is common to use the infinite Sherwood and Nusselt numbers, Sh_∞ and Nu_∞, which takes different values for different geometrical shapes. Table 3.3 shows Sh_∞ and Nu_∞ values for some common channel shapes. In this work, the monolith channels are sinusoidal, and

Table 3.3. Infinite Sherwood and Nusselt numbers for some common channel shapes [130].

Shape	Sh_∞, Nu_∞
Circular	3.66
Square	2.98
Triangular	2.98
Rectangular	3.39
Sinusoidal	2.97
Hexagonal	3.34

2.97 has been chosen as the infinite Sherwood and Nusselt number.

Depending on operating conditions in the monolith, the flow can develop from turbulent at the entrance to laminar. If the flow is turbulent for a considerable length of the channel, position dependent Sherwood and Nusselt numbers have to

be used. An example of how to solve this is by analogy with the Graetz-Nusselt problem for developing laminar flow [17, 131, 50]

$$Sh = Sh_\infty + 8.827(1000 z_{mt})^{-0.545} e^{-48.2 z_{mt}} \tag{3.106}$$

$$Nu = Nu_\infty + 8.827(1000 z_{ht})^{-0.545} e^{-48.2 z_{ht}} \tag{3.107}$$

where

$$z_{mt} = \frac{xD}{ud_{hyd}^2} \tag{3.108}$$

$$z_{ht} = \frac{x\lambda}{ud_{hyd}^2 c_{p,b}\rho_b} \tag{3.109}$$

Another alternative is to use the Hawthorn correlation, which provides length averaged Sherwood and Nusselt numbers:

$$Sh = Sh_\infty \left(1 + 0.095 \frac{d_{hyd}}{L} ReSc\right)^{0.45} \tag{3.110}$$

$$Nu = Nu_\infty \left(1 + 0.095 \frac{d_{hyd}}{L} RePr\right)^{0.45} \tag{3.111}$$

where Re is the Reynolds number, Sc is the schmidt number, and Pr is the Prandtl number.

3.8.6.1 Mass Transfer Analysis

To analyse how the flow is developing in the SCR channel under normal operating conditions, Equation (3.112) will be used to see how far into the channel the flow is fully developed. The flow is fully developed if [100]

$$z \geq \frac{Pe}{Sc^{1/3}} \left(\frac{1.4}{Sh_\infty}\right)^2 \tag{3.112}$$

where

$z =$ dimensionless coordinate along the length of the channel [-]

$Pe =$ transverse Peclet number [-]

$Sc =$ Schmidt number [-]

Applying Equation (3.112) to the modelled system under realistic operating conditions gives $z = 0.065$. This means that the flow is fully developed 6.5 % into the channel. For this work, the Hawthorn relation has been used.

3.9 Model Implementation

The equations that have been shown previously in this chapter are all PDEs and ODEs. The PDEs requires both discretisation in space and time to be solved. This is a common problem in chemical engineering, and there are well established methods to solve these kinds of problems. This section will present the programming structure, the methods that has been used, and illustrate them with an example.

3.9.1 Program Structure

A non-trivial part of the solution of the presented models is the organisation of the program. It has to ensured that the program is easily understood, and that parts of the model can be easily changed to new ones, for example channel models and kinetic models. Figure 3.5 shows a schematic overview of how the code has been implemented. The call function is the main script where the user defines

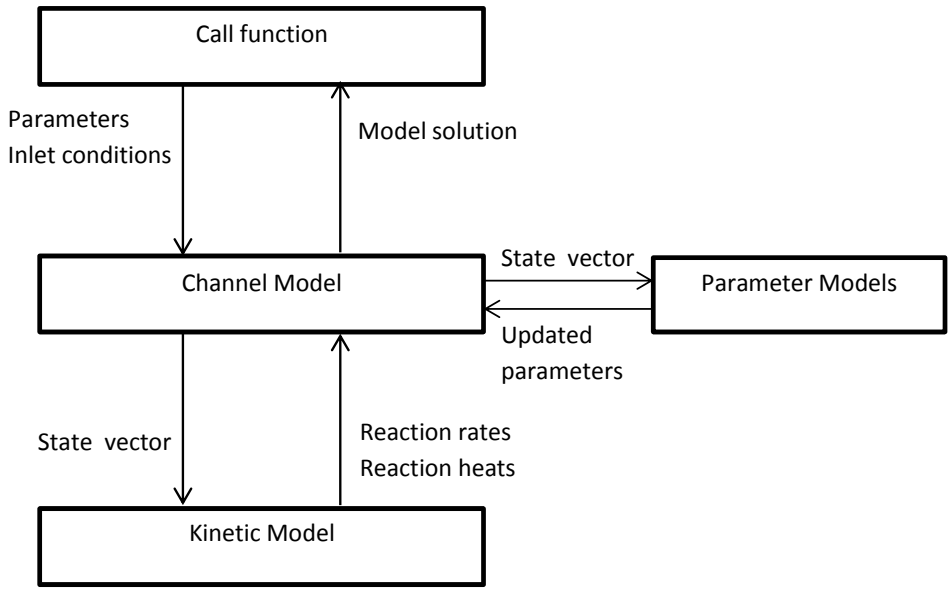

Figure 3.5. Schematic view of code structure. Three main sections are used: Call function, channel model, and kinetic model.

which channel model, kinetic model, and parameter models that should be used. The parameters that are independent of catalyst conditions are also defined, such as the monolith length etc. The discretisation method is also chosen in the call function, and the corresponding matrices are created. In a transient simulation

the call function is called every sampling time, thus updating the monolith inlet conditions. The channel model file contains the channel equations. The equations are discretised, and the time derivatives are solved for. The channel model file calls the kinetic model, and passes the state values so that the reaction rates and reaction heats can be calculated with the current conditions. The file also updates the parameters that are condition dependent, such as the mass and heat transfer coefficients. The presented structure ensures that it is easy to change between different channel models, kinetic models, and parameter models.

3.9.2 Method of Lines

The Method of Lines (MOL) is a method that involves reducing a initial boundary value problem, such as the ones encountered in this work, into a system of ODEs, by discretising the space derivatives [74, 112]. The remaining system of ODEs can be solved using standard ODE solvers, such as ODE15s in Matlab, which has been used in this work. A major advantage of the MOL is that it has good stability, and that it is possible to use high order discretisation methods in the spatial derivatives without a big increase in the computational complexity [112]. Using the MOL, the time dependent diffusion equation, as seen in Equation (3.113) can be written as Equation (3.114).

$$\frac{\partial c}{\partial t} = \frac{\partial^2 c}{\partial x^2} + q(x,t) \tag{3.113}$$

$$\frac{\partial c_i}{\partial t} = \mathbb{D}\left(\frac{\partial^2 c}{\partial x^2}\right) + q(x_i,t) \tag{3.114}$$

where c is the concentration, q is a function describing a relation between x and t, and $\mathbb{D}$ is a discretisation of the spatial derivative, for example one of the methods shown in Section 3.9.3. The equation has been discretised in the spatial derivative, and thus a system of ODEs remain to solve using a standard ODE solver.

3.9.3 Finite Difference Method

As seen in Section 3.9.2 the spatial derivatives needs to be discretised manually. There are several well established methods for this, for example the Finite Difference Method (FDM), Finite Volume Method (FVM) and the Finite Element Method (FEM). In this work the FDM has been used [55]. The FDM can be derived through taylor expansions. Given a domain as in Figure 3.6, and a function f to describe

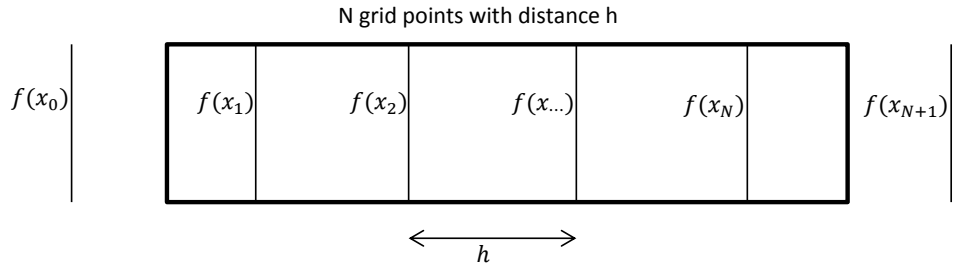

Figure 3.6. General channel domain and its grid points.

the states, a taylor expansion around point $i-h$ gives

$$f(i-h) = f(i) - f'(i)h + R_2(x) \tag{3.115}$$

$$f'(i) \approx \frac{f(i) - f(i-h)}{h} \tag{3.116}$$

where h is the discretisation point length, and $R_2(x)$ is the second order error term. The above expansion has resulted in a first order backward differentiation. In the example above the error term is second order. Depending on how complicated the discretisation method is, the error can be higher order as well.

3.9.3.1 Example - Warm Flow Parallel to Wall

To illustrate the Method of Lines and the Finite Difference Method, an example is presented. Consider the scenario in Figure 3.7. A flow with the temperature T_{flow} is flowing parallel to a wall with temperature $T(t,z)$. The temperature is dependent on the z-coordinate and a temperature profile will be present. The equations describing the wall temperature are:

$$\frac{\partial T}{\partial t} = \frac{\lambda}{\rho C_p}\frac{\partial^2 T}{\partial z^2} \tag{3.117}$$

$$\left.\frac{\partial T}{\partial z}\right|_{z=0} = \frac{k}{\lambda}\left(T|_{z=0} - T_{flow}\right) \tag{3.118}$$

$$\left.\frac{\partial T}{\partial z}\right|_{z=L} = 0 \tag{3.119}$$

$$T(0,z) = T_0 \tag{3.120}$$

The spatial derivative will be discretised with a second order central difference scheme, and the boundary conditions included in the solution. The goal is to represent the resulting system of ODEs as:

$$\frac{\mathrm{d}}{\mathrm{d}t}\mathbf{x} = (\mathbf{A}x + \mathbf{A}_b(\mathbf{B}_1\mathbf{x} + \mathbf{B}_0)) \tag{3.121}$$

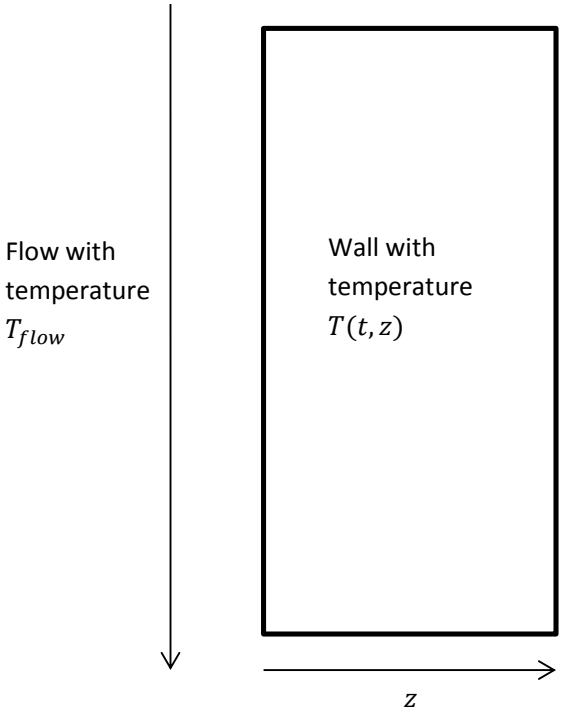

Figure 3.7. Discretisation Example - A flow with temperature T_{flow} flows parallel to a wall with temperature $T(t,z)$.

where $\mathbf{A}$ is the matrix describing the general discretisation, $\mathbf{A}_b$ determines which boundary conditions that are used, $\mathbf{B}_1$ describes the relation between the boundary conditions and the states, and $\mathbf{B}_0$ desribes the constant values of the boundary conditions.

Introducing the discretisation of the spatial derivative, the system becomes:

$$\frac{\mathrm{d}T_i}{\mathrm{d}t} = \frac{\lambda}{\rho C_p}\frac{T_{i+1} - 2T_i + T_{i-1}}{h^2} \tag{3.122}$$

From the boundary conditions follows:

$$\left.\frac{\partial T}{\partial z}\right|_{z=0} = \frac{k}{\lambda}\left(T|_{z=0} - T_{flow}\right) \tag{3.123}$$

$$\Rightarrow \frac{T_1 - T_0}{h} = \frac{k}{\lambda}\left(\frac{T_1 + T_0}{2} - T_{flow}\right) \tag{3.124}$$

$$\Rightarrow T_0 = \frac{2\lambda - hk}{2\lambda + hk}T_1 + \frac{2hk}{2\lambda + hk}T_{flow} \tag{3.125}$$

$$\left.\frac{\partial T}{\partial z}\right|_{z=0} = 0 \tag{3.126}$$

$$\Rightarrow \frac{T_{N+1} - T_N}{h} = 0 \tag{3.127}$$

$$\Rightarrow T_{N+1} = T_N \tag{3.128}$$

The complete system can now be formulated according to Equation (3.121):

$$\begin{aligned}\frac{\mathrm{d}}{\mathrm{d}t}\mathbf{T} = \frac{\lambda}{h^2\rho C_p}\Bigg(&\begin{bmatrix} -2 & 1 & 0 & & & \\ 1 & -2 & 1 & \ddots & & \\ 0 & 1 & -2 & \ddots & 0 & \\ & \ddots & \ddots & \ddots & 1 & 0 \\ & & 0 & 1 & -2 & 1 \\ & & & 0 & 1 & -2 \end{bmatrix}\begin{bmatrix} T_1 \\ T_2 \\ T_3 \\ T_4 \\ \vdots \\ T_N \end{bmatrix} + \\ &\begin{bmatrix} 1 & 0 \\ 0 & 0 \\ 0 & 0 \\ 0 & \vdots \\ \vdots & 0 \\ 0 & 1 \end{bmatrix}\left(\begin{bmatrix} \frac{2\lambda - hk}{2\lambda + hk} & 0 & 0 & 0 & \cdots & 0 \\ 0 & 0 & 0 & \cdots & 0 & 1 \end{bmatrix}\begin{bmatrix} T_1 \\ T_2 \\ T_3 \\ T_4 \\ \vdots \\ T_N \end{bmatrix} + \begin{bmatrix} \frac{2hk}{2\lambda + hk} T_{flow} \\ 0 \end{bmatrix}\right)\end{aligned} \tag{3.129}$$

The system of ODEs can now be solved with Matlabs ODE15s. The presented example is very close to the equations presented in this chapter, and therefore represents the discretisation challenges well that are encountered here.

3.10 Discussion

The models that has been presented in this chapter are expected to be able to predict the dynamics of the SCR monolith to different extents. Models 3 through 5 are expected to perform worse than models 1 and 2, since they include simplifications related to the physics of the monolith. Model 2 is not expected to perform worse than Model 1. The difference between the two is that internal mass transfer is not included in model 2, while it is in model 1. The reason to include intra porous diffusion is if the intrinsic kinetic parameters are of interest, or if it is of interest to analyse how concentration profiles look inside the catalyst wall. Not including intra porous diffusion will result in a situation where the efficiency factor is included in the kinetic parameters. This follows from:

$$r = \eta k c \tag{3.130}$$

Table 3.4. Summary of the properties of the models shown in this chapter. The table shows the dimensions the models consider, as well as the number of ODEs that has to be solved after discretisation, including the kinetic model. N is the number of bulk phase discretisation points, M is the number of wash coat discretisation points, and j is the number of species.

Model	Dimensions	Number of ODEs	Number of ODEs for $N = 10$, $M = 10$, $j = 5$
Model 1	1 + 1D	$N(j+1)+MN(j+2)$	760
Model 2	1 + 0D	$2Nj+3N$	130
Model 3	1 + 0D	$Nj+3N$	80
Model 4	1 + 0D	$2Nj+2N$	120
Model 5	1 + 0D	$Nj+2N$	70

for a first order reaction [40]. It is therefore expected that model 2 will be able to predict the SCR monolith as well, if not better, than model 1. The extra parameters that are needed in model 1 will result in more uncertainty, compared to if the internal diffusion related phenomena are included in the estimated kinetic parameters. Model 1 will contain a considerable amount more ODEs that needs to be solved, and will thus take longer to simulate. Table 3.4 shows the number of ODEs that needs to be solved for each model, including the kinetic model. M is the number of wash coat discretisation points, N is the number of bulk phase discretisation points, and j is the number of species. Table 3.4 also shows the number of ODEs for typical values of N, M, and j. As can be seen, the number of ODEs decreases substantially when the resolution in the washcoat is neglected. Since the expected accuracy is the same for models 1 and 2, and the fact that model 2 will be faster to solve, the main model used throughout the thesis will be model 2.

As seen in Table 3.4 the majority of the models are 1 + 0D. This means that the bulk phase is modelled as one-dimensional, while the wash coat is zero-dimensional, and considered a surface. Model 1 is stated as a 1 + 1D model since both the bulk phase and wash coat phase are modelled with one-dimension.

In this work it has been decided to focus more on the channel physics than the kinetic model, thus only one kinetic model has been used throughout the thesis. If a more complex kinetic model than the presented one had been chosen, it is possible that more chemical phenomena could be explained. It is however important to choose the kinetic model in relation to what data is available for calibration. As will be seen in Chapter 4, the experimental data will not allow for more reactions to be calibrated. In this work the main focus is on the global performance of the SCR

catalyst, and not the details. The complexity level of the kinetic model is therefore believed to be satisfactory.

3.11 Conclusions

Five SCR monolith models have been presented. Model 1 includes the least simplifications, while the other five models includes simplifications related to mass and heat transfer. A kinetic model has been presented that includes most of the relevant reactions taking place inside the monolith. The kinetic model will be used together with all the presented channel models. It is expected that the models, to varying degree, will be able to predict the dynamics of a full-scale SCR monolith. Models 1 and 2 will likely have the same accuracy, while the other models have simplifications that will decrease performance.

Chapter 4

Estimation of Kinetic Parameters for the SCR Catalyst

The methodology that has been used to estimate the kinetic parameters for the SCR catalyst is presented. The methodology uses bench-scale data and full-scale data. The experimental setup that was used to produce experimental data is presented along with the experimental data. The results shows that the estimation procedure was successful, however the adsorption and desorption related parameters needed to be corrected with full-scale data. Some of the simplified models are not calibrated with full-scale data, because of model analysis results presented in Chapter 6.

The main contribution of this chapter is published in two articles (A. Åberg, A. Widd, J. Abildskov, J. K. Huusom. Parameter Estimation and Analysis of an Automotive Heavy-duty SCR Catalyst Model. Chemical Engineering Science 161 (2017) 167-177), and (A. Åberg, A. Widd, J. Abildskov, J. K. Huusom. Estimation of Kinetic Parameters in an Automotive SCR Catalyst Model, Topics in Catalysis 59 (2016) 945-952).

4.1 Introduction

A necessary step in the development of a functioning model is to estimate its parameters. Since the reactions are the most important phenomena occurring in the monolith, is it of importance that they are estimated to such a degree that the model can be used. It is thus a commonly encountered problem when modelling the SCR catalyst, and much literature exists on the subject. Two main approaches are possible. Either a powder sample of the catalyst is used, which eliminates mass transfer limitations and makes it easier to get the intrinsic values of the parameters, or reactor experiments are used. Reactor experiments have the advantage that mass transfer conditions will be similar to those of the full-scale monolith. In this work, experimental data from a small scale reactor setup was available for use. In [115] reactor experiments were used to characterise and calibrate a high-fidelity model, similar to model 2 in this work. A complicated scheme of inlet conditions allowed the authors to successfully calibrate their model to predict NO, NO_2, and both gaseous and adsorbed NH_3. Other reactor based parameter estimations has been done for example in [23, 25]. Catalyst characterisation based on powder samples can be found for example in [87]. This chapter will present the parameter estimation of the kinetic model coupled with the channel models presented in Chapter 3. The methodology that has been used to calibrate the model is presented. As will be seen, the methodology contains several steps where different parameters are calibrated sequentially. Some of the channel models will not be calibrated. Due to reasons that will be discussed in Chapter 6, some models are not calibrated. For example, model 5 has not been calibrated at all. This chapter will present the steps that were carried out for the different models. The model that was calibrated first, and therefore presented first, is model 2, due to the appealing balance between complexity and accuracy. The chapter will also present the experimental setup and the experimental data that was used.

4.2 Experimental Setup

This section will present the experimental setup that was used to gather experimental data for the kinetic model calibration. A small scale monolith with length 3 inches and a diameter of 1.9 inches was used for producing experimental data. An overview of the experimental setup can be seen in Fig. 4.1. The full lines represent the actual flows, while the dotted lines represent data collection. The exhaust gases did not come from an engine, but were produced by mixing gases. The gases con-

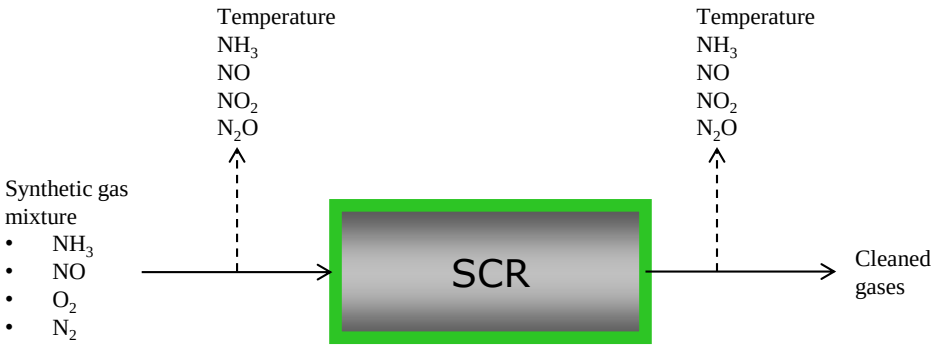

Figure 4.1. Simplified overview of reactor setup for collection of parameter estimation data. Dotted lines represent the measurements and full lines represent the actual flows. The inlet gas mixture also contained 5 vol-% O_2 and was balanced with N_2.

tained 5 vol-% H_2O, 10 vol-% O_2, and varying amounts of NO and NH_3, in different Ammonia-NOx-Ratios (ANR). The test consisted of three different sections:

1. **Diluted NH_3** - Feed with diluted NH_3, H_2O, and O_2.
2. **ANR 1.0** - Feed with diluted NH_3, NO, H_2O, and O_2, with ANR = 1.0.
3. **ANR 1.2** - Feed with NH_3, NO, H_2O, and O_2, with ANR = 1.2.

All NO_2 present was a result of the $NO \leftrightharpoons NO_2$ equilibrium. The tests were carried out isothermally, with different tests between 200^{o}C and 500^{o}C. The pre-set NO concentration was sent to the control unit and was used to calculate the NH_3 dosing. In a realistic application, this amount is calculated from control algorithms, but here it was selected by a pre-determined ANR. The temperature was logged before and after the monolith. The measurement equipment consisted of one Gasmet DX-4000 FTIR which measured the concentration of the NH_3, NO, NO_2, and N_2O. The data was logged at 1 Hz, which was the sampling time used for simulation. The commercial software Matlab was used for optimisation with an Intel Core i7-3630QM @ 2.4 GHz processor.

4.2.1 Experimental Data

This section will present the experimental data that was produced. Figure 4.2 shows inlet and outlet NH_3 concentration during the NH_3 only section at 200 ^{o}C. As can be seen, no NH_3 is consumed in oxidation reactions or other side reactions. At the

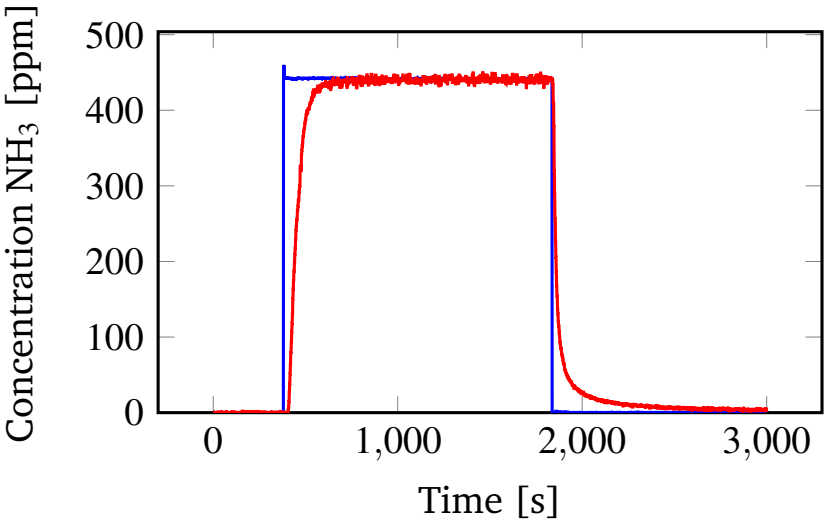

Figure 4.2. Experimental data used for calibration of adsorption and desorption reactions when only diluted NH_3 is used, at 200 ^{o}C. Legend: Input NH_3 (——), Output NH_3 (——)

beginning of the test, the catalyst had no stored NH_3, and the output is therefore delayed, since the NH_3 is being adsorbed on the surface. The difference in area between the inlet and outlet corresponds to the amount of adsorbed NH_3. This parameter was estimated with a Thermal Gravimetric Analysis (TGA) at 150^{o}C. In the end of the test, the NH_3 outlet is again delayed, due to the NH_3 being desorbed from the surface. It should be noted that the measurement equipment for NH_3 outlet was placed several meters away from the outlet of the monolith, and this can therefore exaggerate the tailing behaviour. NH_3 also has a tendency to stick to the surface of the transportation pipes, so that the tailing behaviour is increased further. No temperature rise was included after the NH_3 was turned off, which was included in for example [115]. This can compromise the quality of the adsorption and desorption parameters.

Figure 4.3 shows the inlet and outlet of NH_3 and NO during the NH_3 only test. The data covers the temperatures 200, 250, 300, 400, and 500^{o}C, with two different space velocities. Only one is showed here. The data points corresponds to the steady state values of experiments as the one in Figure 4.2. Up to 300 ^{o}C, the outlet of NH_3 is close to inlet, meaning that no oxidation takes place. At 400 and 500 ^{o}C, the outlet of NH_3 starts decreasing compared to the inlet, which is a result of the oxidation taking place at higher temperatures. It can be seen that NO is present in

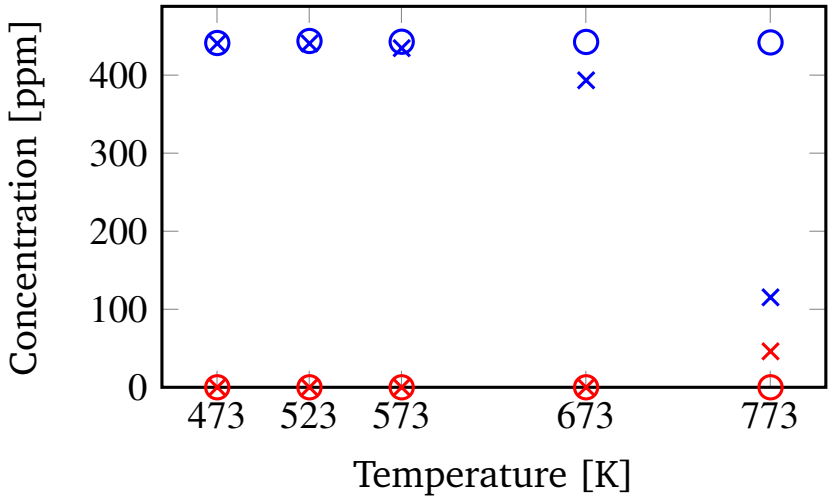

Figure 4.3. Experimental data used for calibration of SCR reactions and side reactions. NH_3 only. Legend: Input NH_3 (○), Output NH_3 (×), Input NO (○), Output NO (×)

the outlet as well, even though none was present in the inlet. This is believed to be due to NH_3 oxidation to NO. It is typical to model NH_3 oxidation as only producing N_2, which is not able to capture the oxidation to NO. This is the major reason that the kinetic model in Section 3.7 includes oxidation to NO. In an effort to keep the optimisation problem as simple as possible the oxidation reaction producing N_2 was not included. The idea is that at for example 400 ^{o}C, some of the produced NO will react with NH_3 in the standard SCR reaction. An oxidised NH_3 molecule therefore requires an extra NH_3 molecule, when it is reduced into N_2. Scenarios such as the one at 400 ^{o}C, where NH_3 is oxidised but no NO is present in the outlet, can thus be explained with the chosen kinetic model.

Figure 4.4 shows the inlet and outlet of NH_3 and NO with an approximate ANR of 1.0, meaning that an equimolar amount of the two is dosed. The ratio is upheld well for all temperatures besides 500 ^{o}C, where slightly more NH_3 is present than NO. It can be seen that the conversion of NO is increasing up to 300 ^{o}C. At 500, the NH_3 oxidation is significant, and the NH_3 is spent on producing NO instead of reducing NO. The produced NO results in that there is not enough NH_3 to remove all NO, and the conversion drops significantly.

Figure 4.5 shows the inlet and outlet of NH_3 and NO with an approximate ANR of 1.2, meaning that there is a 20 % molar surplus of NH_3. As in the case with ANR = 1.0, the ratio is approximately constant for all temperatures, except for 500

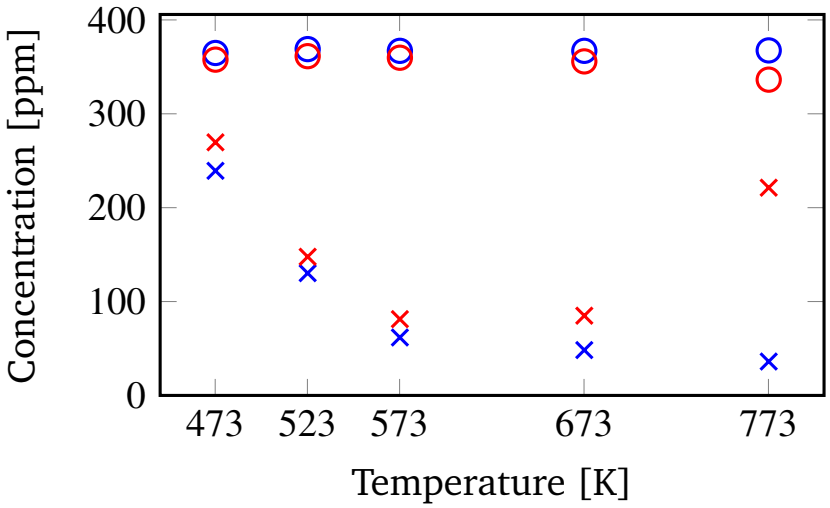

Figure 4.4. Experimental data used for calibration of SCR reactions and side reactions. ANR = 1. Legend: Input NH_3 (○), Output NH_3 (×), Input NO (○), Output NO (×)

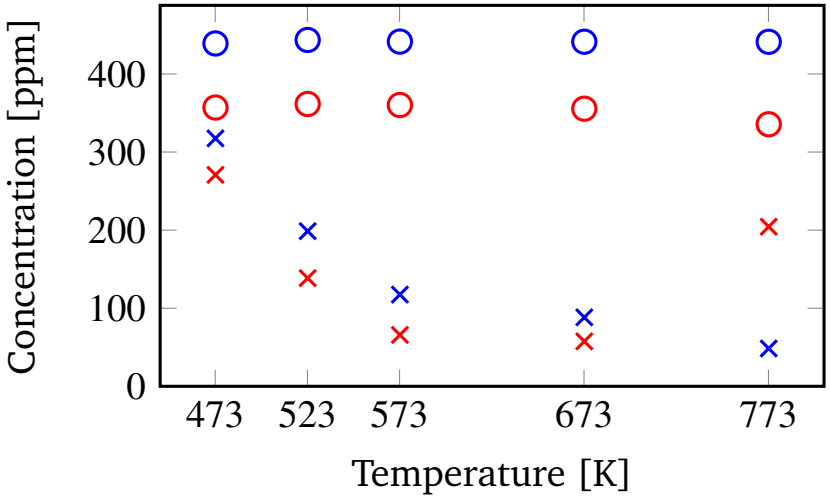

Figure 4.5. Experimental data used for calibration of SCR reactions and side reactions. ANR = 1.2. Legend: Input NH_3 (○), Output NH_3 (×), Input NO (○), Output NO (×)

^{o}C, where the ratio is slightly higher. The NO conversion is increasing up until 300 ^{o}C. At 500 ^{o}C, the NO conversion drops significantly due to NH_3 oxidation, as previously.

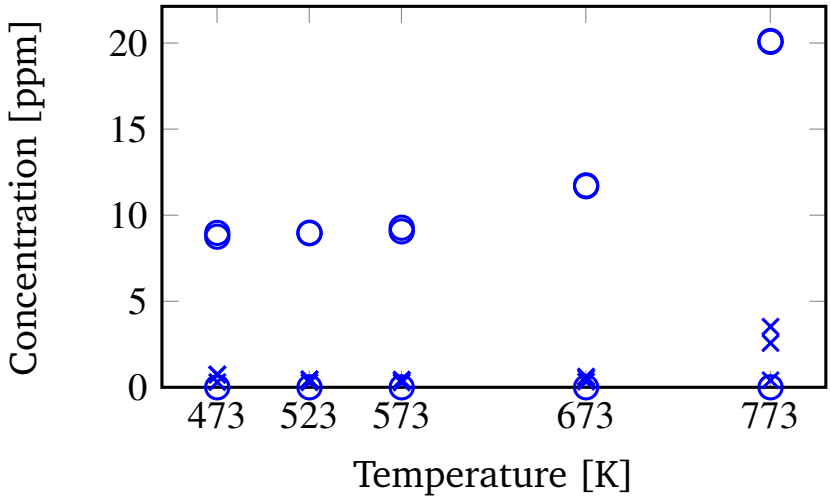

Figure 4.6. Experimental data used for calibration of SCR reactions and side reactions. Inlet and outlet of NO_2 for all three experimental sections, at each temperature. Legend: Input NO_2 (○), Output NO_2 (×)

Figure 4.6 shows the inlet and outlet of NO_2 for all three tested ANR, at 200, 250, 300, 400, and 500 ^{o}C. The inlet NO_2 concentration is increasing with temperature. Since the NO_2 concentration was not controlled, the present NO_2 is a result of the NO-NO_2 equilibrium reaction, and as such there is no NO_2 in the inlet when no NO was present in the inlet gases. The concentrations of NO_2 are ranging from around 2.5 % and 5 %, depending on temperature. The outlet concentrations are approximately 0 up to 400 ^{o}C, however at 500 ^{o}C, the concentration is between 3 and 5 ppm, depending on the ANR. The highest concentration is at ANR = 1, since NH_3 is in demand for the fast SCR reaction, which consumes NO_2. NO_2 can also be consumed in the N_2O formation reaction. Since this reaction is slower than the fast SCR reaction, it is expected that more of the NO_2 is converted to N_2O at ANR = 1.0 than ANR = 1.2. During only NH_3, it can be seen that there is no NO_2 in the inlet. Due to the low levels of NO_2, it is expected that calibration of the fast SCR reaction is quite difficult. The slow SCR reaction, that has not been included in this work, was left out because of this reason. The available NO_2 is much more likely to react in the fast SCR reaction because of the low levels.

Figure 4.7 shows the inlet and outlet of N_2O for all three tested ANR, at 200, 250, 300, 400 and 500 ^{o}C. The inlet of N_2O is 0 at all temperatures, since this was not included in the inlet gas mixture, and no reaction pathways are possible without a catalyst. The N_2O starts to appear in the outlet gas at 400 ^{o}C, however

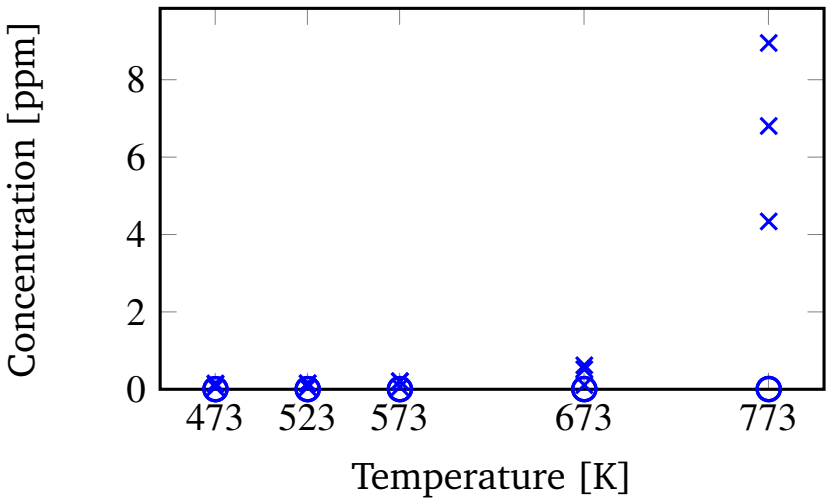

Figure 4.7. Experimental data used for calibration of SCR reactions and side reactions. Inlet and outlet of N_2O for all three experimental sections, at each temperature. Legend: Input N_2O (○), Output N_2O (×)

at very low levels, around 1 ppm. This can be due to measurement noise, but since the values are averages of a 100 second time span, it is likely that low levels of N_2O are present in the outlet gas. At 500 ^{o}C the N_2O concentration lies between 4 and 9 ppm, depending on the ANR. The point with the highest outlet N_2O concentration was with ANR = 1.0, which is expected due to the lower SCR activity. It is expected that a Vanadium based catalyst, as the one used, produces very low amounts of N_2O. However, since N_2O is formed from NO_2, and the levels of NO_2 were very low, it is possible that higher levels will be formed at driving conditions where NO_2 levels are higher. The lowest amount of N_2O correspond to when no NO is present in the inlet. At these conditions, the only way for N_2O to be produced, is if NH_3 is oxidised to NO, which is converted into NO_2 due to the equilibrium, which is then reacted into N_2O.

4.3 Methodology

This section will present the used methodology to estimate the kinetic parameters. The methodology is based both on bench-scale experimental data and full-scale experimental data. Since no Temperature Programmed Desorption (TPD) or oxygen free ammonia adsorption tests were available in this project, as explained in Section 4.2, the methodology does not depend on this data. This can lead to poor estimates

of the adsorption and desorption parameters, and the bench-scale data thus might have to be complemented with full-scale data. Two main steps are included; estimation of adsorption and desorption related parameters, and estimation of SCR and side-reactions related parameters. The methodology can be seen in Figure 4.8.

The first step is to define which parameters that needs to be estimated. The kinetic model in this work has 12 unknown kinetic parameters, 4 related to the adsorption and desorption parameters, and 8 related to the other reactions, as was shown in Chapter 3.

The second step is to define how the objective function should be formulated. The objective function determines what should be minimised during the optimisation. Depending on how its chosen, different parameter values will be achieved. The most common is to use a least squares version of the residuals. This has been adopted in this work:

$$J = \sum_{i=1}^{N} (y_i - f(u_i, \beta))^2 \tag{4.1}$$

where J is the objective to be minimised, y_i are the experimental measurements, and $f(u_i, \beta)$ are the function values calculated by the model using the inputs u_i and the parameter vector to be fitted, β. The objective is taken as the sum of the residuals over the entire time period that is simulated, where N is the number of time points. For estimation of adsorption and desorption parameters, NH_3 measurements were used in Equation (4.1). For the standard SCR, fast SCR, NH_3 oxidation, and N_2O formation, the measurements of NH_3, NO, NO_2, and N_2O were used.

Table 4.1. The procedure for estimating the kinetic parameters. The adsorption a desorption parameters were estimated together in one step, and the rest of the parameters in a second step.

Reaction	**Temperature range**(^{o}**C**)	**Data set**
Adsorption	200-300	Diluted NH_3
Desorption	200-300	Diluted NH_3
Normal+Fast SCR NH_3-Oxidation N_2O-formation	200-500	Diluted NH_3 SCR ANR 1.0 SCR ANR 1.2

Step three is to extract relevant data for the two estimation steps. Table 4.1 shows which data was selected for which parameters. Since no data was available with NH_3 adsorption that was not influenced by oxidation, only the data up to 300

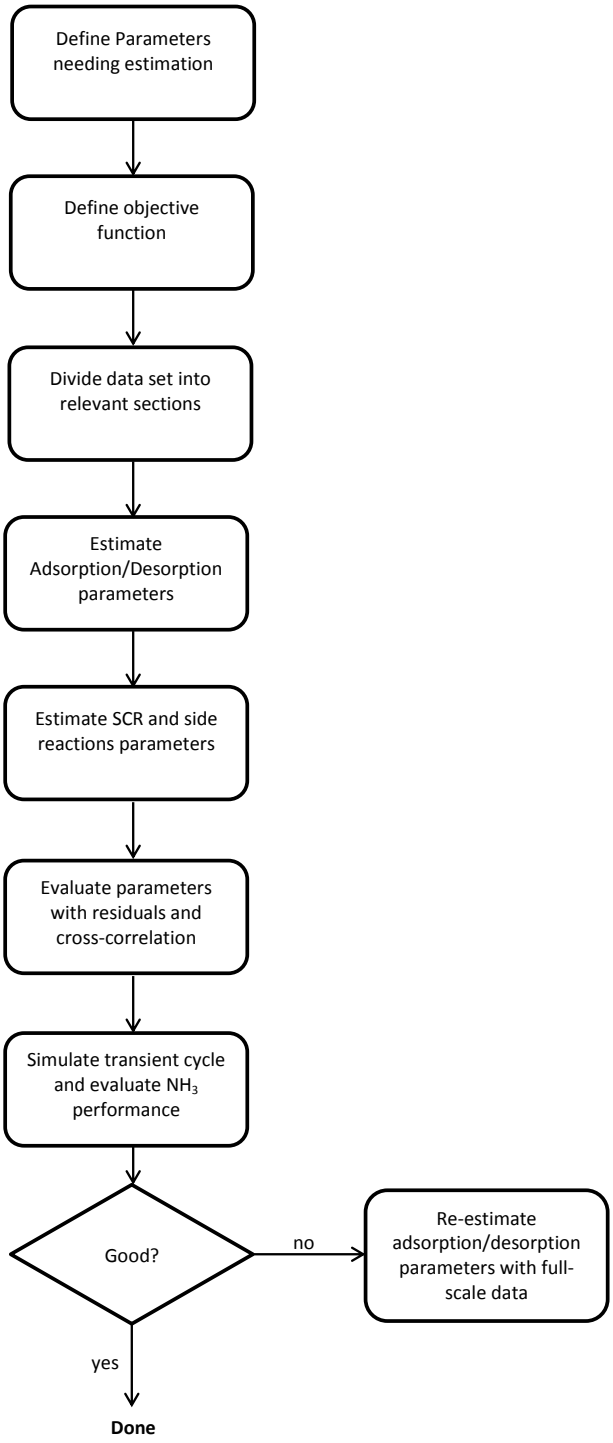

Figure 4.8. Sequential parameter estimation methodology to estimate the kinetic parameters. The adsorption and desorption parameter, and the SCR and side reactions, are estimated separately.

^{o}C was used for estimating these parameters. This was to make sure that the NH_3 oxidation did not influence the results. It should be noted that it was attempted to include all available data up to 500 ^{o}C, and at the same time have a NH_3 oxidation reaction directly to N_2. This did however not improve the result of the estimated parameters, and it was decided to only use data up to 300 ^{o}C.

Step four is to estimate the adsorption and desorption related parameters. The reason these are estimated separately from the SCR related parameters is to reduce the complexity of the optimisation problem. The adsorption and desorption estimation in this work also uses transient data. This is to include as much information as possible about the desorption reaction. The initial guess for the optimisation can for example be taken from literature, which was done in this work. The initial guess can heavily influence the time it takes for the optimiser to find a minimum. It is also possible that the problem is non-convex, meaning there are several local minima. The initial guess can determine which local minimum that is found.

After the adsorption and desorption parameters has been estimated, the SCR and side reaction parameters are estimated in step five. For this estimation, all of the available data presented in Section 4.2.1 was used. The estimation was based on the steady state values of each test, so no transient simulations were done. This saves considerable time, since its much faster to simulate a steady state scenario than a transient scenario. As previously stated, the objective function was now based on all measurements, including NH_3. This was to ensure that the NH_3 oxidation was calibrated correctly.

In step six the parameters are evaluated by analysing the residuals from the optimisation, the cross-correlation matrix, and the 95 % confidence intervals. Analysing the residuals is a easy and fast way to quickly get an overview on if the fit is satisfactory. The cross correlation matrix is defined as:

$$\mathbf{C}(i,j) = \frac{\mathbf{A}(i,j)}{\mathbf{A}(i,i)\mathbf{A}(j,j)} \tag{4.2}$$

where i and j are indices of the matrix, and $\mathbf{A}$ is:

$$\mathbf{A} = \sigma^2 \mathbf{H}^{-1} \tag{4.3}$$

where σ^2 is the variance, and $\mathbf{H}$ is the Hessian matrix. The cross-correlation matrix gives information about how strongly the parameters are correlated. A strong correlation between two parameters implies that a change in one parameter can be compensated by a change in the other, with very little effect on the objective function. The optimisation problem can therefore be said to be more difficult to solve,

and the solution might not be the best possible. In this application, it is expected to have two sorts of correlations. The first is correlation between the pre exponential factor and activation energy, in Equation (3.78). This can be reduced by centering the Arrhenius expression around a temperature, as done in this work. The second possible correlation is between reactions. For example, it is expected that Reactions (R4) and (R5) have correlated parameters, since both reactions consume NO_2. This correlation is difficult to remove, and the only way is to estimate the parameters separately, which would require special data sets for each reaction. Having separate data sets for each reaction is time consuming since a lot of resources has to be spent on producing experimental data. The confidence intervals reveal information about the likelihood that the parameters have the correct values. It should be noted, that the analysis methods can only reveal how good the fit is given the used data. If more data, or better data, is used for optimisation, the parameters and confidence intervals can be different.

Step 7 can in some way be considered a verification step, however the inclusion of this in this methodology is because of the possible poor performance for NH_3 adsorption and desorption. Not including a TPD and higher temperatures in the estimation data, can substantially affect the quality of the adsorption and desorption parameters. Therefore, a transient cycle, such as the European Transient Cycle (ETC), which has been used in this work, should be simulated to evaluate the predictive performance of the NH_3 slip. If the performance is satisfactory, the calibration procedure is done, and the model can be validated as explained in Chapter 5. If the performance is poor, the adsorption and desorption related parameters has to be recalibrated. In this project full-scale ETC data on a full-scale monolith was used. The experimental setup and data for the full-scale setup will be explained in detail in Chapter 5. During recalibration of the parameters, the objective function (4.1) was based on only NH_3 measurements.

4.4 Results

This section presents the parameter estimation results for the calibrated models. The majority of the analysis done will be presented for model 2. For the transient adsorption and desorption estimation, only the data for 200 ^{o}C will be presented. When showing the SCR reactions, NO and NO_2 will not be separated, but instead presented as total NOx. The NH_3 fit will also be presented for the SCR reactions.

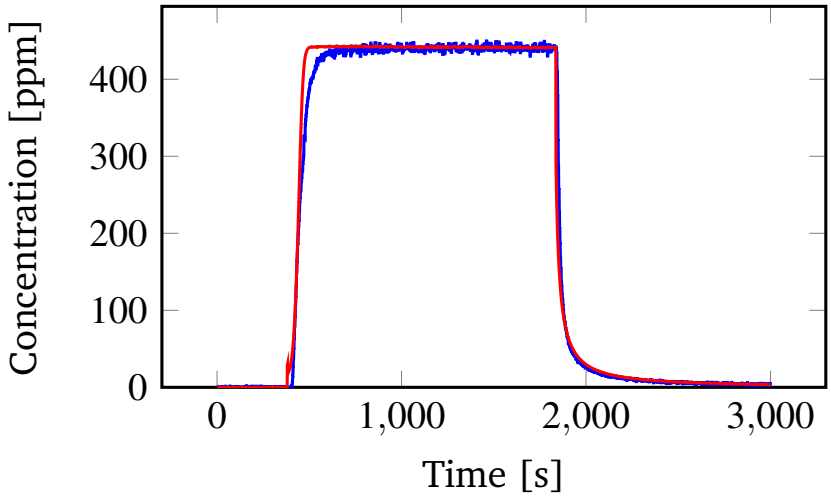

Figure 4.9. Model 2 fit to data after calibration for adsorption and desorption reactions, at 200 ^{o}C. Legend: Experimental data (——), Model (——)

4.4.1 Model 2

This section will present the results from the parameter estimation of model 2. Model 2 was calibrated first, and the results were the basis for calibration of the other models.

The estimated parameter values for the first calibration with model 2 coupled to the kinetic model, along with their 95- % confidence intervals, are given in Table 4.2. The parameters for the adsorption and desorption reactions have narrow confidence intervals. The value for the adsorption parameter is high, but the other parameters are reasonable, compared to literature [135, 139, 86]. The activation energy for the NH_3 oxidation is high. The value is however expected to be higher than values in literature because of the assumption that NH_3 is oxidized into NO. For every molecule that is oxidized, another molecule is needed to reduce NO into N_2. The parameter values for the SCR reactions have reasonable values compared to literature. Based on the values of the parameters and their narrow confidence intervals, the fit was evaluated as satisfactory.

The cross correlation matrix for the kinetic parameters related to the standard and fast SCR, NH_3-oxidation and N_2O reactions can be found in Table 4.4.1. The matrix shows that for the majority of the cases, the correlation is low between the parameters. The centering of the Arrhenius expressions was successful in removing the correlation between the pre exponential factor and the activation energy for

Table 4.2. Parameter values for kinetic model coupled with Model 2.

Parameter	Value	95-% CI
$k_{0,ads}[1/s]$	1500	$\pm 4\%$
$k_{0,des}[1/s]$	$2.9 \cdot 10^{11}$	$\pm 15\%$
$E_{0,des}$ [kJ/mol]	120.5	$\pm 3\%$
$\alpha[-]$	0.22	$\pm 7\%$
$k_{0,oxidation}$ [mol/m^3/s]	$9.56 \cdot 10^{17}$	$\pm 24\%$
$E_{oxidation}$ [kJ/mol]	234.1	$\pm 1\%$
$k_{0,standard}[1/s]$	$5.61 \cdot 10^{10}$	$\pm 8\%$
$E_{standard}$ [kJ/mol]	90.0	$\pm 3\%$
$k_{0,fast}$ [m^3/mol/s]	$1.03 \cdot 10^{13}$	$\pm 17\%$
E_{fast} [kJ/mol]	74.5	$\pm 3\%$
$k_{0,N_2O}[1/s]$	$4.41 \cdot 10^{16}$	$\pm 4\%$
E_{N_2O} [kJ/mol]	170.5	$\pm 3\%$

Table 4.3. Correlation matrix for the SCR and side reactions when using Model 2

$k_{0,standard}$	$E_{standard}$	$k_{0,\text{fast}}$	E_{fast}	$k_{0,\text{oxidation}}$	$E_{\text{oxidation}}$	k_{0,N_2O}	E_{N_2O}	
1	0.06	−0.23	0.04	0.02	−0.46	−0.25	−0.34	$k_{0,standard}$
	1	−0.31	0.38	0.62	0.29	−0.38	0.06	$E_{standard}$
		1	−0.22	0.13	0.33	0.26	0.01	$k_{0,\text{fast}}$
			1	−0.03	−0.16	−0.98	0.15	E_{fast}
				1	0.81	0.02	0.60	$k_{0,\text{oxidation}}$
					1	0.25	0.75	$E_{\text{oxidation}}$
						1	−0.07	k_{0,N_2O}
							1	E_{N_2O}

the different reactions. The majority of the remaining correlation is due to the simultaneous estimation of many parameters. The correlation between k_{0,N_2O} and E_{fast} has a high value of 0.98. To remove this correlation the different reactions would have to be calibrated separately, requiring more detailed experimental data.

Figure 4.9 shows the data points and model fit for NH_3 during the adsorption and desorption calibration using only NH_3 data. As seen, the model follows the data well, and the residuals are small. Figure 4.10 shows the data points and model fit for NH_3 during the SCR related parameter estimation, and Figure 4.11 shows the same for NO. The three different points at each temperature shows two different ANR and one with only diluted NH_3. The residuals for both NH_3 and NO are small. This, along with the tight confidence intervals and low correlations suggests a good fit for the calibration.

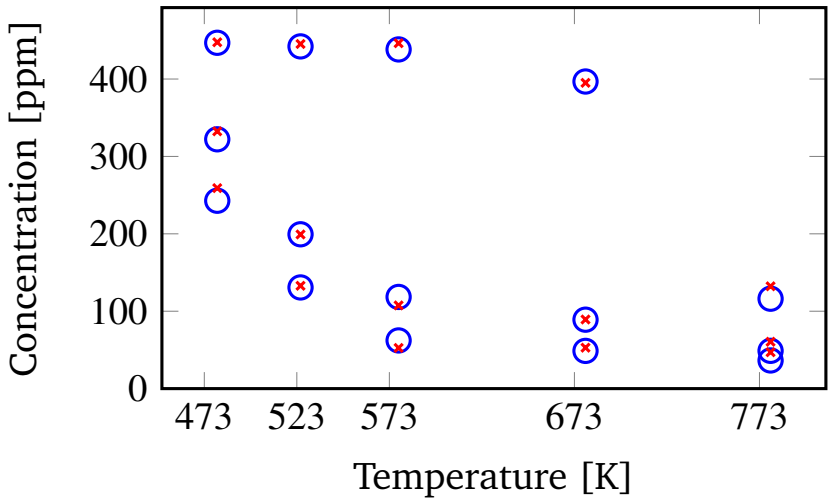

Figure 4.10. Model 2 fit to NH_3 data after calibration for SCR calibration, at all tested ANR, for all temperatures. Legend: Experimental data (○), Model (×)

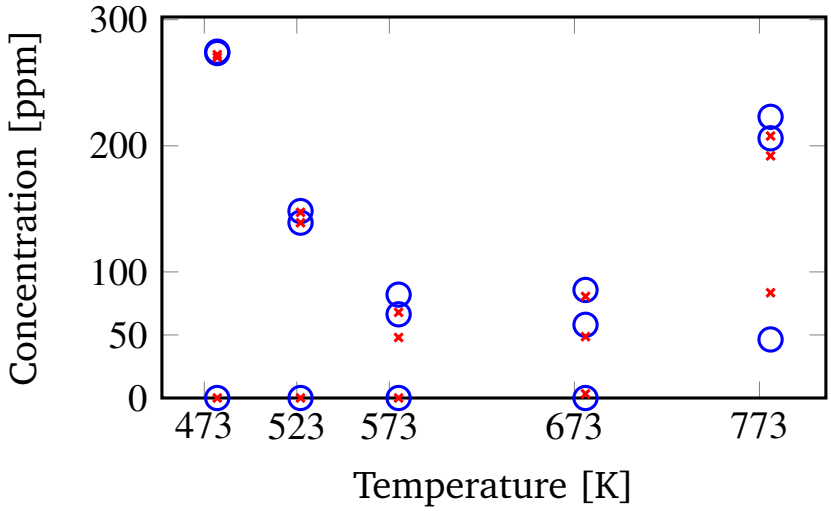

Figure 4.11. Model 2 fit to NO data after calibration for SCR calibration, at all tested ANR, for all temperatures. Legend: Experimental data (○), Model (×)

Table 4.4. New parameter values for adsorption and desorption after full-scale recalibration, for Model 2.

Parameter	Value	95-% CI
$k_{0,ads}$ [1/s]	513	±6.1%
$k_{0,des}$ [1/s]	$1.2 \cdot 10^{11}$	±116%
$E_{0,des}$ [kJ/mol]	119	±5.6%
α [-]	0.44	±5.7%

When the parameters were tested against full scale data, it was however seen that the NH_3 prediction performed unsatisfactory. Neither the dynamics nor the levels were in agreement with data. This was most likely due to inadequate data for estimating the adsorption and desorption parameters. Another possible explanation is that the injected urea was not fully hydrolysed at the inlet of the catalyst. This effect would not be seen in the small scale experiments, since NH_3 was injected directly, thus eliminating the effects from urea decomposition. To test this theory two reaction steps were included that described the decomposition and hydrolisation of urea into NH_3. The parameters were calibrated with a full-scale ETC data set. This analysis showed that the problem with poor NH_3 prediction was not solved, suggesting that a more rigorous analysis is needed to include this effect. Instead, the adsorption and desorption parameters were recalibrated using the full-scale data set, while keeping all other parameters fixed. The objective function in Equation (4.1) was only based on NH_3 measurements, in order to remove the influence of NO. After the recalibration the results for the NOx prediction were similar to before the recalibration, while the NH_3 prediction was greatly improved. These results will be shown in Chapter 5, in relation to model validation. The new adsorption and desorption related parameters can be seen in Table 4.4.

4.4.2 Model 1

The parameter estimation of model 1 was carried out after the calibration of model 2, and the initial guess for the adsorption and desorption reactions were based on the parameters for model 2. The parameters for model 1 can be seen in Table 4.5. The adsorption coefficient takes a similar value as the one for model 2, even before the adsorption and desorption coefficients are recalibrated will full-scale data. The desorption energy however, has a very low value. The SCR related reactions both have expected values, with the activation energy for the fast SCR being lower than for the standard SCR. The parameters for the N_2O formation reaction are not re-

Table 4.5. Parameter values for kinetic model coupled with Model 1.

Parameter	Value	95-% CI
$k_{0,ads}[1/s]$	467	$\pm 2\%$
$k_{0,des}[1/s]$	$7.9 \cdot 10^5$	$\pm 23\%$
$E_{0,des}$ [kJ/mol]	60.4	$\pm 2\%$
$\alpha[-]$	0.17	$\pm 3\%$
$k_{0,oxidation}$ [mol/m^3/s]	$1.06 \cdot 10^{18}$	$\pm 2\%$
$E_{oxidation}$ [kJ/mol]	235.2	$\pm 0.5\%$
$k_{0,standard}[1/s]$	$7.82 \cdot 10^{10}$	$\pm 0.1\%$
$E_{standard}$ [kJ/mol]	91.1	$\pm 1.7\%$
$k_{0,fast}$ [m^3/mol/s]	$6.17 \cdot 10^{12}$	$\pm 1.2\%$
E_{fast} [kJ/mol]	68.5	$\pm 0.1\%$
$k_{0,N_2O}[1/s]$	$3.09 \cdot 10^{55}$	$\pm 9.2\%$
E_{N_2O} [kJ/mol]	644	$\pm 9\%$

alistic, and the optimisation has taken values that give no production of N_2O. This is explained by the fact that the N_2O levels are very low in the calibration data, and the lowest residual is apparently to produce no N_2O. As discussed in Chapter 3, depending on the mass transfer limitations in the monolith, it is expected to have the efficiency factor η removed from the kinetic parameters in this model, compared to model 2. As can be seen for the SCR related parameters, they have very similar values compared to model 2. Figure 4.12 shows the fit to data for the transient NH_3 data at 200 ^{o}C that was used to estimate the adsorption and desorption parameters. In the initial increase in NH_3 concentration, the model predicts a sharper "turn-in" to steady-state. This appears to be common also in literature, see for example [79, 89]. The fit to data is good throughout the test, and the fit is evaluated as satisfactory. Figures 4.13 and 4.14 shows the fit to data for NH_3 and NOx when model 1 is being used, during SCR reaction calibration. The residuals for NH_3 are generally very low, on the order of <10 ppm. The fit is satisfactory for both low and high temperatures. For NOx, the fit is slightly better at low temperatures than high temperatures, especially for the case when no inlet is present in the inlet. This suggests that the NH_3 oxidation is too strong at high temperatures. Another explanation is that to get a good fit at high temperatures, NH_3 oxidation to N_2 is required.

The increased complexity of model 1 compared to model 2, increases simulation time dramatically, to the point where it is not feasible to simulate transient tests such as the ETC. Since the residuals are on the same level as model 2, and the parameters have very similar values, it was decided to not use model 1 further.

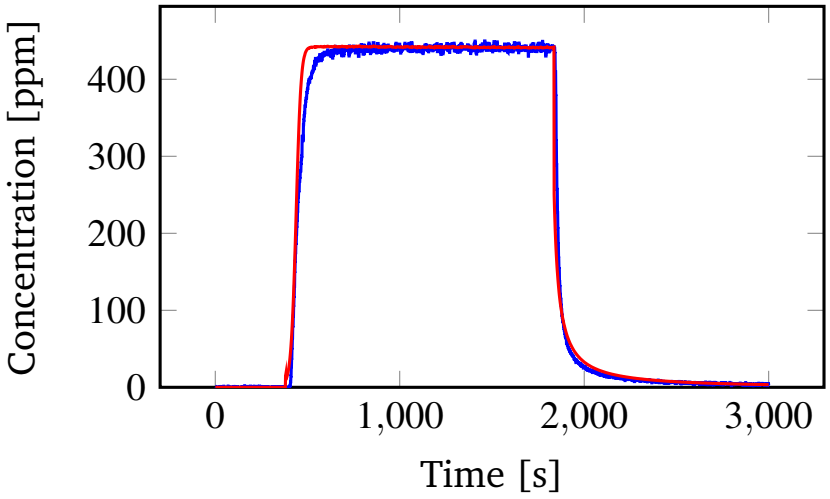

Figure 4.12. Model 1 fit to data after calibration for adsorption and desorption reactions, at 200 ^{o}C. Legend: Experimental data (——), Model (——)

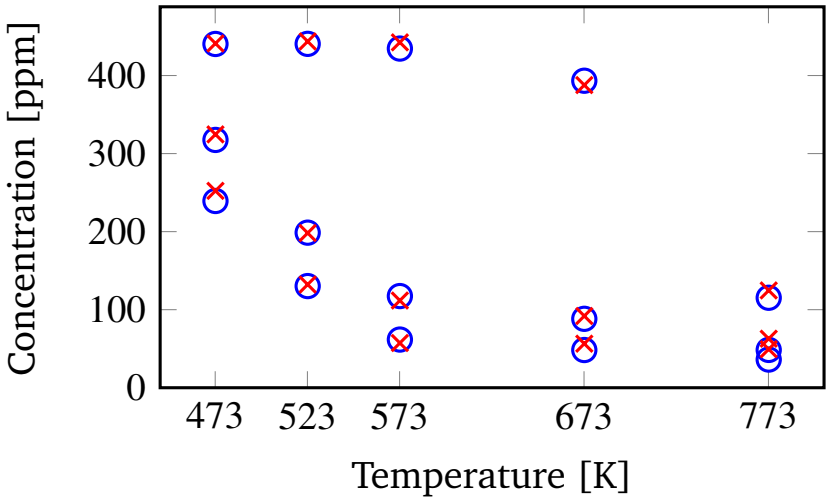

Figure 4.13. Model 1 fit to NH_3 data after calibration for SCR calibration, at all tested ANR, for all temperatures. Legend: Experimental data (○), Model (×)

The analysis carried out in Chapter 3, and the results presented here, shows that internal mass transfer is not necessarily a limiting factor, and there is no advantage in using model 1. The adsorption and desorption parameters will therefore not be recalibrated with full-scale data together with model 1.

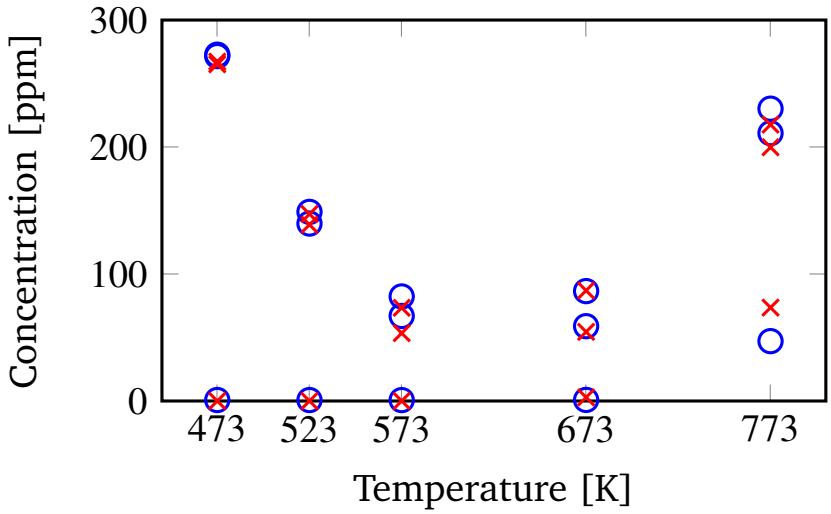

Figure 4.14. Model 1 fit to NO data after calibration for SCR calibration, at all tested ANR, for all temperatures. Legend: Experimental data (○), Model (×)

4.4.3 Model 3

Based on the performance of model 3, shown in Chapter 6, model 3 was chosen to be calibrated. The parameter values for Model 3 after estimation can be found in Tab. 4.6. The parameter values are different from what was shown in Table 4.2. The value for the adsorption parameter is very different from the initial calibration of model 2. It should be noted that the initial guesses used during optimization were the ones that are given in Table 4.2. It is possible that the optimization is non-convex and there are several local minima for the objective function. It is therefore uncertain if a global minimum was found. The activation energies are no longer realistic from a physic-chemical point of view. The reason for this is unknown, however the values result in the best fit to data. It can be noted that there is a substantial difference in the confidence interval in the parameters when comparing to model 2. For example, the confidence interval for the activation energy for the fast SCR reaction is 45 % for model 3. A reason for this has not been found, since the calibration is done under isothermal conditions. It can be noted that some of the parameters have insignificant parameters, meaning that the confidence interval includes 0. The parameters with insignificant values has still been used in simulations. For model 3 the parameters for the N_2O formation reaction are highly uncertain, compared to the ones for model 2. N_2O are present in very low concentrations compared to the other species, and removal of information about

Table 4.6. Parameter values for kinetic models coupled with Model 3. The units are the same as in Tab. 4.5

Parameter	Value Model 3	95-% CI
$k_{0,ads}$	467	±1.8%
$k_{0,des}$	$7.9 \cdot 10^5$	±23%
$E_{0,des}$	60.4	±1.9%
α	0.17	±2.9%
$k_{0,oxidation}$	$3.27 \cdot 10^{16}$	±13%
$E_{oxidation}$	221.1	±10%
$k_{0,standard}$	$1.83 \cdot 10^9$	±1%
$E_{standard}$	75.3	±5%
$k_{0,fast}$	$3.14 \cdot 10^{12}$	±11%
E_{fast}	73.6	±45%
k_{0,N_2O}	$2.2 \cdot 10^{14}$	±200%
E_{N_2O}	140.0	±100%

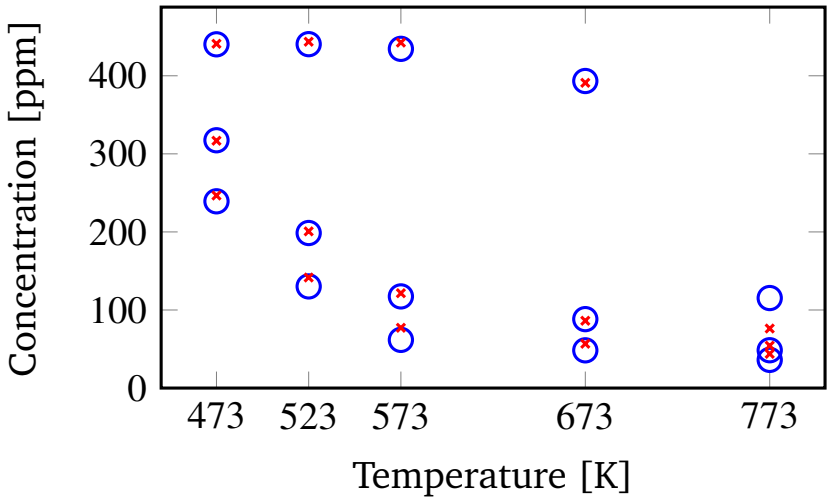

Figure 4.15. Model 3 fit to NH_3 data after calibration for SCR calibration, at all tested ANR, for all temperatures. Legend: Experimental data (○), Model (×)

the wash coat seems to impact the effect of this greatly.

Figures 4.15 and 4.16 shows the residuals for NH_3 and NO, respectively, during calibration of model 3. As expected due to simplifications, the residuals are generally larger than those found in Figures 4.10 and 4.11. The largest difference can be found at high temperatures, where NH_3 oxidation becomes significant.

Model 3, just as model 2, had after the calibration problems predicting the NH_3

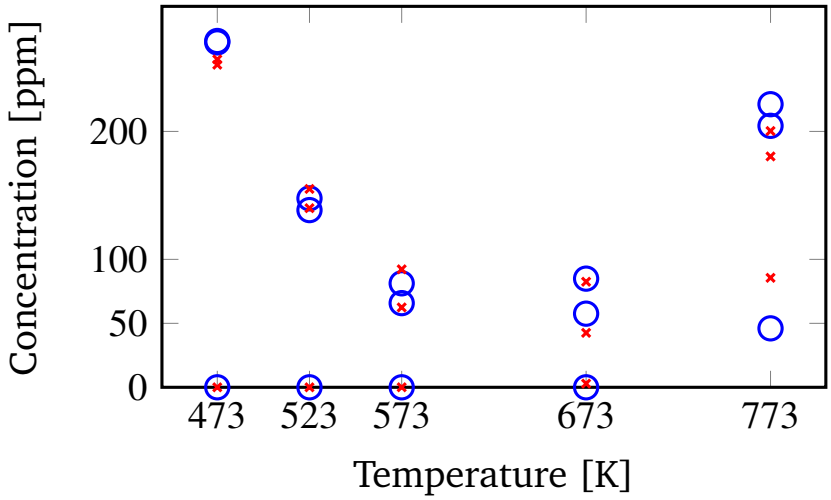

Figure 4.16. Model 3 fit to NO data after calibration for SCR calibration, at all tested ANR, for all temperatures. Legend: Experimental data (○), Model (×)

slip in full-scale simulations. Based on this, and on results shown in Chapter 6, the adsorption and desorption related parameters were recalibrated using full-scale ETC data. The new parameters can be found in Table 4.7. The parameters related to NH_3 adsorption and desorption for Model 3 after recalibration with full-scale data can be compared to the original values in Table 4.6. The adsorption coefficient, $k_{0,ads}$ has decreased, as was the case when model 2 was recalibrated as well. One possible reason for this is that the adsorption of NH_3 to the catalyst is over estimated when isothermal reactor data is used without a TPD. Another reason can be the that the sensor response is delayed. A decrease in $k_{0,ads}$ leads to more NH_3 in the outlet, which can only be seen in the full-scale transient data, and not the outlet of the bench-scale reactor data, where the outlet concentration of NH_3 is the same as the inlet concentration when the catalyst surface is full of adsorbed NH_3. If the parameters between model 2 and model 3 are compared, model 2 has a higher adsorption coefficient, and a lower activation energy for the desorption than model 3. The reason for a lower adsorption coefficient can be that the reaction concentration is slightly higher than with model 2. Since there is no distinction between the wash coat concentration and bulk concentration in model 3, the reactions are not limited by the mass transfer to the wash coat. A slightly lower adsorption coefficient corrects for this. The coverage dependency is however also higher for model 2 which gives higher desorption rate at high temperatures. The difference in activation energy for the desorption reaction between models 2 and 3 is however small,

Table 4.7. New parameter values for adsorption and desorption after full-scale recalibration, for Model 3.

Parameter	Value	95-% CI
$k_{0,ads}$ [1/s]	407	$\pm$4%
$k_{0,des}$ [1/s]	$1.2 \cdot 10^{11}$	$\pm$50%
$E_{0,des}$ [kJ/mol]	122.2	$\pm$4%
α [-]	0.39	$\pm$21.3%

suggesting that the recalibration with full-scale data allows for a more accurate estimate.

4.4.4 Model 5

The parameter values for the calibrated model 5 after estimation can be found in Table 4.8. As with model 3, the parameter values are different from what was shown in Table 4.2. The value for the adsorption parameter is similar to what was achieved for model 3, however differs from the value of model 2. For the desorption it can be noted that the values for model 3 and 5 are similar. The activation energy is substantially lower than for model 2, and no longer has a realistic value from a physic-chemical point of view. The confidence intervals for model 5 are wide, making some of the parameters insignificant. For example, the confidence interval for the activation energy for the fast SCR reaction is 600 %. A reason for this has not been found, since the calibration is done under isothermal conditions. If the temperature was transient a possible reason is that the non smoothed temperature of model 5 would lead to difficulties in estimating temperature dependence. A 600 % deviation makes the parameter statistically insignificant. The parameters with insignificant values has still been used in the calculations.

Figures 4.17 and 4.18 shows the fit to data for NH_3 and NOx, respectively, during SCR reaction calibration with model 5. As can be seen, the residuals are low for both NH_3 and NOx, indicating a good fit. The residuals are slightly higher at 500 ^{o}C, compared to the lower temperatures, especially for the case when no NO is present in the inlet.

Due to NH_3 performance, the adsorption and desorption parameters were recalibrated using full-scale data. The parameters can be seen in Table 4.9. As seen, the parameter values are after recalibration relatively close to the values of model 2. The activation energy for the desorption reaction is slightly higher than for model 2.

Table 4.8. Parameter values for kinetic model coupled with model 5. The units are the same as in Tab. 4.2.

Parameter	Value Model 5	95-% CI
$k_{0,ads}$	459	$\pm$1.9%
$k_{0,des}$	$7.7 \cdot 10^6$	$\pm$27%
$E_{0,des}$	71.8	$\pm$1.9%
α	0.18	$\pm$2.3%
$k_{0,oxidation}$	$7.28 \cdot 10^{16}$	$\pm$12%
$E_{oxidation}$	224	$\pm$9%
$k_{0,standard}$	$4.56 \cdot 10^9$	$\pm$1%
$E_{standard}$	79.3	$\pm$3%
$k_{0,fast}$	$2.79 \cdot 10^9$	$\pm$66%
E_{fast}	31.7	$\pm$600%
k_{0,N_2O}	$1.13 \cdot 10^{15}$	$\pm$570%
E_{N_2O}	152	$\pm$180%

Table 4.9. New parameter values for adsorption and desorption after full-scale recalibration, for Model 5.

Parameter	Value	95-% CI
$k_{0,ads}$ [1/s]	1100	
$k_{0,des}$ [1/s]	$3.8 \cdot 10^{11}$	
$E_{0,des}$ [kJ/mol]	125.1	
α [-]	0.13	

Notably, the adsorption coefficient is substantially higher. This is most likely due to the fact that the removal of thermal mass leads to a rapidly changing temperature in the channel. The combination of a lower desorption and a higher adsorption, ensures that the rapid changes in temperature does not lead to all the NH_3 being desorbed directly. In the original calibration of the adsorption and desorption parameter, the effect of this cannot be seen due to the steady-state temperature. The fact that the temperature will behave transiently inside the channel is only captured with transient data.

4.5 Discussion

It can be noted that after the initial adsorption and desorption reaction calibration, the parameters of model 2 differs quite substantially from the parameters of the other models. The reason for this is believed to be the initial guess, and since model

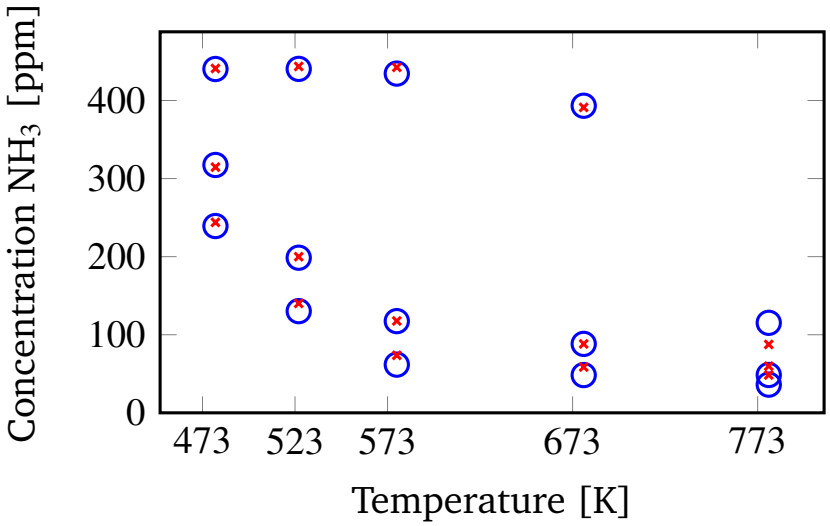

Figure 4.17. Model 5 fit to NH_3 data after calibration for SCR calibration, at all tested ANR, for all temperatures. Legend: Experimental data (○), Model (×)

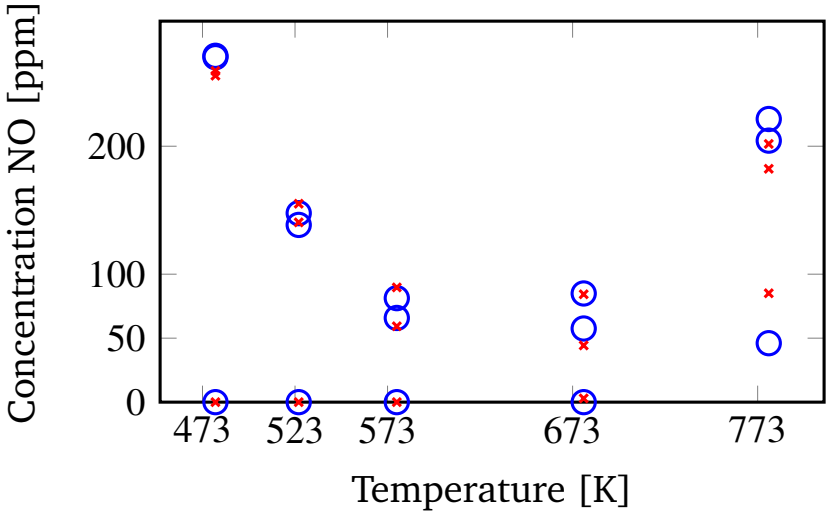

Figure 4.18. Model 5 fit to NO data after calibration for SCR calibration, at all tested ANR, for all temperatures. Legend: Experimental data (○), Model (×)

Table 4.10. Parameters for adsorption and desorption for model 2. The initial guess was the parameters from model 1, to test the influence of the initial guess.

Parameter	Value	95-% CI
$k_{0,ads}$ [1/s]	539	±6.0%
$k_{0,des}$ [1/s]	$3.56 \cdot 10^7$	±33.3%
$E_{0,des}$ [kJ/mol]	73.5	±2.6%
α [-]	0.21	±13.8%

2 was calibrated first, during this calibration parameter values from literature was used as initial guess. For the other models, the initial guesses were based on the parameters achieved with model 2. It can also be seen that after the recalibration of the adsorption and desorption parameters with full-scale data for model 2 and 3, the parameters have similar values. When the SCR related parameters and NH_3 oxidation are compared it can be seen that for all models they have similar values. The solution of the optimisation problem depends both on the objective function to be minimised, and the data the model is trying to fit. The objective function can be non-convex and have several local minima that can be found depending on the initial guess. To test this theory, the adsorption and desorption parameters were calibrated with the parameters from model 1 as initial guess. The result can be seen in Table 4.10. As seen, the parameters have now taken very similar values to what was achieved with the other models when using the small-scale reactor data.

When the optimisation results are examined in detail it can also be seen that the objective function values are very similar for the solution shown in Table 4.2 and 4.10, making the optimisation problem difficult. It is therefore clear that with the adsorption and desorption data that was used, several local minima exists. However with the full-scale data that was used to recalibrate the parameters, it can be seen that the parameters take very similar values, and are realistic from a physic-chemistry point of view. It can therefore be concluded that the estimation data is crucial in getting good parameter values. It can also be concluded that the data for estimating the adsorption and desorption parameters is not optimal.

It can be seen that for the presented models, the NOx fit is generally better at low temperatures than at high temperatures. Even though the residuals are generally small, they are slightly higher at high temperatures. For the case with only diluted NH_3, the model predicts too much NOx, and for ANR = 1, 1.2, the model predicts slightly too little NOx. This can be traced down to how the NH_3 oxidation

is treated. Since a Vanadium based catalyst is modelled, it was assumed that NH_3 is oxidised only to NO, and not N_2. This is generally a good approximation for Vanadium based catalyst, whereas for a Fe-based zeolite, the NH_3 oxidation to N_2 is very prominent. From the data it can however be concluded that some NH_3 oxidation to N_2 do occur. If there was any NH_3 oxidation to N_2, it was believed that this could be corrected for by letting the produced NO molecule react in the SCR reactions. At high temperatures, it appears that to fully explain the outlet, an extra reaction would be needed.

In this work it was decided to do the parameter estimation by formulating a optimisation problem and solving it. When steady-state data at different temperatures is available, it is also possible to use the Arrhenius plot to get the parameters. If the logarithm of the Arrhenius expression and the reaction speed is taken at temperature T, the following is the result:

$$\log(r_0) = \log(k) + \frac{E}{RT} \tag{4.4}$$

where r_0 is the reaction speed at temperature T, k is the pre exponential factor, and E is the activation energy. If r_0 is plotted against the inverse temperature, the slope will thus be $\frac{E}{R}$ and the intercept $\log(r_0)$. In the early stages of the project, this was tried for the SCR reactions. Figures 4.19 and 4.20 shows the Arrhenius plot for the standard SCR reaction and the fast SCR reaction. If the slopes and intercepts are extracted the parameter for the reactions are as in Table 4.11. The parameters are different from what was achieved with the optimisation method. Notably, the activation energy for the standard SCR reaction was very high with this method. The parameters were not tested on full-scale or steady state data to see the performance, but with a very high activation energy on the standard SCR, the most active SCR reaction disappears at lower temperatures, and it is difficult to imagine that the performance would have been satisfactory. It was therefore decided not to use this method, and instead use the optimisation based method, that produced realistic values for the SCR reactions.

The observations presented in this chapter does not justify the use of model 1 compared to model 2. The kinetic parameters obtained with model 1 had very similar values to the ones with model 2. Model 1 and 2 are expected to perform at the same level of accuracy, but with different kinetic parameters to account for the internal mass transfer. If internal mass transfer limitations were present, the kinetic parameters of model 2 would have indicated a lower reaction rate compared

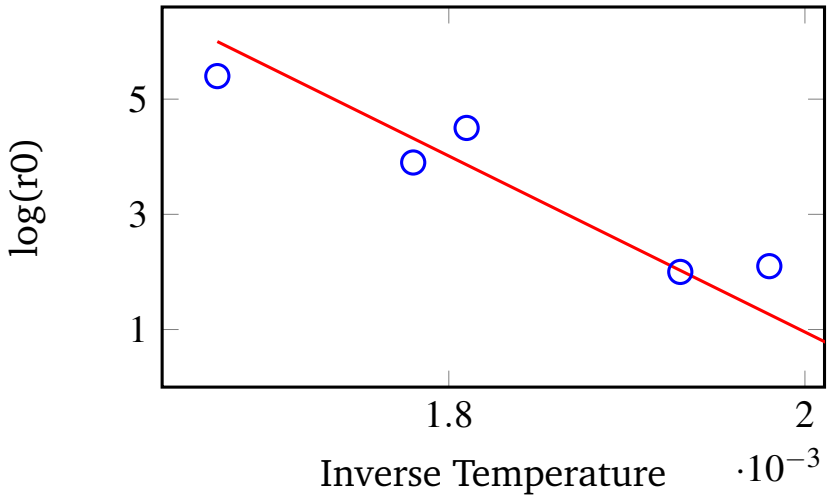

Figure 4.19. Test of using the Arrhenius plot for parameter estimation for the standard SCR reaction. Legend: Experimental data (○), Linear fit to data (——)

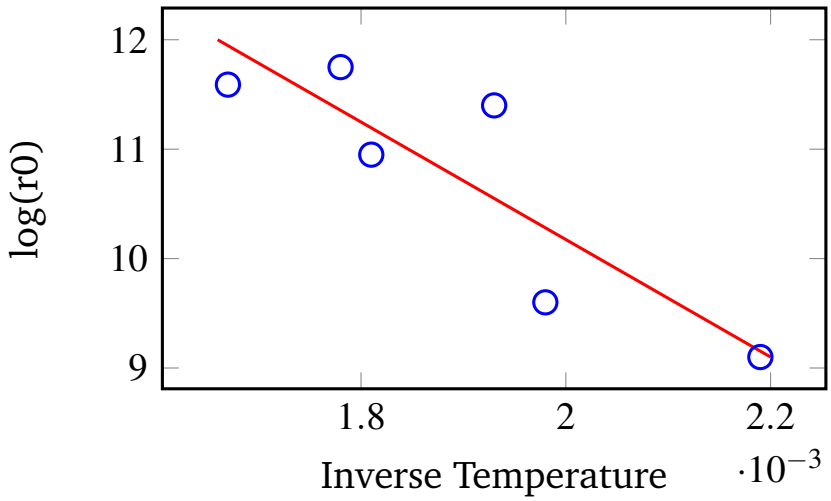

Figure 4.20. Test of using the Arrhenius plot for parameter estimation for the fast SCR reaction. Legend: Experimental data (○), Linear fit to data (——)

Table 4.11. Parameters for the standard and fast SCR reactions, when the Arrhenius plot is used.

Parameter	Value
$k_{standard}$ [1/s]	$6.93 \cdot 10^{13}$
$E_{standard}$ [kJ/mol]	129
k_{fast} [1/s]	$1.27 \cdot 10^{9}$
E_{fast} [kJ/mol]	45.0

to the parameter of model 1. Model 1 includes parameters that introduces extra uncertainties in the model, for example the wash coat diffusion. If a good value for this parameter is not available, the extra complexity will introduce additional simulation time, without additional information. Because of this, it was decided to not continue working with model 1, and model 2 is the most complex model used.

4.6 Conclusions

A methodology to estimate kinetic parameters using bench-scale reactor data and full-scale transient data has been presented. The methodology does not depend on TPD tests, which can compromise the quality of the adsorption and desorption parameters. The methodology has been applied, both completely, and partly, to the presented models in Chapter 3. The models were able to capture the steady-state behaviour of the small-scale SCR monolith well.

Chapter 5

Validation of the SCR Monolith Models

The validation of the previously calibrated SCR monolith models is presented. The validation is based on simulating a full-scale SCR monolith treating real engine gases from an engine following the European Transient Cycle (ETC). The experimental setup is presented, and the methodology to validate the models. The validation is carried out for model 2, model 3, and model 5, using the parameter presented in Chapter 4. The results shows that the models capture the NOx behaviour well, however the NH_3 prediction is less satisfactory.

The main contribution of this chapter is published in two articles (A. Åberg, A. Widd, J. Abildskov, J. K. Huusom. Parameter Estimation and Analysis of an Automotive Heavy-duty SCR Catalyst Model. Chemical Engineering Science 161 (2017) 167-177), and (A. Åberg, A. Widd, J. Abildskov, J. K. Huusom. Estimation of Kinetic Parameters in an Automotive SCR Catalyst Model, Topics in Catalysis 59 (2016) 945-952).

5.1 Introduction

This chapter will present the validation of the models that were calibrated fully in Chapter 4. Models 2, 3, and 5, were calibrated using the full methodology, and will therefore be presented here. Model 4, has due to reasons presented both in Chapter 4 and Chapter 6, not been calibrated and will therefore not be validated. Models 2, 3, and 5 will be validated by simulating a full-scale engine test, and comparing to experimental data. The test is based on a full-scale engine running the European Transient Cycle (ETC), which is a transient test. The reason for using a transient test to validate the models is because it will ensure that the models can correctly predict the SCR monolith behaviour for a very broad range of operating conditions. The ETC is designed to be a realistic representation of how a heavy-duty truck can operate on the road. If a model can accurately predict the behaviour throughout this test, the model can be used for testing control algorithms, which will be the topic of Chapter 7. As seen in Chapter 4, the models were calibrated using mostly steady state data, and this chapter will clearly show if it is possible to use steady steady state data to calibrate a model that is intended to be used for a transient application. Since several models with different simplifications will be validated, it will be possible to see how different simplifications affect the performance of the model. This chapter will not go into detail on how the simplifications perform. That will instead be the focus of chapter 6.

5.2 Experimental Setup

The experimental data used for validation were produced using a full-scale engine, without Exhaust Gas Recirculation (EGR), and with a displacement of 10 liters. The used monolith was a full body vanadium based catalyst with 270 CPSI on a corrugated substrate, and 9 inches long and 12.7 inches in diameter. The monolith and catalyst had the exact same properties as the one used for parameter estimation, in Chapter 4, meaning it was simply a bigger version of it. The European Transient Cycle (ETC) [32] was used as a pre-set for the engine. The exhaust gases were not pre-treated with other catalysts before entering the SCR. The setup was placed in a room without climate control, meaning that different tests can have slightly different results, due to different ambient conditions. The measurement equipment consisted of two Horiba MEXA 7000, one Siemens LDS 6 Diode, and one Gasmet DX-4000 FTIR. The MEXA systems measured the NO, NOx, CO, CO_2, O_2, HC, and N_2O. The FTIR measured the NH_3 ex-situ and the LDS measured the NH_3 in-situ.

The temperature was measured at the inlet and outlet of the monolith. The NH_3 inlet to the catalyst was a feedforward ANR dosing algorithm. Both inlet and outlet data was logged at 1 Hz, which was the sampling time used for simulation. The commercial software Matlab was used for simulation with an Intel Core i7-3630QM @ 2.4 Ghz processor.

5.2.1 Experimental Data

This section will present the data that has been used for validation. The presented data corresponds to one ETC test carried out with a given NH_3 profile. In this work three of these tests were available. Two of them were used for model validation as presented in this chapter, and one was used for full-scale calibration of the adsorption and desorption parameters, as presented in Chapter 4. The data presented here is from one of the tests that was used for model validation.

The inlet and outlet NH_3 can be seen in Figure 5.1. The NH_3 inlet concentration is highly transient and is updated every second, with changes in several hundred percent. The outlet concentration is greatly varying as well, randing from about 0 ppm to 150 ppm.

Figure 5.2 shows the inlet and outlet NOx concentrations in the validation data. The inlet NOx concentration is highly transient, ranging from close to 0 ppm to maximum values around 1500 ppm, in a matter of seconds. The outlet concentration is lower than the inlet concentration due to SCR reactions. If Figure 5.2 is compared to Figure 5.1, it can be seen that the test covers a broad range of ANR, ensuring that the model will be validated for a broad range of scenarios.

Figure 5.3 shows the inlet and outlet temperature for the validation data. It is important that a broad range of temperatures are included in the validation data, to ensure that all reactions take place, at different reaction rates. If the inlet and outlet temperatures are compared, it can be seen that the outlet is a smoothed version of the inlet temperature. The catalyst mass acts as a low pass filter. Since the presented models are 1D in the channel, the temperatures at which the reactions take place will be increasingly smoothed along the length of the channel. The broad range of temperatures ensures that the models are properly validated.

Figure 5.4 shows the space velocity at the inlet of the catalyst for the validation data. The space velocity is calculated with the inlet temperature, and will therefore be smoothed along the length of the channel, when the temperature is smoothed. The mass flow will however remain the same. The space velocity takes values between 5000 to 100000 hr^{-1}. The main effect of the space velocity is the mass

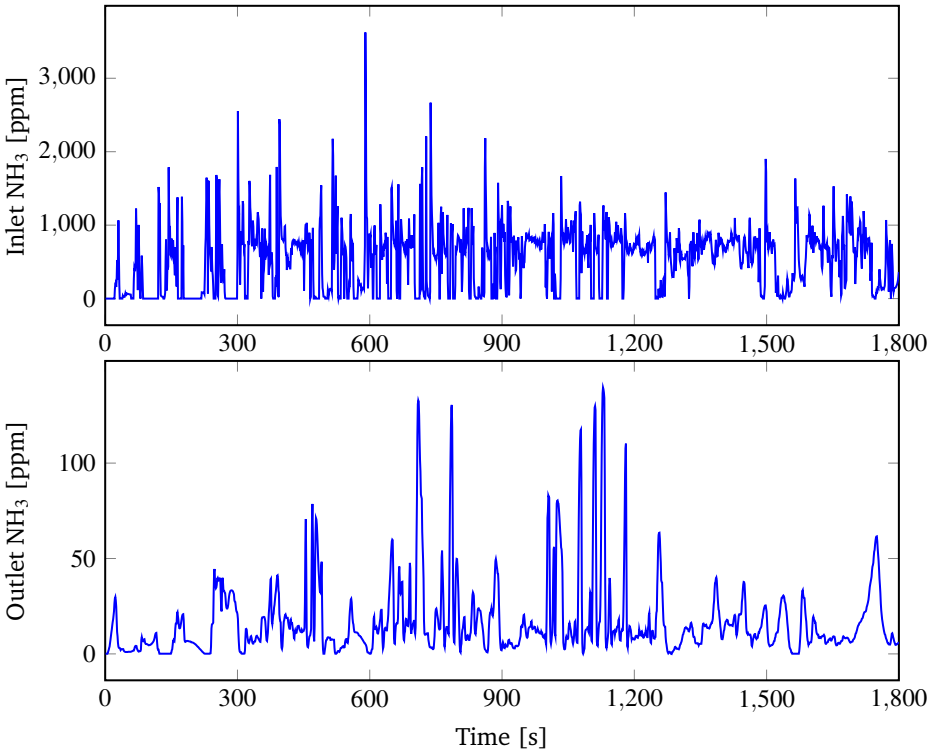

Figure 5.1. Experimental data used for validation of the previously calibrated models. The top plot shows the inlet NH_3 concentration, and the bottom shows the outlet NH_3 concentration. Legend: NH_3 (——)

transfer coefficients, which depends on the gas velocity. The space velocity also determines how long the gas hold up in the channel is. A higher space velocity means a lower residence time, and thus a shorter time for reactions to occur.

5.3 Methodology

This section will describe the methodology that has been used to validate the models. As previously stated, the basis for the validation is the models ability to predict the monolith outlet of NOx and NH_3 during the ETC. The models will be simulated and the model output and experimental data will be plotted in 600 s periods, to analyse how the models perform in the 3 parts of the ETC: urban, rural, and highway. The residuals for the same time periods will be analysed as well, to investigate if they have a normal distribution. Model 2 through 6 will be validated, while model

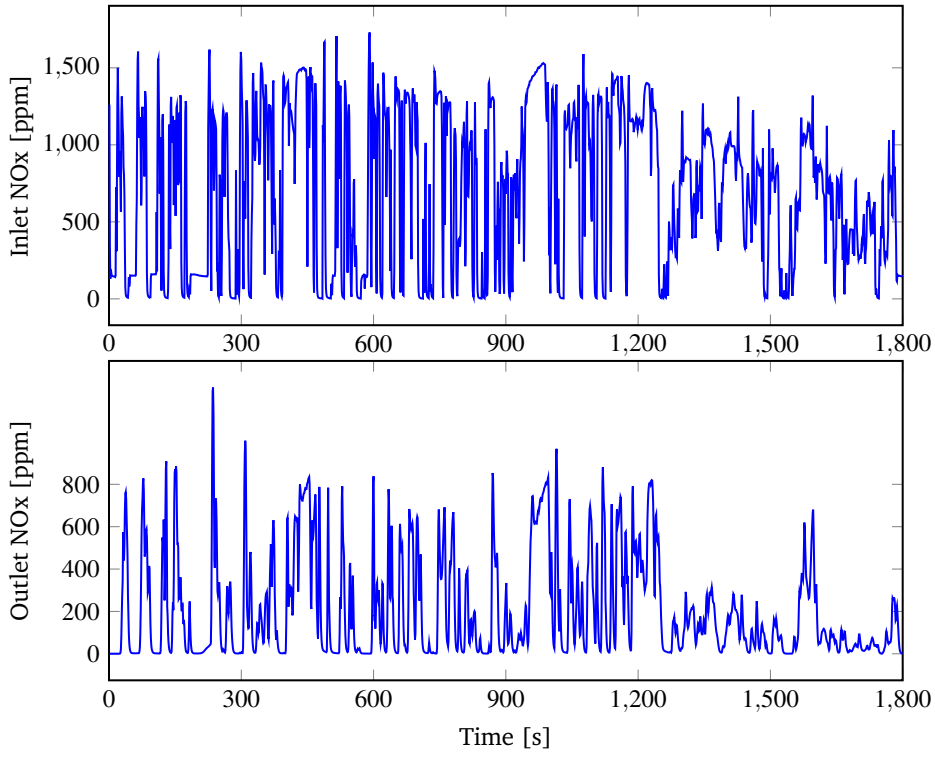

Figure 5.2. Experimental data used for validation of the previously calibrated models. The top plot shows the inlet NOx concentration, and the bottom shows the outlet NOx concentration. Legend: NOx (——)

1 is left out for reasons stated in Chapter 4. For model 2, the outlet temperature will be validated as well, and the difference between the gas temperature and wash coat temperature will be analysed.

The initial conditions for each model are determined by first simulating the model with zero initial conditions. The end values for the simulation are then used as the initial conditions for the real validation test. This is how the test are carried out in the experimental setup, and is a common way to condition the monolith before a test.

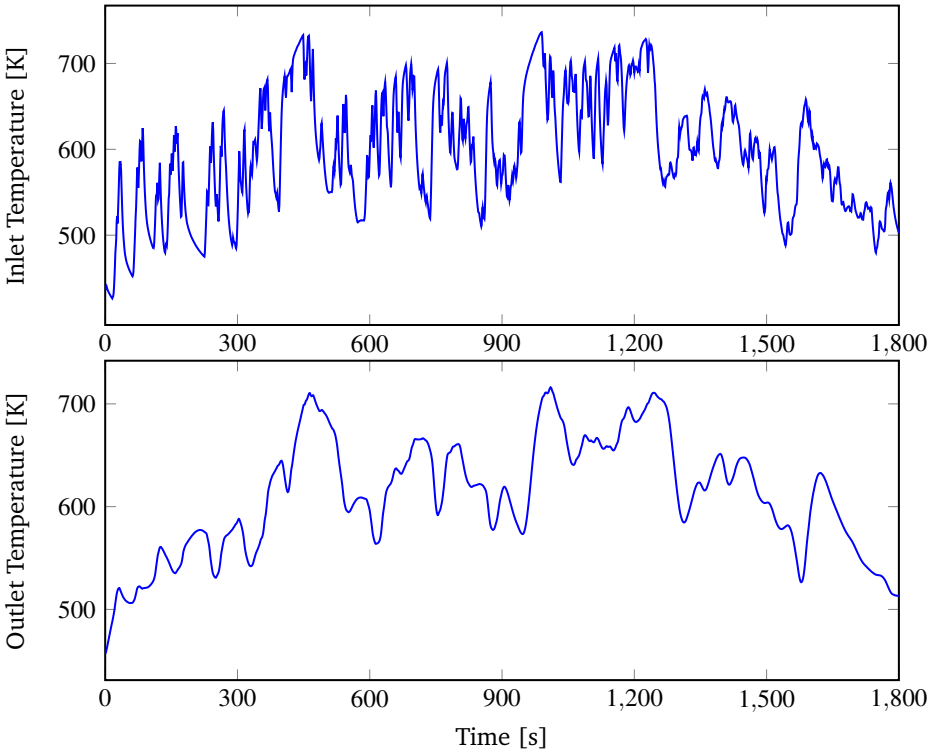

Figure 5.3. Experimental data used for validation of the previously calibrated models. The top plot shows the inlet temperature, and the bottom shows the outlet temperature. Legend: Temperature (——)

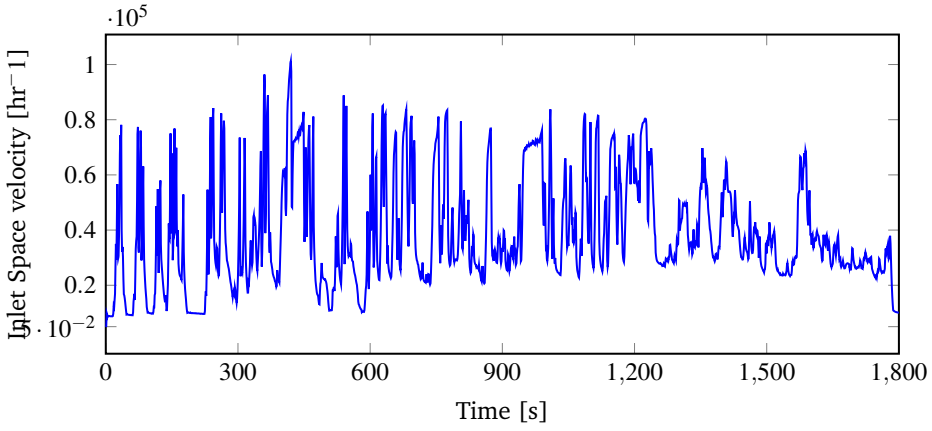

Figure 5.4. Experimental data used for validation of the previously calibrated models. Inlet space velocity. Legend: Space velocity (——)

5.4 Results

This section will present the validation results, using the data presented in Section 5.2.1. One other ETC test was used for validation as well, however these results will not be shown here, since they were similar to the ones presented here.

5.4.1 Model 2

5.4.1.1 NOx and NH_3

The results from the validation of model 2 can be seen in Figure 5.5, which shows a comparison between the simulation and the measurements at the outlet of the catalyst. The NO_x prediction follows data well, and the dynamics as well as the levels are correct for most of the simulation. It can be noted that the peaks of the model are sharper than for the data. This can be attributed to both the fact that the model does not include channel dispersion, which would smooth the peaks slightly. It is also an effect of the measurement equipment, which naturally smooths the data peaks more than what is actually coming out from the monolith. The NH_3 prediction is satisfactory for the majority of the data set, but there are periods especially between 600 and 1200 s where there is a substantial difference between data and simulation. It appears that the NH_3 slip is generally underestimated.

The normalised residuals for Figure 5.5 can be seen in Figure 5.7. The top plot shows the NOx residuals and the bottom plot shows the NH_3 residuals. The NOx residuals has approximately the same number of values above zero, as under zero. The residuals are generally lower in the last 600 s of the test, which is because the last segment is less transient than the others. The residuals are normal distributed. The residuals for NH_3 confirms that the NH_3 slip is generally underestimated. The majority of the residuals are bigger than 0, meaning that the model prediction is lower than the data. The time period between 1000 and 1300 s is when the residuals are biggest. It can be seen that the negative NOx residuals are smaller than 1, even though they are normalised. This is due to how the normalisation was done. All residuals were divided by the largest positive residual, meaning that there are some negative residuals that have a bigger numerical value than the biggest positive residual.

Figure 5.6 shows the difference between the gas and wash coat concentration in the middle of the monolith channel for NOx during a small time period in the validation test. No experimental data is available to validate this, however examining the plot shows that there is a difference between the concentrations. The

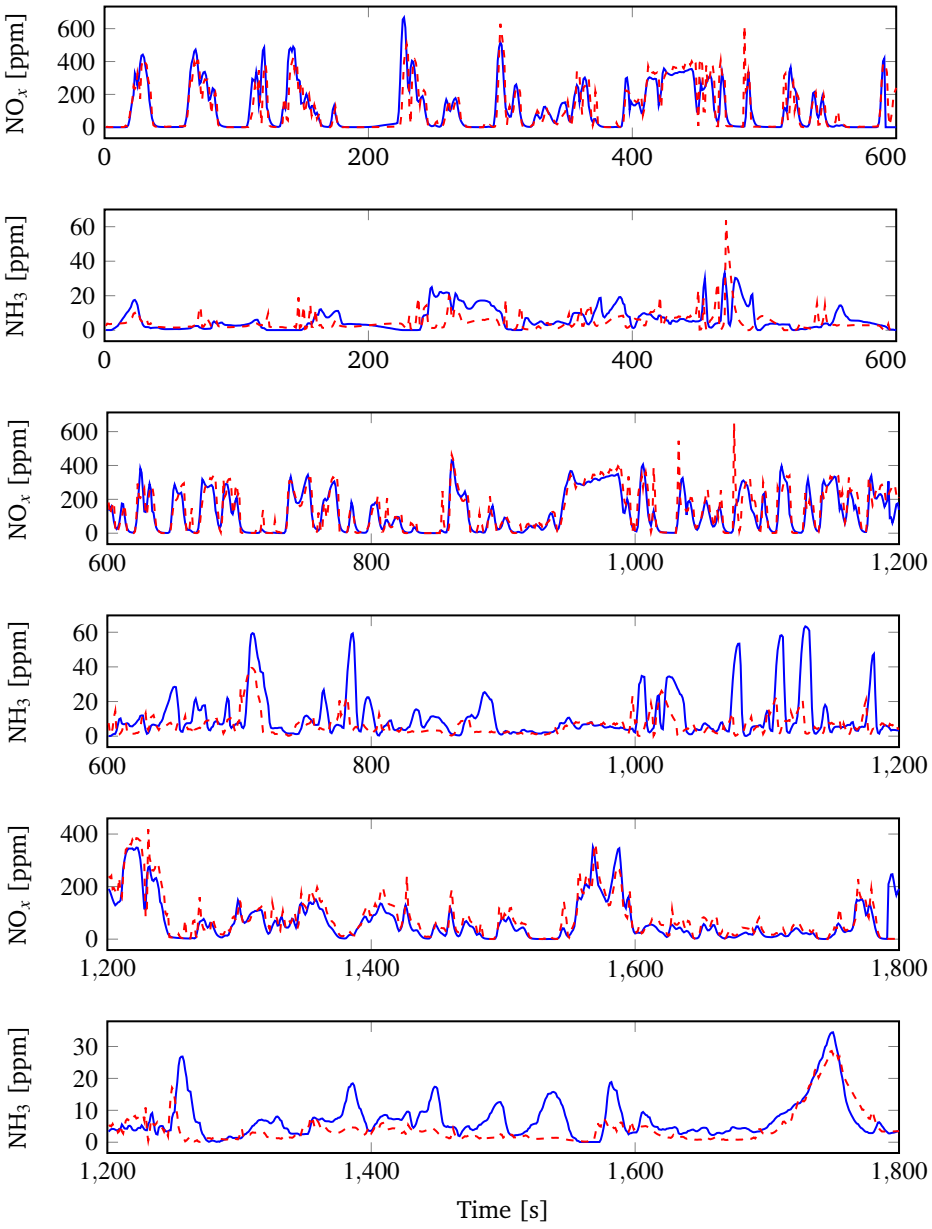

Figure 5.5. Full-scale monolith ETC validation for model 2. The two top pictures shows the NO_x and NH_3 comparison between data and simulation for the first 600 s of the test. The two middle pictures shows the same for the following 600 s, and the bottom two pictures for the last 600 s. Legend: Experimental data (——), Model (- - -).

difference in concentration depends on the current conditions in the monolith, and is therefore time dependent. As seen, the difference in concentration is smaller in the beginning than in the end of the time period. The maximum difference is around 50 ppm, which is not unreasonable. The wash coat concentration is, in this case, lower than the bulk concentration. This is dependent on the temperature, and if the NH_3 oxidation is active. The analysis shows that the models shows realistic behaviours regarding this, and the application of the hawthorn correlation for mass transfer coefficients, can be said to be successful.

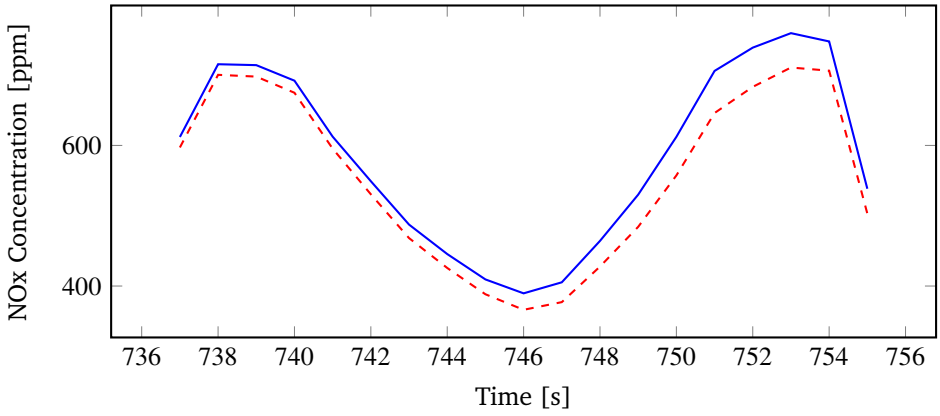

Figure 5.6. Comparison between the NOx wash coat and bulk concentration in the middle of the monolith channel, for a small time period in the test. Legend: Channel concentration (——), Wash coat concentration (- - -)

The model prediction and residuals shows that model 2 is able to accurately predict the behaviour of SCR monolith. The NOx performance is better than the NH_3 performance, which is expected due to the lack or proper adsorption and desorption calibration data.

5.4.1.2 Temperature

Figure 5.8 shows a comparison between the simulated output temperature and the measured output temperature. The model is able to predict the output temperature to a close to perfect degree. There are periods, especially in the beginning, where the model underestimates the temperature by around 100 K, however this can be attributed to initial conditions. To analyse the difference between the wash coat temperature and channel temperature, Figure 5.9 can be examined. The figure shows the temperature in the middle of the catalyst for a small time segment in the

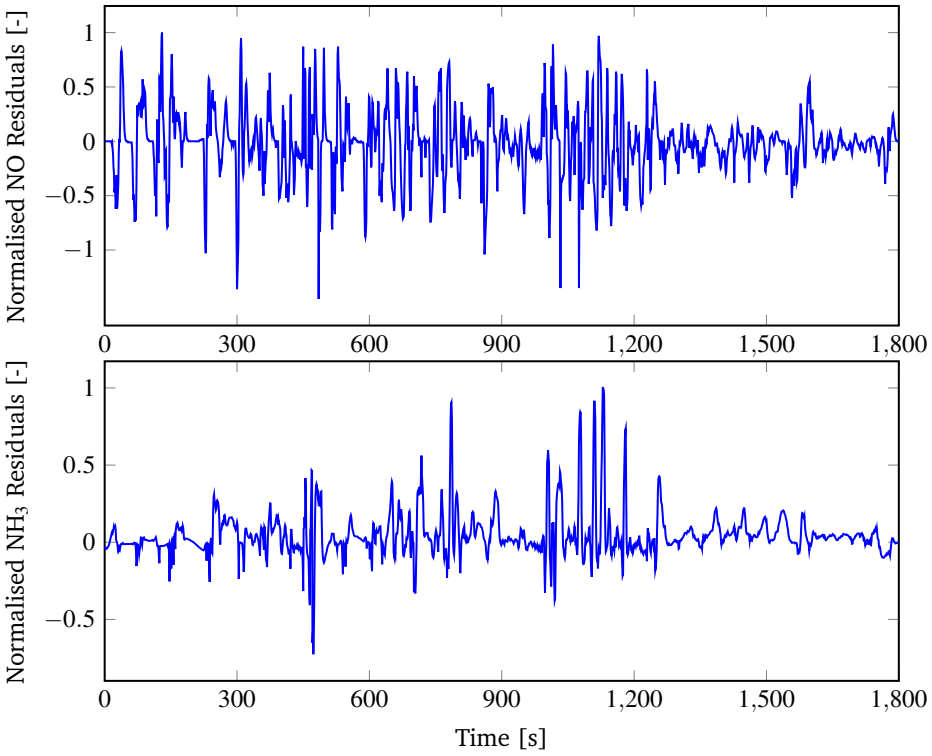

Figure 5.7. Residuals for NOx and NH_3 during full-scale validation with model 2.. The top plot shows the NOx residuals, and the bottom plot shows the NH_3 residuals. Legend: Residuals (——)

test. It can be noted that there is a temperature difference of approximately 15 K in parts of the figure. This can also be seen in other parts of the test, when examined. A temperature difference of 15 K will lead to a not insignificant difference in reaction speed. It can be seen that, depending on the inlet temperature, the temperature either rise or fall, and the wash coat or channel gas can be the hottest. The validation data does not include any measurements of the temperature difference between the wash coat and gas, so it cannot be validated with experimental data. The analysis however shows that the results are reasonable, and it can be concluded that the estimation of the heat transfer coefficient has been successful.

5.4.2 Model 3

This section will present the validation results for model 3. Figure 5.10 shows the comparison between data and simulation for model 3, during a simulation of the

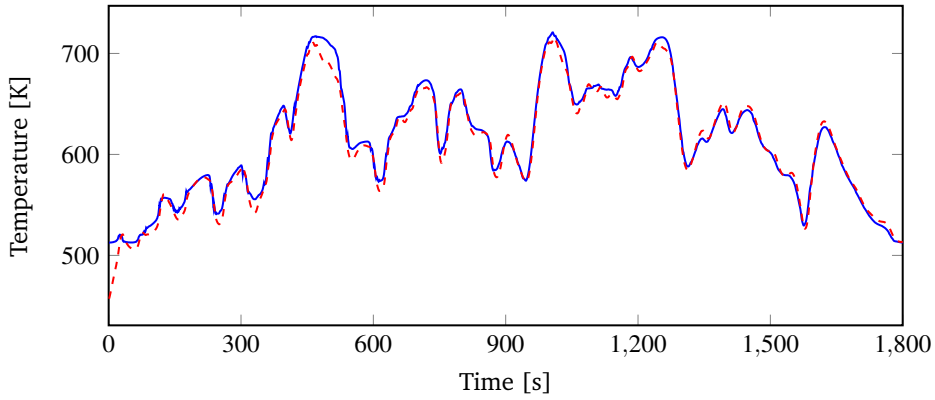

Figure 5.8. Full-scale monolith ETC validation for model 2. Comparison between monolith temperature output for model and experimental data. Legend: Experimental data (——), Model (- - -).

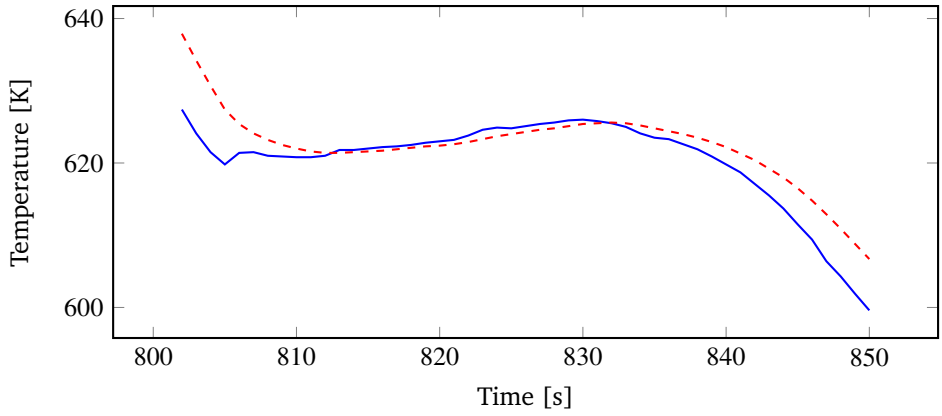

Figure 5.9. Full-scale monolith ETC validation for model 2. Comparison between the channel gas temperature and the wash coat temperature, in the middle of the monolith channel, for a 50 s time period. Legend: Channel temperature (——), Wash coat temperature (- - -).

ETC. The simplifications related to mass transfer does not appear to have hindered the NOx prediction substantially, and the model predicts the outlet of NOx accurately, both with regards to absolute value, and the dynamics. As with model 2, the peaks during rapidly changing concentrations are exaggerated compared to the experimental data. This can be seen especially between 600 and 1200 s. At the end of the test there is a section where the model is predicting zero, while the

data takes other values. This is because of the time shift that was explained in the methodology.

The model is performing worse with regards to NH_3 slip compared to model 2. In the first 600 s, the model is overestimating the NH_3 slip, and notably there are peaks that are wrong with regards to dynamics at 200 and 550 s. Between 600 and 900 s, the model is performing well, and the dynamics are correct. Between 1000 and 1200 s then model appears to have the correct dynamics, however the peaks are too small. For the last 600 s, in the bottom of Figure 5.10, The slip peaks appear to be slightly delayed compared to data. It can also be seen that the last big peak is not captured by the model, compared to model 2, where it was predicted correctly.

Figure 5.11 shows the normalised residuals for the ETC test with model 3. The residuals for NOx, in the top plot, are normally distributed, and appears as noise with different intensity, and approximately equal amounts above and below zero. As with model 2, the residuals are lower in the last 600 s. The majority of residuals are close to zero.

The NH_3 residuals in the bottom of Figure 5.11 does not have as clear normal distribution as for NOx. Notably, at 200 s, there is a segment of residuals that have a clear trend. It would therefore be possible to predict the residuals, which implies a model error. A similar segment of residuals, but positive, is present at 1750 s. For the rest of the test the residuals looks like noise, but with a majority of them being positive.

5.4.3 Model 5

Figure 5.12 shows the comparison between data and simulation for model 5, during a simulation of the ETC. The effect of the simplifications are the combined effects of models 3 and 5, meaning that the model does not include the mass transfer to the wash coat, and that the model does not have thermal mass and heat transfer to the wash coat. It can be seen that the NOx prediction is substantially worse than than for model 2 and 3. The NOx peaks are, as with the other models, higher than the data peaks. There are also NOx peaks occurring when there is no peaks in the data. For example in the period between 600 and 800 s, the model predicts several peaks when the data does not show any.

The NH_3 comparison in Figure 5.12 shows that the model cannot predict the NH_3 slip to a satisfactory level. In the beginning of the test, two major peaks occur that are not corresponding to data. These peaks are due to the initial adsorbed NH_3

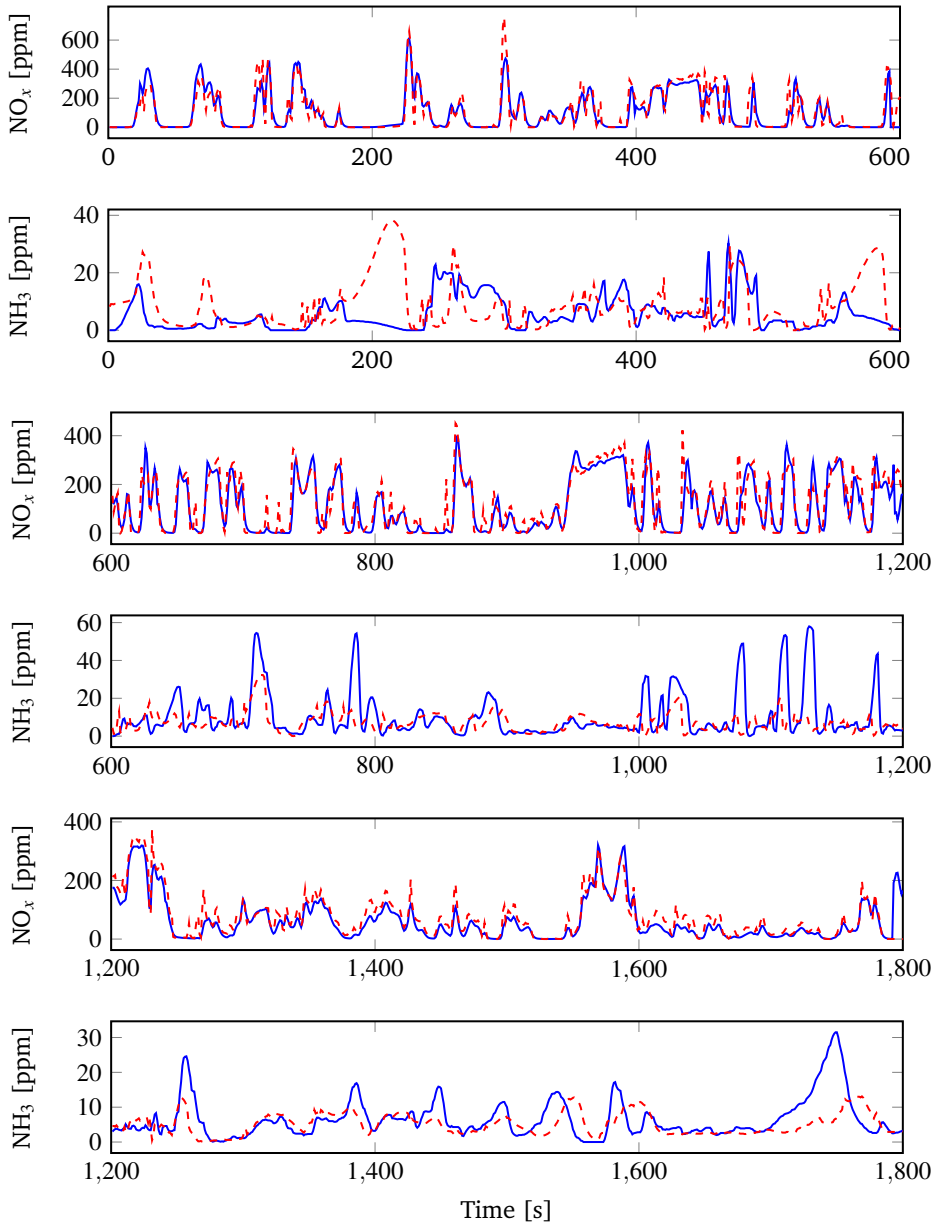

Figure 5.10. Full-scale monolith ETC validation for model 3. The two top pictures shows the NO_x and NH_3 comparison between data and simulation for the first 600 s of the test. The two middle pictures shows the same for the following 600 s, and the bottom two pictures for the last 600 s. Legend: Experimental data (——), Model (- - -).

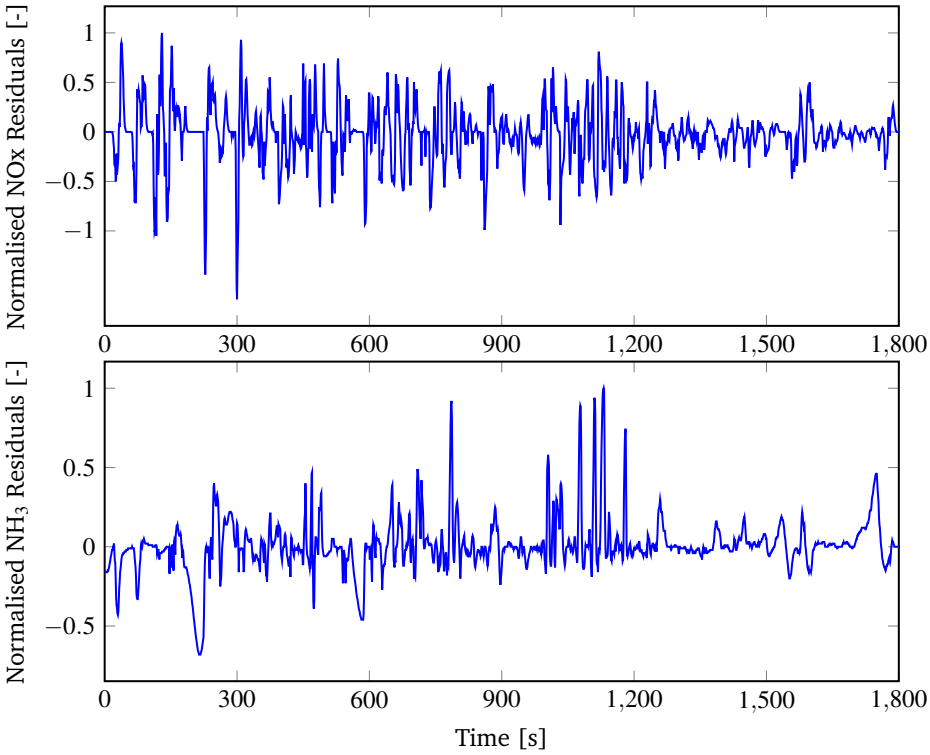

Figure 5.11. Residuals for NOx and NH_3 during full-scale validation with model 3. The top plot shows the NOx residuals, and the bottom plot shows the NH_3 residuals. Legend: Residuals (——)

being desorbed, and it appears as if the used methodology to produce the initial conditions does not work well for this model. Throughout the rest of the test, the NH_3 slip is at a constant low level. The high adsorption coefficient that was achieved during calibration in Chapter 4, makes the desorbed NH_3 adsorb to the surface again, the high levels of adsorbed NH_3 also results in significant amounts of NH_3 being converted to NO as a result of NH_3 oxidation during temperature peaks.

Figure 5.13 shows the normalised residuals for NOx and NH_3 when model 5 is used. The NOx residuals does no longer appear to be random and normal distributed, for some segments. For example the residuals in the first 200 s have a tailing behaviour, which suggests that the residuals are not random. The residuals are lower for the later parts of the test, which was the case for the other models as well. There is still a good division between positive and negative residuals, which

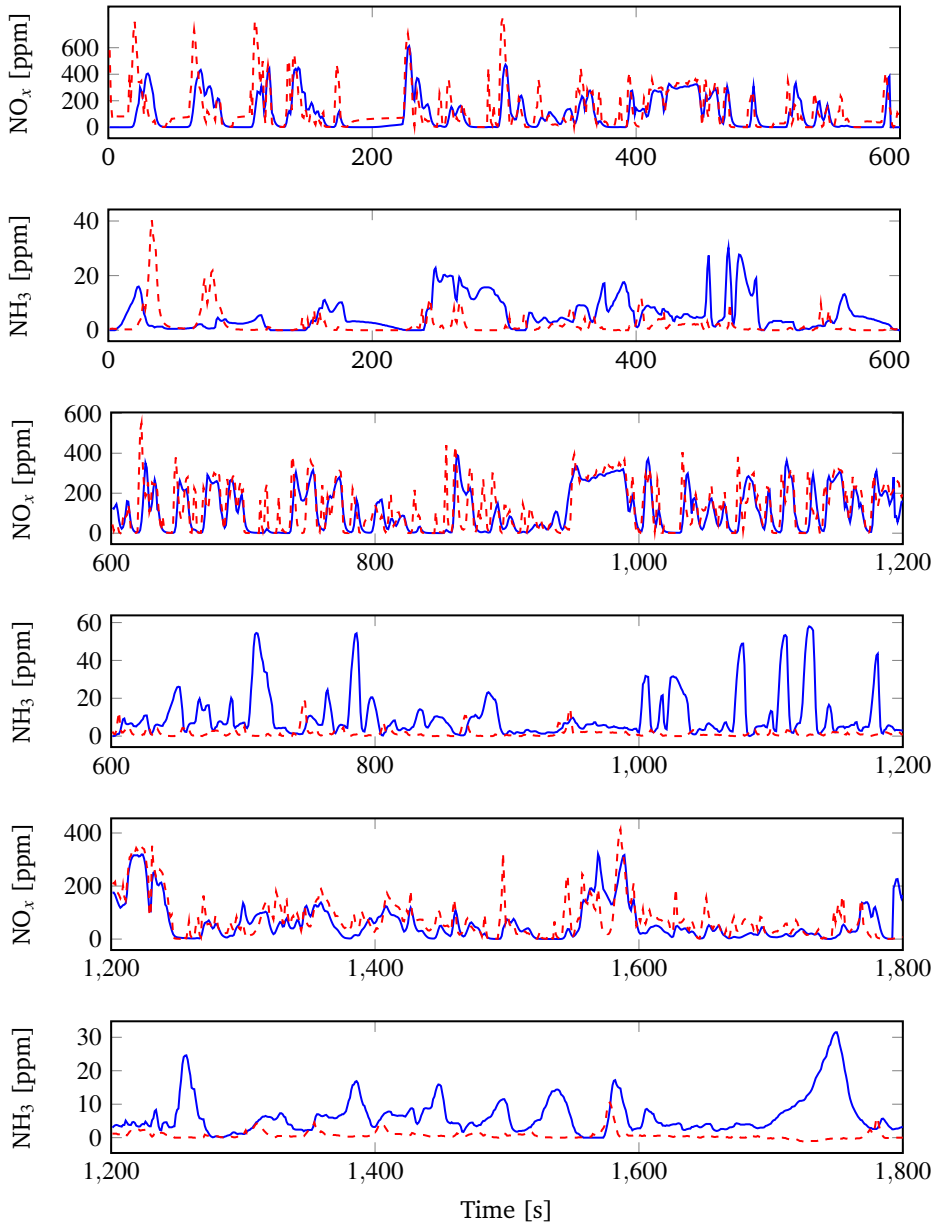

Figure 5.12. Full-scale monolith ETC validation for model 5. The two top pictures shows the NO_x and NH_3 comparison between data and simulation for the first 600 s of the test. The two middle pictures shows the same for the following 600 s, and the bottom two pictures for the last 600 s. Legend: Experimental data (——), Model (- - -).

shows that the model, at least for parts of the test, do not show systematic errors.

The NH_3 residuals in the bottom of Figure 5.13 are generally larger than zero, meaning that the model underestimates the NH_3 slip. The big release of the initially adsorbed NH_3 can be seen in the beginning, while most of the rest of the residuals are positive. The middle segment between 600 and 1200 s has the largest residuals, which is due to the data showing major NH_3 release, while the model does not. In the end of the test, the big residual corresponds to the NH_3 that is shown in data, but the model does not predict.

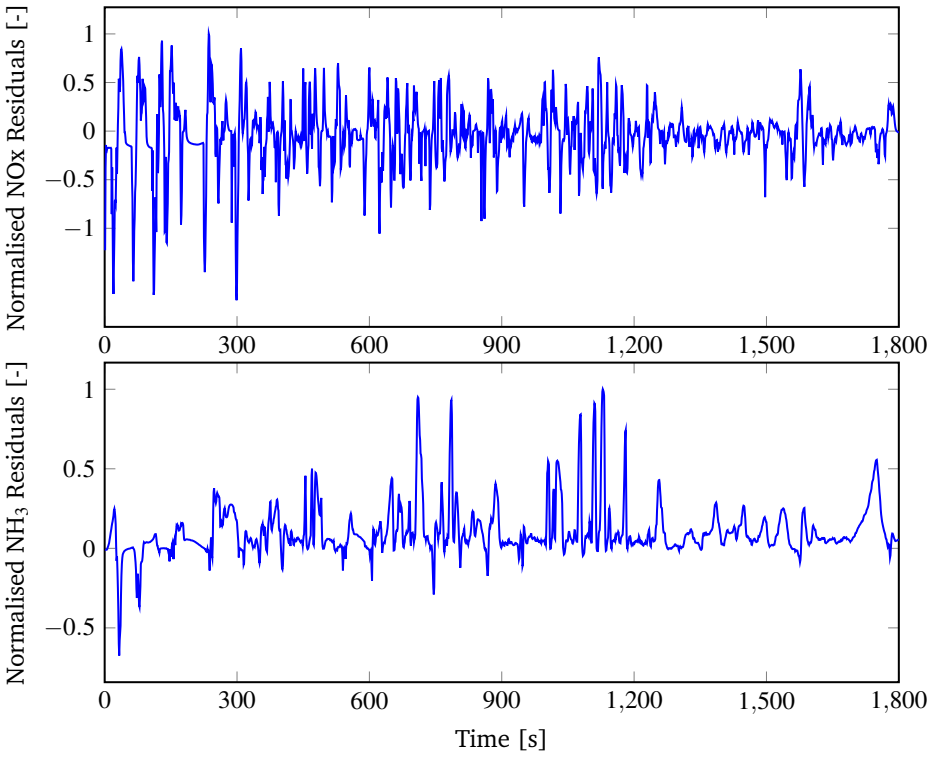

Figure 5.13. Residuals for NOx and NH_3 during full-scale validation with model 5. The top plot shows the NOx residuals, and the bottom plot shows the NH_3 residuals. Legend: Residuals (——)

5.5 Discussion

The results have shown that all models are quite good at predicting the SCR monolith outlet of NOx during an ETC test. As expected, model 2 performs the best both

in relation to NOx prediction and NH_3 prediction. This is expected since it is the model with the least simplifications of the ones validated. The results for model 5 showed that the simplifications related to heat transfer and mass has a significant impact on the performance of especially NH_3 prediction. Both models 2 and 3 were able to capture the overall trends of NH_3 slip, although model 2 better, while model 5 was not able to capture any of the dynamics of NH_3 slip. As presented in Chapter 4, the adsorption and desorption parameters of model 5 were recalibrated with full-scale data, similar to the data used in this chapter. The model was still not able to predict NH_3 slip. It can therefore be said to be a problem with the model structure, instead of the calibration data. It is unlikely that the model would predict the correct NH_3 slip, even if the adsorption and desorption related parameters were calibrated with better data.

The validation of model 3 showed that the model was able to predict the NOx slip to a very similar level of model 2. This is expected, since the result of the simplifications of model 3 is that information about the mass transfer will be included in the kinetic parameters. For NH_3 however, the model is clearly worse than model 2. While there are some peaks in the cycle that actually are predicted better than with model 2, several peaks appear that should not be there, and others are heavily underestimated. The reason for this is difficult to find, however one possible explanation is that the removal of the mass transfer makes the model more sensitive to incorrect initial conditions. The initial conditions will always be an uncertainty in model simulations in this application since they are unknown. For example, the wash coat temperature is not known. After the conditioning test the catalyst is allowed to cool down slightly for approximately 10 minutes before the next test is started. There might thus be an error related to this. Another highly impacting state is the NH_3 coverage ratio at the beginning of the test. Unless advanced measurement technologies are used, this is unknown, and has to be estimated with the model itself. If there are inaccuracies in the model, the initial conditions will be wrong. However, based on the performance of model 2 and 3 in the beginning of the test, it does appear as if the used methodology has been successful.

Model 2 has the required accuracy to be used to draw conclusions about the performance of urea dosing controllers, a subject that will be the topic of Chapter 7. A requirement for this is that the model can accurately predict NOx and NH_3 slip, which model 2 has shown itself capable of. When control algorithms are tested for the SCR catalyst, the requirements are partly based on how they perform during a

transient cycle, such as the ETC. If the model can accurately predict the system during transient operation, conclusions can be drawn about how the controller works.

5.6 Conclusions

The methodology that has been used to validate model 2, 3 and 5 has been presented. The methodology uses full-scale monolith data produced with a full-scale engine following the ETC. The results have shown that while models 2 and 3 perform satisfactory with regards to NOx prediction, the simplifications of model 5 makes it less suitable for this application. Model 2 can to some degree predict the NH_3 slip, however it is underestimated. Model 3 and 5 performs worse than model 2. It is believed that the accuracy of model 2 is enough for it to be used in the development of urea dosing controllers.

Chapter 6

Analysis of the SCR Monolith Models

This chapter presents an analysis of the predictive performance for NOx for some of the models presented in Chapter 3. The calibration of model 2 was taken as the reference case, and the other models were initially coupled with the kinetic parameters of model 2, and their predictive performances were compared. The models were also coupled with their own kinetic parameters, and analysed again. The results show that, after recalibration, the model that included simplifications related to mass transfer was able to keep most of its predictive capabilities, while the simulation time was reduced substantially.

The main contribution of this chapter is published in an article (A. Åberg, A. Widd, J. Abildskov, J. K. Huusom. Parameter Estimation and Analysis of an Automotive Heavy-duty SCR Catalyst Model. Chemical Engineering Science 161 (2017) 167-177). Early work related to this chapter was presented at the 2015 AIChE Annual Meeting, November 8-13, 2015, Salt Lake City.

6.1 Introduction

In this thesis several different models has been developed and calibrated in previous chapters. The choice of model complexity is an important decision for simulation of the system, since an unnecessarily complex model takes a longer time to simulate. Selection of the proper model complexity for the control design and the state estimation is also crucial to get a controller that is able to meet the requirements both with regards to accuracy and simulation time. Modeling of the SCR catalyst is a well-studied area, with contributions of different complexity for example in [115, 78, 106, 21, 28, 20, 15]. Previous work have investigated both high accuracy models that typically are used for simulation purposes and phenomena understanding, and simpler models that can be used in for example control applications. To the authors knowledge, little work has been done to investigate the effect different simplifications on the physical modeling level has on simulation accuracy. Work has been done for the ASC [26] to investigate the importance of wash coat diffusion modeling, or the analysis of controller models [111] for the SCR. For control purposes, such analysis is important because simplifications done to the underlying physics model can reduce simulation time substantially. Another thing that can help reduce computational effort is to use a smaller discretisation grid. Simplifications of the underlying physical model, that significantly reduces computational effort, without reducing accuracy below the required level, would be desirable.

The contribution of this chapter is an investigation on the effect different simplifications on the channel model have on the predictive capabilities related to NO_x, by analysing calibration results and full scale engine tests. The results are used to draw conclusions on which simplifications are most valuable if a faster, while still accurate simulation model is required, with applications for example in simulation and control. Model 2 is used as the reference, and models 3, 4, and 5 are analysed to different extents.

The methodology that has been used to analyse the information loss will be presented, and the results for the different models.

6.2 Methodology

This section will present the methodology that has been used to analyse the effect different simplifications to the channel model has on the NOx prediction.

Models 2, 3, 4 and 5 presented in Chapter 3 were analysed in terms of how well they can predict the monolith output of NOx during an ETC test. This was quanti-

fied with the Sum of Squared Error (SSE) as in Equation (6.1), the mean error as in Equation (6.2), the standard deviation of the error as in Equation (6.3), the coefficient of determination, R^2 as in Eq. (6.4), and by analysing where the different models perform the best and the worst. The predictive sensitivity regarding discretisation was also analysed, and the importance of accounting for measurement delay in full scale conditions. Finally, the models were compared with regards to computation time. The models were all coupled with the presented kinetic model with the same parameter values as the model 2 in the first analysis. After this, models 3 and 5 were analysed with their specific kinetic parameters achieved in Chapter 4 due to their performance with the kinetic parameters from model 2. The analysis was repeated, to see if a recalibration is enough to account for the information loss in the simplifications. The progress of the model analysis combined with parameter estimation followed the following steps:

1. Model analysis using the described methods for models 2, 3, 4, and 5, using the kinetic parameters that were achieved with the calibration of model 2.
2. Recalibration of kinetic parameters for the most promising simplified models.
3. Model analysis of the simplified models using the new kinetic parameters from step 3.

$$SSE = \sum_i (y_i - f(u_i, \beta))^2 \tag{6.1}$$

$$\mu_{err} = \frac{\sqrt{SSE}}{n} \tag{6.2}$$

$$\sigma_{err} = \sqrt{\frac{\sum_i (y_i - \mu_{err})^2}{n}} \tag{6.3}$$

$$R^2 = 1 - \frac{\sum_i (y_i - f(u_i, \beta))^2}{\sum_i (y_i - \mu_{err})^2} \tag{6.4}$$

The commercial software Matlab was used for simulations and analysis with an Intel Core i7-3630QM @ 2.4 GHz processor.

6.3 Results

This section will present the results from the model analysis. It will start by presenting the results for the models before they were recalibrated, and continue with the

same analysis with the recalibrated models. The analysis was done by comparing simulation results with experimental data for a full ETC with a full-scale monolith and real engine, which had the same specifications as in Chapter 5.

6.3.1 Time shift and discretisation

Figure 6.1 shows the SSE for NO_x for model 2 when the time correction for measurement delay and the number of discretisation points are varied. The results shows that correcting for measurement delay is of great importance to get accurate results. The highly transient ETC test means that the inlet as well as outlet concentration of the species varies dramatically on a short time scale. The model has no measurement delay, but in the experimental setup the outlet gases are transported through pipes to the analysis equipment, thus introducing delay. The time of the delay is unknown, and it is therefore assumed that the time shift that gives the smallest error to data, is the delay. The optimum was found to be a correction in the model of 8 s. This was used for all the models. It can be seen that the results are insensitive to the number of discretisation points used. Even going as low as 5 points for a full-scale monolith leads to a small difference. This makes it possible to reduce the number of discretisation points as it highly affects simulation time. It can be noted that at a 8 s time correction, the case where N = 10 performs slightly better than the other. This is explained by the fact that N = 10 was used during parameter estimation. The simulation time for the different discretisation numbers were:
N = 5 : 345 s
N = 10 : 520 s
N = 20 : 1029 s
N = 30 : 1403 s
For all remaining simulations, the number of discretisation points were chosen as 10.

6.3.2 Analysis Using Kinetic Parameter of Model 2

Table 6.1 shows a summary of the different measurements for information loss when the kinetic parameters of model 2 were used for all models. Model 2 performs the best in all categories. It has the lowest mean error and standard deviation of the error, and also has the highest R^2-value. The direct transfer of the kinetic parameters has the smallest effect on model 3, which has an R^2-value of 0.66 compared to model 2 with a value of 0.78. The simulation time for model 3 is 351 s compared

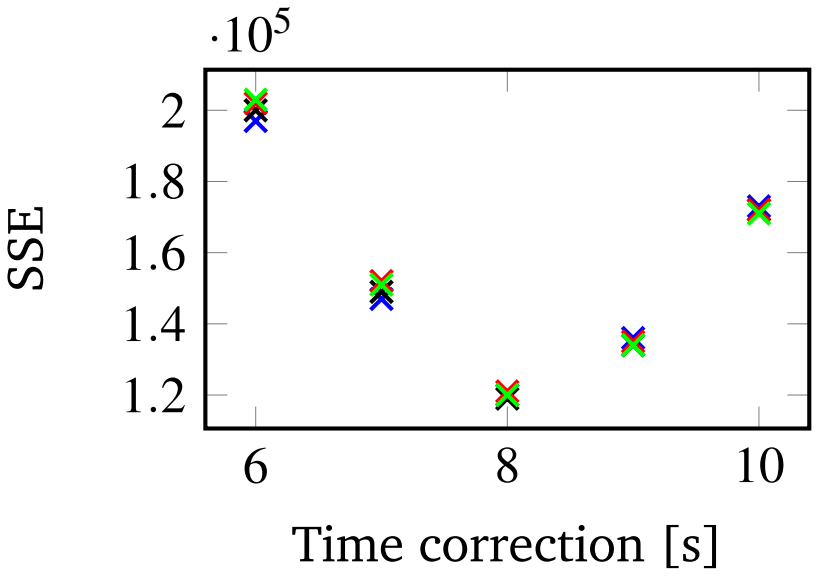

Figure 6.1. SSE for NO_x with model 2. The time correction corresponds to the shift that is needed to compensate for measurement time. N are the number of discretisation points used. Legend: N = 5 (×), N = 10 (×), N = 20 (×), N = 30 (×).

to the model 2 at 520 s, making model 3 a promising choice for further analysis. Model 4 and 5 performs worse than the other two. The Arrhenius expression is only affected by changes in the reaction temperature, as seen in Equation (3.78), and it is therefore likely that these should be affected the most by the transient temperature resulting from removing the thermal mass. There is a small difference in performance between model 4 and model 5, indicating that the temperature simplification is the most dominant and leads to most of the information loss. If there are combinatorial effects from the two simplifications, they are small. The simulation time for the different models follows the expected trend based on the discussion in Chapter 3. Model 2 has the longest simulation time, followed by model 3, 4, and 5, respectively. The low simulation time for model 5 justifies that the parameters are included in a recalibration procedure, even though the performance is substantially worse than models 2 and 3, to investigate if the kinetic parameters can compensate for the information loss. It is on the basis of these results that models 3 and 5 were calibrated in Chapter 4. The performance of model 4 was too poor to motivate the extra time effort to calibrate its parameters.

The cumulative SSE for models 2, 3, 4, and 5, while using the kinetic parameters of model 2, can be seen in Figure 6.2, which confirms the results of Table 6.1.

Table 6.1. Summary of information loss before calibration for all presented models.

	Model 2	Model 4	Model 3	Model 5
Acc. slip [gNOx/kWh]	2.46	2.54	2.41	2.48
SSE	$1.19 \cdot 10^5$	$2.32 \cdot 10^5$	$1.43 \cdot 10^5$	$2.35 \cdot 10^5$
Mean error [ppm]	66	129	76	130
Std. dev. error [ppm]	101	153	124	155
R^2	0.78	0.16	0.66	0.14
Simulation time [s]	520	411	351	203

Table 6.2. Summary of information loss, using the kinetic parameters specific for each model, for model 2, model 3, and model 5.

	Model 2	Model 3	Model 5
Acc. slip[gNOx/kWh]	2.46	2.54	2.41
SSE	$1,19 \cdot 10^5$	$1.29 \cdot 10^5$	$2.21 \cdot 10^5$
Mean error [ppm]	66	72	123
Std. dev. error [ppm]	101	92	143
R^2	0.78	0.77	0.27

Models 3, 4, and 5 performs significantly worse consistently throughout the test cycle. The difference between model 4 and 5 is very small, and it is difficult to draw conclusions on which part of the test model 4 outperforms model 5. The curves overlap in the majority of the test, however a slight difference can be seen at the end of the first 600 s part of the test. The difference between models 2 and 3 is small as well. In the last two segments of the test, the curves overlap for a majority of the test, however model 3 is slightly above model 2. The major difference in performance can be traced to the first segment, where there is a clear difference between model 2 and 3. The fact that the mass transfer related simplifications appear to have the largest effect in the first segment of the test is thus confirmed both by model 2 performing better than model 3, and that model 4 performs slightly better than model 5, in the first segment.

6.3.3 Analysis Using Kinetic Parameters Specific to Individual Models

Figure 6.3 shows the cumulative SSE for model 2, and models 3 and 5 using their specific kinetic parameters. The figure is divided into three sub-plots, where each represents one 600 s section of the ETC. The cumulative SSE was reset after each section, to analyse where the different models were performing the best. Table

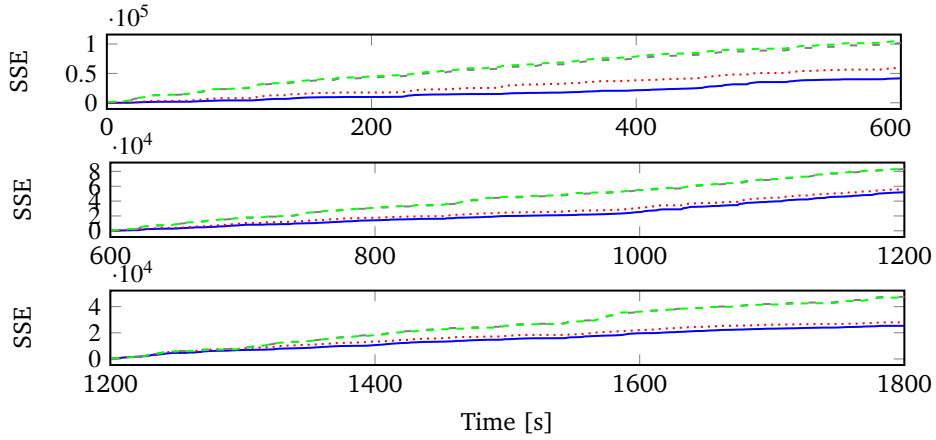

Figure 6.2. Cumulative SSE for model 2, model 3, model 4, and model 5, using the kinetic parameters of model 2. The top picture shows the three models during the first 600 s of the ETC. The second shows the same for the following 600 s and the last shows for the last 600 s. Legend: Model 2 (——), Model 3 (·····), Model 4 (– –), Model 5 (– – –).

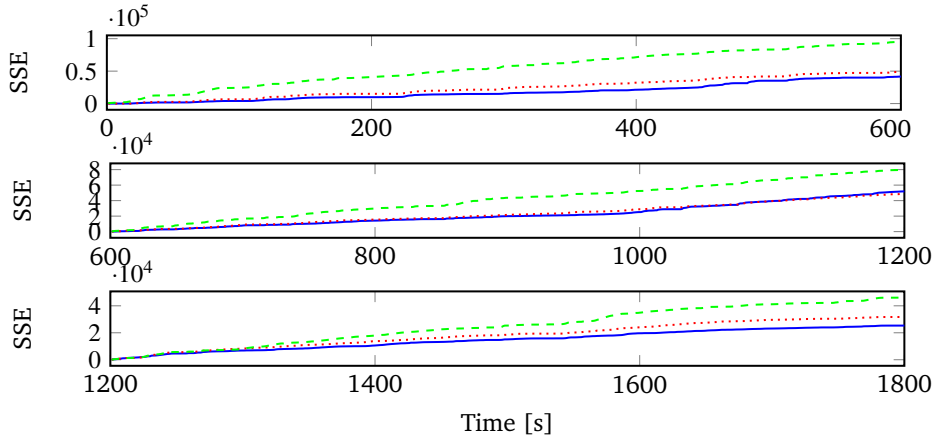

Figure 6.3. Cumulative SSE for model 2, model 3, and model 5, using the kinetic parameters specific for each model. The top picture shows the three models during the first 600 s of the ETC. The second shows the same for the following 600 s and the last shows for the last 600 s. Legend: Model 2 (——), Model 3 (·····), Model 5 (– – –).

6.2 shows a more detailed overview of the information loss after recalibration. As seen, the models were performing closer to model 2 after the recalibration. Model 3 achieves a R^2-value of 0.77, compared to model 2 that achieves $R^2 = 0.78$. The

average error and SSE was however still higher than for model 2. Figure 6.3 confirms that model 3 generally had a higher error than model 2, however during the second stage of the ETC, the models performed equally well. Model 5 was performing worse than the two other models in every measurement. These results show that recalibrating the kinetic parameters for the simplified models compensated for some of the information loss that occurred when simplifications were made. Model 3 was close to performing at the same accuracy level as model 2, however some of the kinetic parameters that were presented in Chapter 4 changed quite substantially. The new parameters are likely further away from their intrinsic values than the ones obtained when model 2 was used during calibration. The fact that models 3 and 5 performs better when kinetic parameters that are specifically calibrated using those models, are used, shows the significance of recalibrating a new model, and not using old kinetic parameters.

6.4 Discussion

The model analysis conducted in this paper showed that the model predictive capabilities regarding NO_x was highly affected by the assumption that the catalyst does not have any thermal mass and wash coat heat transfer. During steady state operation, as used for parameter estimation of the kinetic parameters in Chapter 4, this did not lead to any error, since the temperature of the monolith is already at operating condition at the start of the test, and does not change throughout the test. When the analysis on full-scale ETC tests was carried out, the effect of the simplification became significant, since the transient input varies greatly in temperature. A model that does not take into effect the smoothing of the temperature inside the monolith, greatly exaggerates the temperature in the majority of the catalyst, and therefore does not follow data well. A candidate for future work is a model that has thermal mass, but does not consider a temperature gradient between the channel gas as wash coat. Initial tests were carried out with this kind of model, however the simulation time was not greatly reduced. The goal of this work was to introduce simplifications that considerably reduced simulation time, and the model was therefore not included.

Out of the models including simplifications related to the transfer physics, the model that performed best in this work was model 3, that assumed infinitely fast mass transfer between the channel and wash coat. This assumption leads to higher concentrations of species in the wash coat than exists in the practical application, thus yielding faster reaction rates. This can be seen in Tab. 6.1, where the accumu-

lated slip of NO_x is lower for Model 2 than the Reference model. When the model was calibrated it was seen that the kinetic parameters has compensated for this increased concentration in the wash coat, and the accumulated NO_x slip is increased, as seen in Tab. 6.2. Model 3 is however still not capable of performing at the same level as model 2 after using its own kinetic parameters, indicating that fundamental limitations in the simplifications in model 3 that cannot be compensated by the kinetic parameters. Model 3 still performs close to the performance of model 2, with a substantial reduction in simulation time, and is therefore considered the best candidate to use in applications that require faster simulation time. The model was able to simulate a 1800 s data set in 351 s, approximately 5 times faster than real time simulations. This can be compared to model 2 that simulated the same data set in 520 s, corresponding to 3.5 times faster than real time.

The analysis performed in this work only focused on the NO_x performance. In the real application and control applications, NH_3 prediction performance is also of high importance. The simplifications here however only relate to physical phenomena, and before the analysis is performed on NH_3 as well, the assumption is that the results are transferable to NH_3 prediction. It should also be noted that the conclusions drawn in this work are only valid for the tested catalyst. A Cu or Fe based zeolite catalyst might show different behaviour regarding which simplifications result in the lowest information loss.

6.5 Conclusions

This chapter has presented an analysis where the predictive performance related to NOx was investigated for models 2, 3, 4, and 5. The models were first analysed using the kinetic parameters of model 2. This showed, as expected, that model 2 performed best. The performance of model 3 was close to model 2, while the simplifications of models 4 and 5 resulted in a significant information loss. Based on the results, models 3 and 5 were calibrated, as described in Chapter 4, and the analysis was carried out again. The results showed that using kinetic parameters specific for each model improved the predictive performance for all models. Model 2 was still the model that showed the best results.

Chapter 7

Controlling the Urea Dosing

Pareto fronts are used to analyse how changes in the control structure for the urea dosing to the automotive SCR catalyst can improve the trade-off between NOx slip and NH3 slip. Model 2 was used to simulate the European Transient Cycle (ETC) with P, PI, PD, and PID feedback controllers, combined with Ammonia-NOx-Ratio (ANR) based feedforward to control the urea dosing. The controllers were also tested in full-scale experiments, to compare with the simulation results. Results show that PI with feedforward performs best in simulation. Due to challenges in choosing parameters such that the appropriate span of the NOx-NH_3 trade-off is covered, conclusions from the experiments are difficult, however some conclusions from the simulation are transferable. It is also shown that combining feedback with feedforward performs better than only using feedback or feedforward. The main contribution of this chapter is published in one articles (A.Åberg, A. Widd, J. Abildskov, J. K. Huusom, Methodology for Analysing the NOx-NH3 Trade-off for the Heavy-duty Automotive SCR Catalyst, Submitted to The 20th World Congress of the International Federation of Automatic Control, 2017, Toulouse, Frace), and (A. Åberg, A. Widd, J. Abildskov, J. K. Huusom, Pareto Front Analysis of Automotive SCR Control. Submitted to Control Engineering Practice, 2017.)

7.1 Introduction

As discussed in Chapter 2, a promising and widely used technology for removing NOx is based on SCR, with NH_3 in the form of hydrolyzed urea as a reducing agent [41]. Challenges with this technology include dosing the appropriate amount of urea to reach sufficient NO_x conversion, while at the same time keeping NH_3-slip from the exhaust system below the legislation limit. This requires efficient control. Closed loop control of the SCR catalyst has been studied in literature [105, 53, 129], as well as feedforward based controllers [97, 110]. Challenges with feedback control are for example cross-sensitivity of NH_3 in NOx-sensors, dynamics with greatly varying time constants in combination with a transient system, and time delay in the urea dosing system [134]. The exhaust systems rarely has NH_3 sensors, making it difficult to use NH_3 based control.

An important constraint on a controller, in this application, is its ability to meet the legislation. However, to compare controllers that meet the legislation, another performance measure is needed. Due to the nature of the SCR catalyst, the evaluation is a trade-off between NOx slip and NH_3 slip. Contributions in literature often focus on optimising a single control structure for a given system, rather than a full analysis of how different control structures can improve the performance of the SCR catalyst. Using pareto fronts to graphically analyse the best possible trade-off between NOx slip and NH_3 slip for a given control structure, and how the trade-off can be improved by changing the control structure, can to the authors knowledge not be found in literature.

This chapter presents a methodology to graphically analyse the trade-off between NOx slip and NH_3 slip for the automotive SCR catalyst. The methodology can be used to investigate how changes in the urea dosing control structure improves or worsens the trade-off performance. The methodology is demonstrated by generating pareto fronts for a set of feedback controllers, both with and without feedforward. The pareto fronts are generated by simulating the European Transient Cycle (ETC) using model 2. The performance gain or loss for different control structures will be analysed graphically using the developed methodology. Additionally the controllers has been implemented in a full-scale engine setup to test the validity of the simulations.

7.2 Methodology

This section will present the methodology that has been used to generate the pareto fronts, along with the controllers that have been tested. The experimental setup that was used to validate the methodology will be described.

7.2.1 Pareto Fronts

The control problem in SCR monoliths is of a multi-objective nature due to the legislation which places limits on NOx slip, average NH_3 slip, and maximum NH_3 slip. To prevent a system from over-consuming urea for economical reasons, it is also natural to limit over consumption of urea. The set of solutions to a multi-objective optimisation problem can be represented as a pareto front, which is the curve representing the solutions that are pareto efficient. Pareto efficieny is a state where it is impossible to make an individual component of a cost function better, without increasing the overall cost of the cost function. In this work pareto fronts were used to represent the trade-off between NOx slip and NH_3 slip for different controllers. The process of producing the pareto fronts is shown in Figure 7.1. The process begins with deciding which controller to test, for example a P controller. The ETC was simulated with data from a engine without Exhaust Gas Recirculation (EGR) and with a displacement of 10 liters, using the controller with a certain K_c parameter. The cycle performance was evaluated, and the results were saved. This represented one data point on the pareto front. The process was repeated with a new K_c parameter, until a pareto front is complete. For controllers that have several parameters, such as a PI controller, the pareto fronts were generated using the same procedure, but for a certain T_i. T_i was then changed and another pareto front was produced by simulating the cycle for a range of K_c values, thereby giving information about the importance of the integral time. It was however expected that the integral time had limited influence on the cycle based performance because of the transient input of the ETC. The performance was evaluated using the NOx slip in g/kWh for the entire cycle, and the average NH_3 slip in volume ppm. The NOx mass is calculated by assuming that all NOx is NO_2, as the legislation is formulated [3]. The average NH_3 slip is calculated by taking the mean of all NH_3 outlet concentration measurements.

After the pareto fronts are generated a visual representation of the tested configurations of a control structure is achieved. This can be used to see if any controller satisfies the legislations. It also makes comparisons between controllers easy, as it becomes clear if a control structure outperforms another structure. The benefit of the analysis is that the conclusions on control structure should be independent of

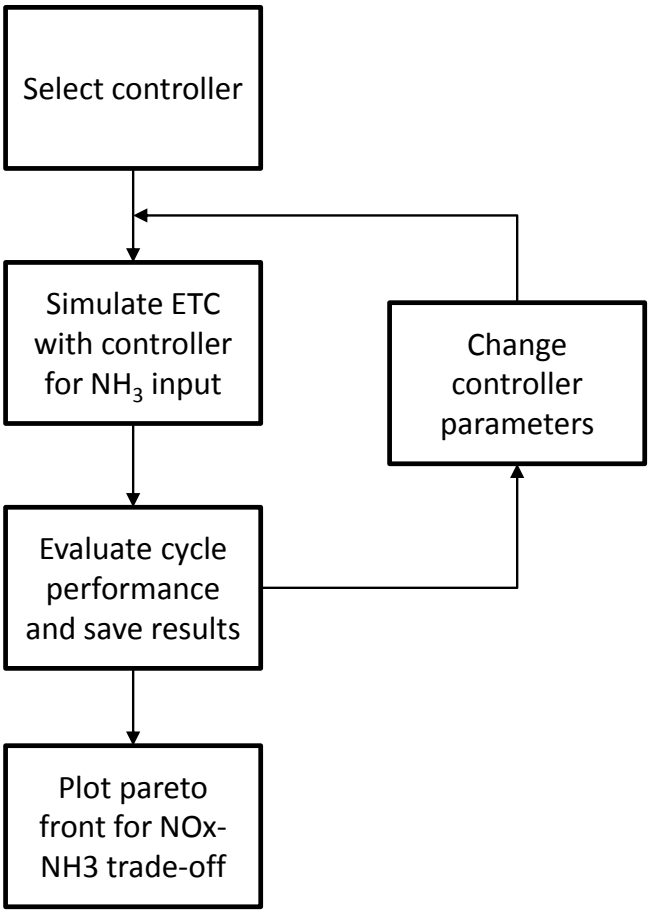

Figure 7.1. Procedure to generate the pareto fronts.

the size or activity of the monolith. The control parameters that were used are presented with each controller. The figures are however in most cases cropped, to only present relevant results. The pareto fronts presented here have a higher NH_3 slip and lower NOx slip than is typical for a monolith of this size. This is done because the differences between the controllers is more clear at lower NOx slip, and the qualitative results remain the same.

7.2.2 Controllers

P, PI, PD, and PID controllers have been tested both with and without feedforward action. There are multiple reasons to why these controllers were tested. The P controller is a simple controller that does not require much tuning. The PI controller is

a standard controller in industry, with applications in many different fields. The PD controller is interesting due to the transient nature of the application, and the PID controller is interesting since it is combines the features of the previous controllers. The controllers are not complicated to implement and are therefore good for testing a methodology. The feedforward action throughout this chapter is referring to NOx inlet measurement based feedforward, as in (7.1),

$$u^{FF}(t_k) = \text{ANR} \cdot \text{NOx}_{in}(t_k) \tag{7.1}$$

where $u^{FF}(t_k)$ is the calculated feedforward dosing in mol/m^3 at time t_k, ANR is the predetermined Ammonia-NOx-Ratio, and NOx_{in} is the inlet NOx concentration in mol/m^3. The controllers that have been tested are formulated as:

$$u(t_k) = K_c \left(e(t_k) + \frac{T_s}{T_i} \sum_{t=1}^{T} e(t_k) + D(t_k) \right) + u^{FF}(t_k) \tag{7.2}$$

where $u(t_k)$ is the dosing of NH_3 in mol/m^3 at time t_k, K_c is the proportional gain, T_i is the integral time, T is the time the cycle has been running, subscript k indicates the time instant, T_s is the sampling time, and the error $e(t_k)$ is

$$e(t_k) = r - NOx_{conversion}(t_k), \tag{7.3}$$

where r is a constant set point in NOx conversion as a fraction. $D(t_k)$ in Equation (7.4) is the derivative action given by [10]

$$D(t_k) = \frac{T_d}{T_d + NT_s} D(t_{k-1}) - \frac{T_d N}{T_d + NT_s} (e(t_k) - e(t_{k-1})) \tag{7.4}$$

where T_d is the derivative time, and N is the filtering factor. The expression in (7.2) represents all controllers that have been tested in this work. A P controller represents the scenario where $T_i \to \infty$, $T_d = 0$, and ANR = 0. A PI controller is the case where $T_d = 0$, and ANR = 0. A PD controller is when $T_i \to \infty$ and ANR = 0. A controller coupled with feedforward is the case where ANR $>$ 0, and the same parameters as previously. The sampling time T_s was 1s. The set point r was set to 100% conversion in all simulations. Having the set-point at 100% conversion means that the integral error will increase throughout the test cycle. For a road going vehicle, it would be necessary to either use a set-point that is realistic, or introduce saturation on the integrated error. It can be noted that the integral action does not include any anti-windup or saturation. Anti-windup is not necessary since the urea dosing devices are capable of dosing large amounts of urea and because the set-point is not changed. The decision to not include saturation on the integrated error is believed to be acceptable since the purpose of the controllers is to test the

methodology, and not find an optimized controller for a road going vehicle. The overall control action was limited to be minimum 0, however the individual parts were not.

In this work the feedback was based on only NOx conversion, as seen in eq.(7.3). As stated in section 7.1, a problem with NOx sensor based control is that the sensors are cross-sensitive to NH_3. This effect was not taken into consideration, and the sensors were considered to be noise-free.

It was assumed that the dosing was instant and was uniformly distributed to the inlet of the monolith. It was also assumed that the urea was decomposed instantly to NH_3. These assumptions will likely have an impact compared to the real application, where dosing delay and urea decomposition are problems [134], however it is believed that the general trends observed from the pareto fronts should be the same.

7.2.3 Experimental Setup

The experimental test conducted with the different controllers were produced using a full-scale engine, without EGR, and with a displacement of 13 liter. The used monolith was a full body vanadium based catalyst with 270 CPSI on a corrugated substrate, 8 inches long, and 13 inches in diameter. The monolith and catalyst had the same properties as the one used for parameter estimation, in Chapter 4, meaning it was simply a bigger version of it. The European Transient Cycle (ETC) [32] was used as a pre-set for the engine. The exhaust gases were not pre-treated with other catalysts before entering the SCR. The setup was placed in a room without climate control, meaning that different tests can have slightly different results, due to different ambient conditions. The measurement equipment consisted of two Horiba MEXA 7000, and one Siemens LDS 6 Diode Laser. The MEXA systems measured the NO, NOx, CO, CO_2, O_2, HC, and N_2O. The LDS measured the NH_3 in-situ. The temperature was measured at the inlet and outlet of the monolith. Both inlet and outlet data was logged at 1 Hz, which was also the sampling time used for simulation. The dosing system used to implement the controllers for the full-scale tests was a in-house built system written in LabView [93]. The dosing files were written in Matlab [94] and sent to the LabView system. The system used the NOx sensor as input and was controlling a Emitec dosing pump for urea. The urea solution was 32.5% urea diluted in water. The urea dosing was in ml/h. It should be noted that in simulation, the dosing was done directly in mol/m^3 of NH_3, due to how the model was designed. The dosing therefore had to be recalculated in the experi-

mental tests. For each controller, six different parameter sets were tested. The first test acted as conditioning of the catalyst to the following test. The most common procedure is to run each test two times, ensuring that the catalyst in conditioned according to the test. Between each experimental test, the engine was set to idle for 10 minutes, which reduced the temperature of the monolith. This was not included in the simulation.

The commercial software Matlab was used for simulation. The simulated monolith was 12.7 inches long and 9 inches diameter. The engine was a 10 liter engine without EGR. It can be noted that the simulations and experimental tests are based on different engines. The model was validated on data from a 10 liter engine, and was therefore used to generate the simulated pareto fronts. This engine was no longer available during the experimental verification, and a 13 liter engine was used instead. It does however not pose a problem since the objective is to validate the qualitative behaviour rather than the quantitative.

7.3 Results

This section will present the results where the methodology is applied to the described controllers, both during simulation and for full-scale tests. The simulation results for the individual controllers will be presented first, and a comparison between the controllers. The simulated controllers will be compared to the experimental results.

7.3.1 Simulation

7.3.1.1 P Controller

The P controller has one free parameter, the gain K_c. Figure 7.2 shows the pareto fronts for P controllers with varying degrees of feedforward, ranging from ANR = 0 to ANR = 1.5. The parameters used for simulation were in the range $0 \leq K_c \leq 1.0$. It can be seen that the controller with ANR = 0 starts to increase in average NH_3 slip rapidly after the NOx slip goes below 3 g/kWh. The EURO IV emission limited the NOx slip to 3.5 g/kWh, and it appears that a P controller was enough to meet the previous emission limits, at least with the assumptions included in this work. As the feedforward is increased it can be seen that the pareto front is shifted inwards, giving a better trade-off between NOx and NH_3. When ANR > 1, meaning that more moles of NH_3 (or urea) is dosed from the feedforward action than there is NOx in the monolith inlet, the pareto fronts are shifted upwards, and the feedforward that

should be used depends on the desired NOx slip. As an example it can be seen that the P controllers with ANR = 1.3 and ANR = 1.4 overlap.

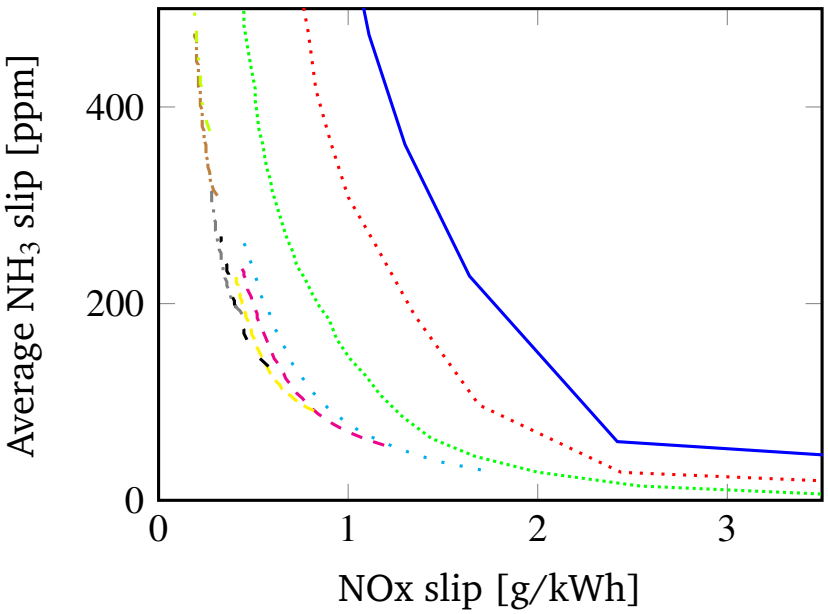

Figure 7.2. Pareto fronts for simulated P controllers with the ETC, with different levels of ANR feedforward. Legend: ANR = 0 (——), ANR = 0.2 (.....), ANR = 0.5 (.....), ANR = 0.8 (. . . .), ANR = 0.9 (- - -), ANR = 1.0 (- - - -), ANR = 1.1 (- - -), ANR = 1.2 (- . - .), ANR = 1.4 (- . - .), ANR = 1.5 (- . -)

7.3.1.2 PI Controller

The PI controller has two free parameters, the gain K_c and the integral time T_i. Figure 7.3 shows the influence of the integral time for a PI controller without any feedforward. The K_c parameter used for simulation was in the range $0 \leq K_c \leq 0.01$. As seen, the difference in the cycle based performance for different T_i is small. The transient nature of the ETC ensures that the process is never in steady state, and it makes little difference if the integral action is acting towards a hypothetical steady state in 60s or 70s. Figure 7.4 shows the pareto fronts for a PI controller with ANR = 0, and ANR = 0.9-1.2. It can be seen that as with the P controller, introducing feedforward improves performance. The overlap between controllers when the feedforward is increased is more prominent with the PI controller than with the P controller. Generally it seems better to increase the K_c parameter up to a certain level, instead of increasing the feedforward. The reason for this is

unknown. When the feedback become too strong, increasing the feedforward is better for the NOx-NH_3 trade-off. The trade-off curves become increasingly steep as feedforward is increased, which is also seen with the P controller. This is likely because of fundamental limits of the control structure, and the NOx slip can not become smaller than a certain limit. At ANR = 1.2 and beyond, increasing the feedback only gives an increase in NH_3 slip, while not reducing the NOx slip.

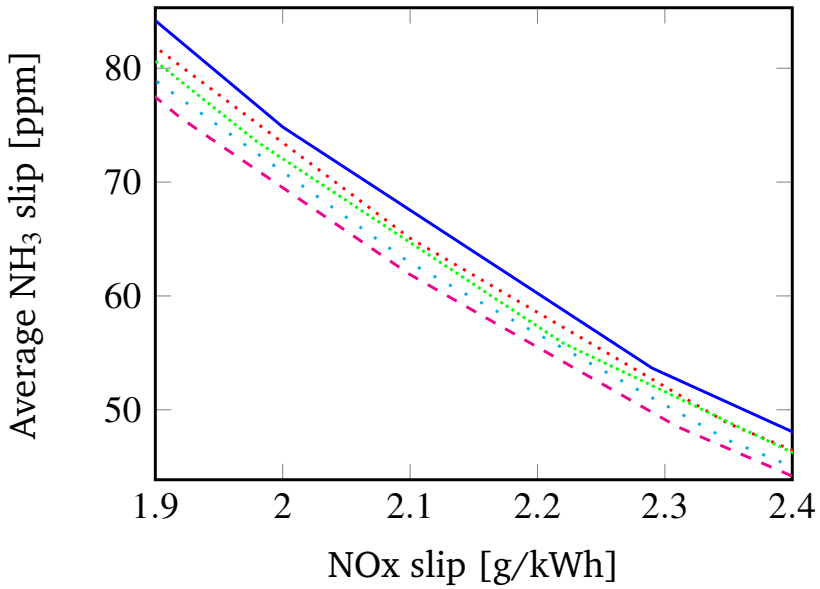

Figure 7.3. Pareto fronts for simulated PI controllers with the ETC, with different integral times. Legend: $T_i = 40$ (——), $T_i = 50$ (·····), $T_i = 60$ (·····), $T_i = 70$ (· · · ·), $T_i = 80$ (- - -)

7.3.1.3 PD Controller

The PD controller has three free parameters, the gain K_c, the derivative time T_d, and the filtering factor N. Figure 7.5 shows several pareto fronts with different T_d and N parameters. The K_c parameter used for simulation was in the range $0 \leq K_c \leq 0.05$. As can be seen the curves have a non-smooth shape and for a given T_d and N, two different K_c can give the same NH_3 slip and different NOx slip. [10] state that the N parameter normally takes values between 8 and 20, which has been adopted here. The derivative time has also been tested in a broad range, with limited success. The PD controller performs worse than P controllers that were shown in Figure 7.2. To investigate if the reason for the erratic shape was a too strong derivative action, the gain was held constant while increasing the derivative time, in Figure 7.6.

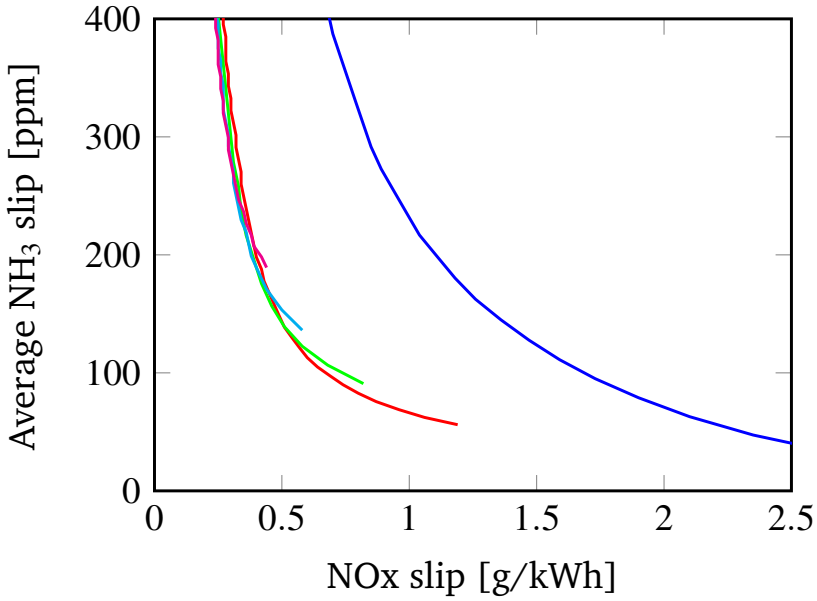

Figure 7.4. Pareto fronts for simulated PI controllers with the ETC, with different levels of ANR feed forward. The integral time for all simulation was $T_i = 70$. Legend: ANR = 0 (——), ANR = 0.9 (——), ANR = 1.0 (——), ANR = 1.1 (——), ANR = 1.2 (——)

It can be seen that even for low derivative times, the trade-off curve became irregular and no smooth shape was obtained. The reasons for this behaviour is not fully known, however it is suspected that even though the signal was considered noise free, the transient input resulted in a rapidly changing error, that the derivative action was too sensitive to. The fact that the results showed cases where the controller gave the same NH_3 slip for different NOx-slip, suggests there are periods where one parameter set results in a large NH_3 slip at a certain time, while the other parameter set does not.

Because of these results and the fact that the PD controller performed worse than a P controller even for good parameters, it was decided to investigate the properties of the closed-loop system. The isolated feedback system can be described by Figure 7.7, where y is the NOx conversion, r is the reference in NOx conversion, e is the error in NOx conversion, u is the dosed NH_3, the box C is the controller, P is the process dynamics, and D is the disturbance dynamics. From the figure is can be derived that:

$$Y(s) = \frac{1}{1 + G_C(s)G_P(s)} Z(s) + \frac{G_C(s)G_P(s)}{1 + G_C(s)G_P(s)} R(s) \tag{7.5}$$

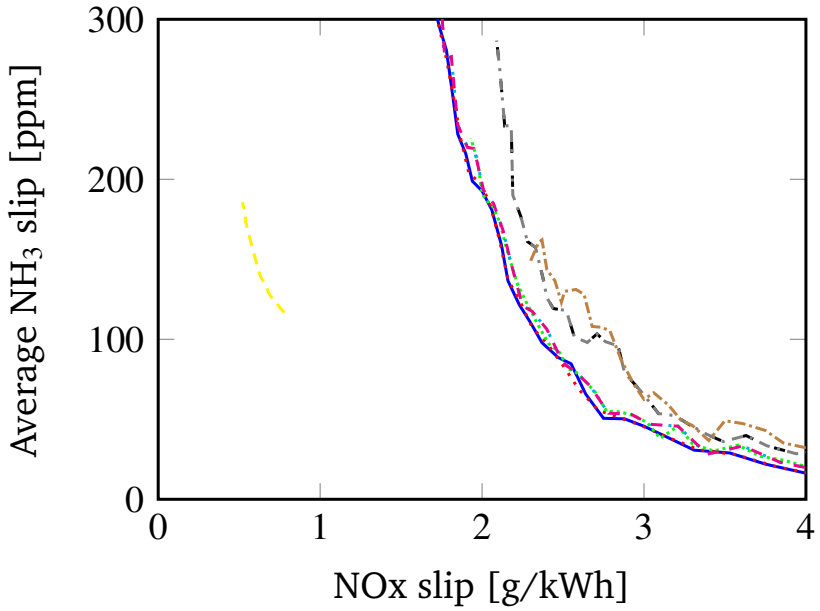

Figure 7.5. Simulated PD controllers with the ETC, with different T_d and N. Legend: $T_d = 0.5$, $N = 15$ (——), $T_d = 0.5$, $N = 20$ (.....), $T_d = 1$, $N = 10$ (.....), $T_d = 1$, $N = 15$ (. . . .), $T_d = 10$, $N = 10$ (- - -), $T_d = 10$, $N = 20$ (- - -), $T_d = 12$, $N = 20$ (-.-.-), $T_d = 15$, $N = 15$ (-.-.-), $T_d = 1$, $N = 15$, ANR = 1.0 (- - -)

where s is the complex number frequency parameter from the Laplace transform, $G_C(s)$ is the transfer function for the controller, $G_P(s)$ is the transfer function for the process, and $Z(s)$ is the combined contribution of the disturbances. If $R(s) = 0$ the transfer function for the closed-loop disturbance behaviour is achieved:

$$G_Z(s) = \frac{Y(s)}{Z(s)} = \frac{1}{1 + G_C(s)G_P(s)} \tag{7.6}$$

and if $Z(s) = 0$, the transfer function for the closed-loop command behaviour is achieved:

$$G_R(s) = \frac{Y(s)}{R(s)} = \frac{G_C(s)G_P(s)}{1 + G_C(s)G_P(s)} \tag{7.7}$$

Since the reference in this study is constant, Equation (7.7) is of no interest for the stability of the system. Equation (7.6) is however of importance for the system. To analyse the properties of the closed-loop disturbance behaviour, models $G_C(s)$ and $G_P(s)$ are required. The models for the disturbances are not needed, since assuming that stable models are used, the only thing that can introduce instability is feedback. The model for the controller is the implemented PD controller, and

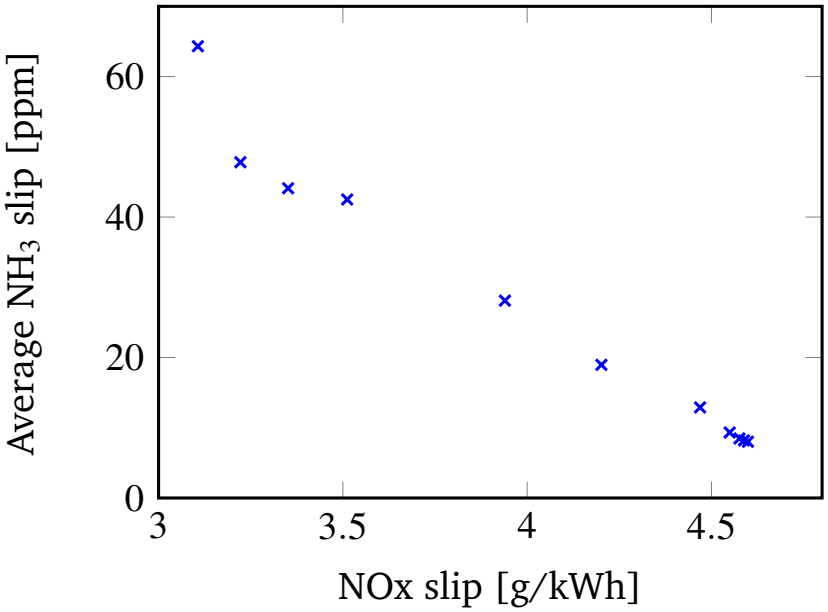

Figure 7.6. Behaviour for PD controllers when the gain K_c is kept constant and the derivative time T_d is increased. $K_c = 0.01$ and $T_d = 0.1 : 8$ Legend: PD controller (×)

using the parameter values $T_d = 1$, $N = 10$, $K_c = 0.01$:

$$G_C(s) = -K_c\left(1 + \frac{sT_d}{1 + sT_d/N}\right) = \frac{-0.11s - 0.1}{s + 10} \tag{7.8}$$

The process model was created using the system identification toolbox in Matlab. The same open-loop data that was used for validation in Chapter 5 was used to fit the parameters. Several different order models were tried, and the best fit to data was achieved with a 2-pole-2-zero model:

$$G_P(s) = \frac{13.9s^2 + 5.655s + 0.04339}{s^2 + 0.4009s + 0.0007181} \tag{7.9}$$

The poles of $G_C(s)$ and $G_P(s)$ are negative, however if Equations (7.8) and (7.9) are inserted in Equation (7.6), the poles of the system are:

$$s_1 = 16.26$$
$$s_2 = -0.40$$
$$s_3 = -0.0008$$

The fact that the system has positive poles indicates that the system might be unstable. The process model used here is not as good a representation of the dynamics

as model 2 that was used to create the pareto fronts, however it indicates that it is not necessarily a well defined control problem.

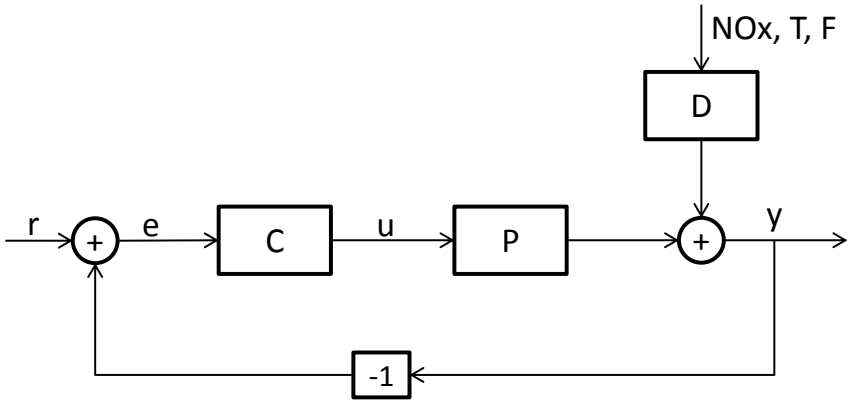

Figure 7.7. Overview of the feedback system.

7.3.1.4 PID Controller

The PID controller has four free parameters, the gain K_c, the integral time T_i, the derivative time T_d, and the filtering factor N. T_i was chosen as the value that showed the best performance during PI analysis in Section 7.3.1.2, and T_d and N were chosen based on performance in PD analysis in section 7.3.1.3. The K_c parameter used for simulation was in the range $0 \leq K_c \leq 0.02$. Figure 7.8 shows pareto fronts for PID controllers with ANR = 0, and ANR = 0.7-1.1. It can be seen that the negative effect of derivative action seems to have disappeared. The performance is, as with the P and PI controller, improved when feedforward is included. The overlap seen previously when feedforward is increased is also seen here.

The same analysis of the closed-loop system that was carried out for the PD controller was carried out here as well. The results however showed that Equation (7.6) had a positive pole for the PID controller as well. The analysis naturally depends heavily on the process model, which is a big uncertainty in the analysis. To investigate further why the PD controller exhibits unexpected behaviour and the PID does not, the contribution of each of the control parts was analysed for a specific controller for the PD and PID controllers. Figure 7.9 shows the contributions of each part of the controller for a PD and PID controller without feedforward. For the PD controller, the derivative part takes values both positive and negative. This is due to the form in Equation (7.4). If the current NOx conversion is higher than the previous, and the previous derivative action was low, it is possible to achieve

negative action. The overall control action was set to be minimum 0, however the individual parts were not. If the PD controller is compared to the PID controller, it can be seen that, as expected, the integral action becomes larger throughout the test, since the set point was 100% conversion. The integral action is dominant in the later stages of the test, and since the derivative part has little influence, this can explain why the PID controller seems to function well, and the PD does not.

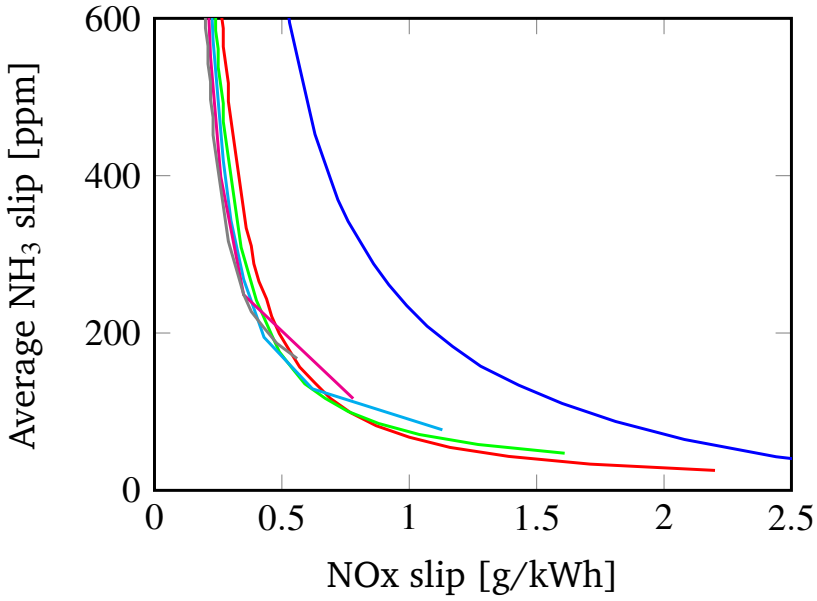

Figure 7.8. Simulated PID controllers with the ETC, with different levels of ANR feed forward. Legend: ANR = 0 (——), ANR = 0.7 (——), ANR = 0.8 (——), ANR = 0.9 (——), ANR = 1.0 (——), ANR = 1.1 (——)

7.3.1.5 Comparison of Simulated Controllers

Figure 7.10 compares some of the previous results. The best controller tested was the PI with feedforward ANR = 1.0. This controller outperformed the P controller with feedforward, meaning that the integral action increased performance when combined with feedforward as well. The difference between a P controller and a PI controller was however substantially bigger without feedforward. The reason integral action improves performance even though no steady state is reached is because it ensures that there is continous dosing, even during periods of low error. The effect of feedforward was dominating, and as can be seen, a P controller with feedforward outperformed a PI controller without feedforward. The difference be-

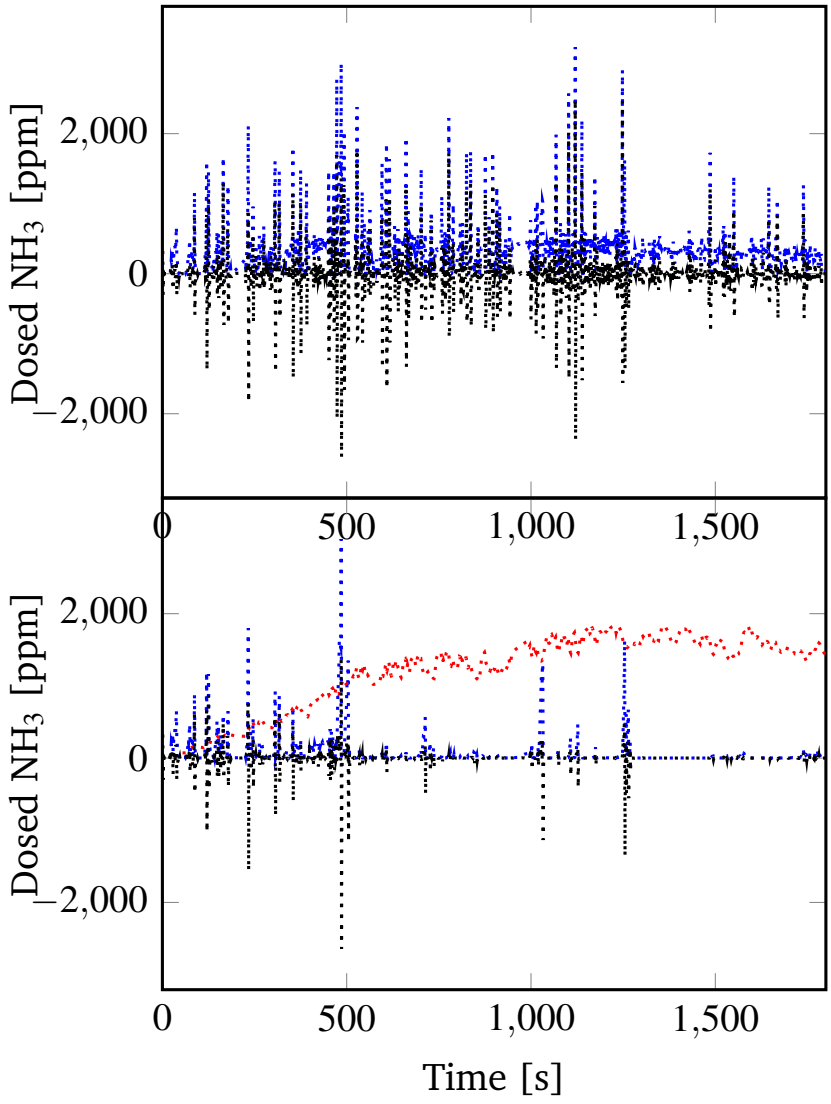

Figure 7.9. Comparison of the different control contributions for a specific PD (top) and PID (bottom) controller. Legend: Proportional action (.....), Integral action (.....), Derivative action (.....)

tween a PI controller and PID controller without feedforward is difficult to see in Figure 7.10. However if zoomed, it can be seen that the PI controller was slightly better than the PID controller. This confirms that the derivative action has little or no effect at the expense of added complexity, also combined with the integral action. Figure 7.10 shows that controllers including both feedback and feedforward performed better than controllers with only feedforward. This shows that even

though the feedforward was dominating, the feedback control action contributes to the cycle based performance.

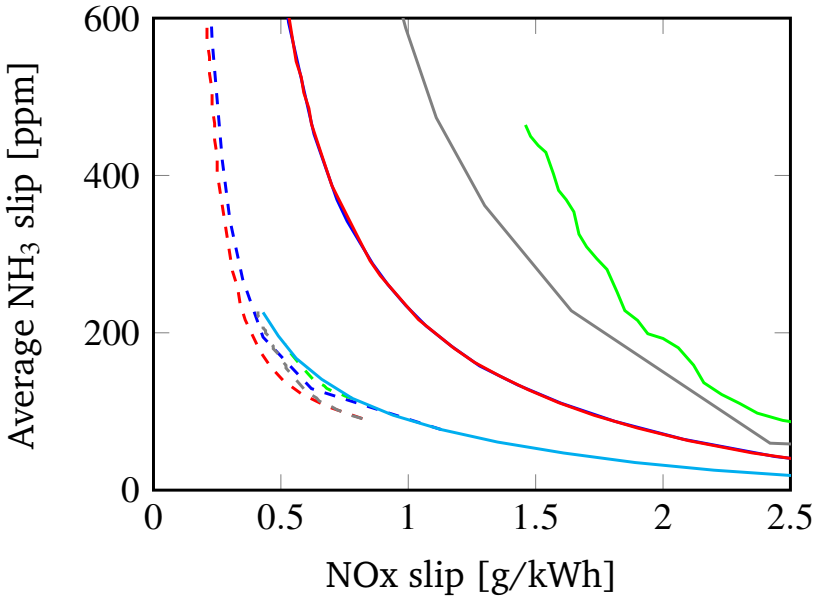

Figure 7.10. Simulated PID controllers with the ETC, with different levels of ANR feed forward. Legend: P (——), P with ANR = 1 (- - -), PI (——), PI with ANR = 1.0 (- - -), PD (——), PD with ANR = 1.0 (- - -), PID (——), PID with ANR = 1.0 (- - -), ANR = 0:1.0 (——)

7.3.2 Experimental Verification

This section will present the experimental results where a small selection of the simulated controllers was tested with a full-scale setup. The feedfoward ANR was in all cases set to ANR = 0.9, except for the controller with only feedforward.

7.3.2.1 ANR Feed Forward

Figure 7.11 shows a comparison between the simulated ANR based feedforward controller with ANR = {0.6:1.4} with step length 0.05, and experimental data for ANR = {0.7, 0.8, 0.9, 1.0, 1.1, 1.2}. There deviation between data and model is small. It is slightly higher for higher ANR values than for the lower values. This is expected, since the model has been calibrated and validated for operating conditions that are close to Euro IV emission limits. The experimental pareto front has the same curving shape as the simulated controllers. It can be noted that the figure does

not show the exact placement of the simulated ANR = {0.7,0.8,0.9,1.0,1.1,1.2} controllers. This is because it is expected to have a deviation between the model and the experimental data for a controller with identical parameters. The difference is due to both on the fact that the simulation was based on a 10 liter engine and the experimental tests with a 13 liter engine, and that the catalysts were of slightly different size. This does however not invalidate the methodology, as the purpose is to investigate the trade-off curve, rather than the exact performance of a specific controller. When a controller that has been developed through simulation is implemented, it will likely require fine tuning of the parameters.

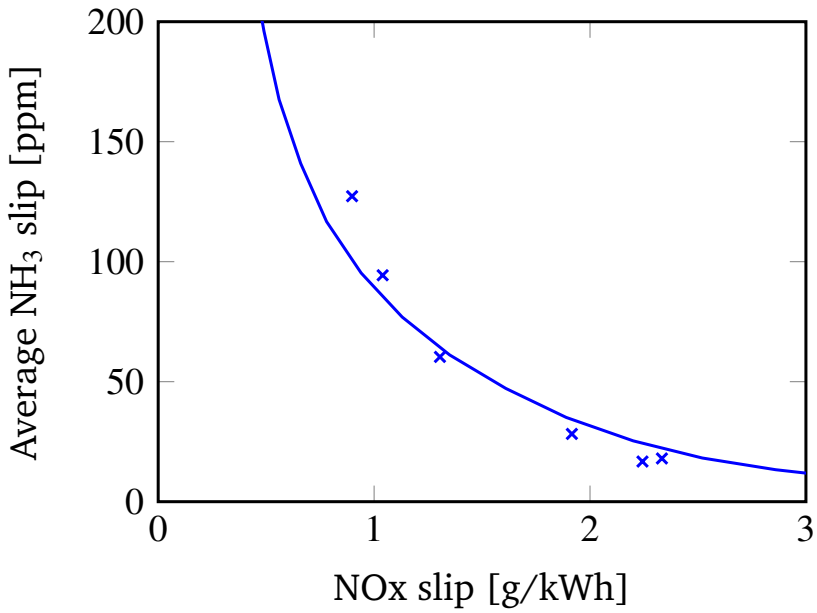

Figure 7.11. Simulated ANR based feedforward controllers with the ETC, compared with experimental data. Legend: Model ANR = {0.6:1.4}(——), Data ANR = {0.7, 0.8, 0.9, 1.0, 1.1, 1.2} (×)

7.3.2.2 P Controllers

Figure 7.12 shows a comparison between the simulated P controllers with ANR = {0,0.9}, and the experimental data for the same controllers. The parameters for the experimental tests were, without feedforward:

$K_c = \{0.025, 0.03, 0.035, 0.040, 0.045, 0.05\}$

and with feedforward:

$K_c = \{0.0018, 0.0054, 0.009, 0.0126, 0.0162, 0.0197\}$.

It can be seen that for the controllers without feedforward, the experimental tests perform better than the simulated controllers. The pareto front is located closer to the desired bottom left corner than the simulated controllers. The experimental pareto front has a more linear trend than what can be seen for the simulated pareto front. In general the simulated pareto fronts have an increasing slope with a more aggressive controller, and is close to linear, in the chosen parameter interval, for high NOx conversions. The reason for the linear experimental pareto front can therefore be that the curving section has already been passed for the chosen parameters. It is also possible that a larger span of parameters is needed to see the curving in the experimental tests, as the curvature can appear close to linear, even for the simulated pareto fronts, for smaller intervals of K_c.

To gain insight into why there is a difference between the case when ANR = 0, the error that the dosing system was acting on in Equation (7.3) in the test is plotted for the same controller, both for simulation and experimental values, in Figure 7.13. The top of the figure shows the error during simulation, and the bottom shows the error in the experimental test. It can be seen that the error is changing significantly more rapidly when the model is used compared to the experimental setup. The two first sections of the ETC shows a greatly varying error for both the model and experiment, however in the last section, which is less transient, the model has an average error of around 0.3 and the experimental controller achieves an almost zero error. If the average error is taken for both tests for the first 1200 s, the average error is 0.24 for the model and 0.20 for the experiment. For the entire test the average error is 0.25 for the model and 0.16 for the experiment. The majority of the difference between the two cases can therefore be traced to the last section. The main difference between the two errors appears to be that the model error contains more high frequency components. Figure 7.14 shows the frequency components for the error series for both the model and the experimental data, up to the Nyquist frequency of 0.5 Hz. The figure confirms that the higher frequency components are generally larger for the model than the error. The model has a significant contribution up to around 0.2 Hz, until it starts decreasing. The data has a high contribution up to 0.1 Hz, and is low at higher frequencies. To investigate if a closer match between the model and data error was possible if the high frequencies of the model were removed, low pass Butterworth filters were developed and applied to the model error. The low pass filter has the form:

$$H(s) = \frac{B(s)}{A(s)} = \frac{b(1)s^n + b(2)s^{n-1} + ... + b(n+1)}{a(1)s^n + a(2)s^{n-1} + ... + a(n+1)} \tag{7.10}$$

where a are the coefficients for the numerator, b are the coefficients for the denominator, and n is the order of the filter. a and b contains $n+1$ parameters. First, second, and third order filters were tested. A higher order low pass filter generally means that it has a more direct cut-off after the cut-off frequency. Based on the frequency component analysis in Figure 7.14, the cut-off frequency was chosen as 0.1 Hz. It was attempted to optimise the best cut-off frequency for different filter orders, with a least-squares optimisation problem. The results however showed that the filters became too aggressive, and certain parts of the data set contributed significantly to the objective function, resulting in a filter that appeared closer to the average of the error. It was therefore decided to use 0.1 Hz as the cut-off frequency, which provided a good trade-off between keeping the model dynamics and a better fit to data. The coefficients for the filters can be seen in Table 7.1. Figure 7.15 shows a comparison between the experimental error of the investigated P controller, and when the model error has been filtered with a first, second, and third order filter. The model error is significantly closer to the experimental error. The main difference between the different orders of the filter can be seen between 400 to 500 s and 1000 to 1200 s, where the higher order filters produces a signal closer to the model signal. At periods where the model has zero error, such as between 900 to 1000 s, and 1300 to 1800 s, there still exists a large difference between the model and experiment. The results shows that the experimental sensor or monolith includes frequency dampening properties that the model cannot predict, at least when a feedback controller is used. If the model should be used to test controllers, the output should therefore be filtered as shown here.

For the controllers with ANR = 0.9, the agreement between the simulated and experimental pareto fronts is better. The experimental controllers perform slightly worse than the simulated controllers. It can be noted that the first data points has a slightly higher NH_3 slip than the second data point, which has a more aggressive controller. This is however due to the catalyst being conditioned in a incorrect way in the first test. It can be seen that the difference between the controllers with ANR = 0 and ANR = 0.9 is substantially lower for the experimental pareto fronts than for the simulated.

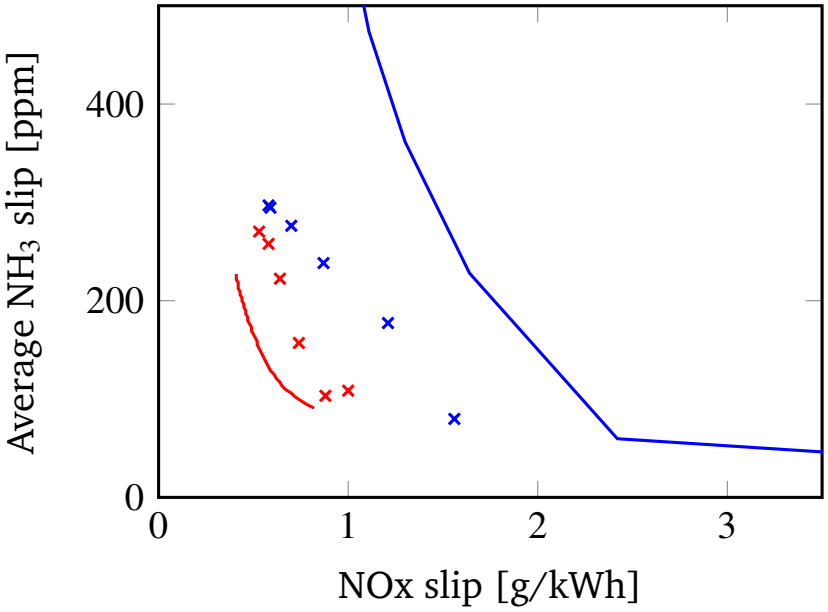

Figure 7.12. Simulated P controllers with the ETC, compared with experimental data. Legend: Model ANR = 0 (——), Model ANR = 0.9 (——), Data ANR = 0 (×), Data ANR = 0.9 (×)

Table 7.1. Coefficients for the low pass filters.

Parameter	$n = 1$	$n = 2$	$n = 3$
a_1	1.0	1.0	1.0
a_2	−0.5095	−1.1430	−1.760
a_3	–	0.4128	1.1829
a_4	–	–	−0.2781
b_1	0.2452	0.0675	0.0181
b_2	0.2452	0.1349	0.0543
b_3	–	0.4128	0.0543
b_4	–	–	0.0181

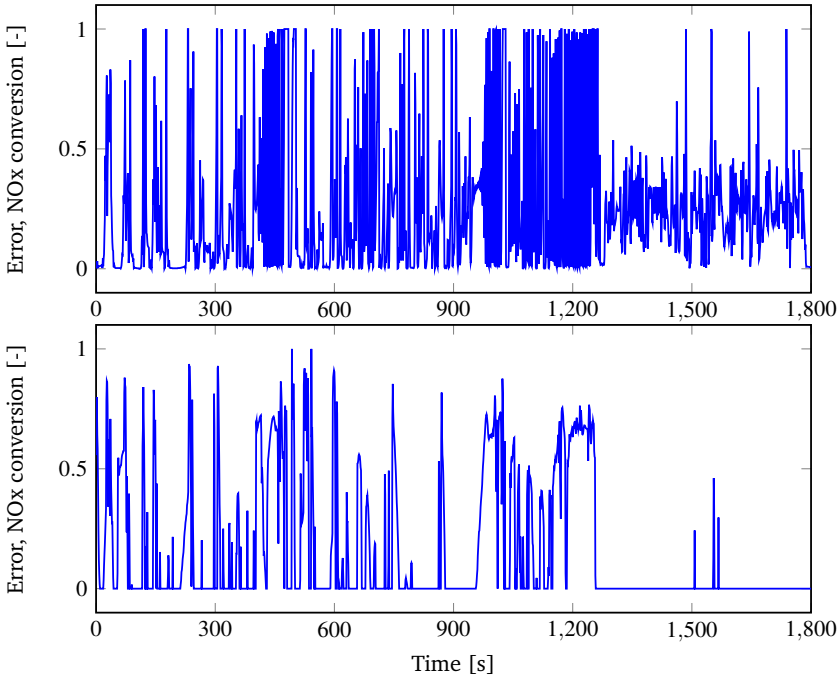

Figure 7.13. Comparison of the error used to calculate urea dosing for the P controller, with model (top) and experimental (bottom). Legend: Error (——)

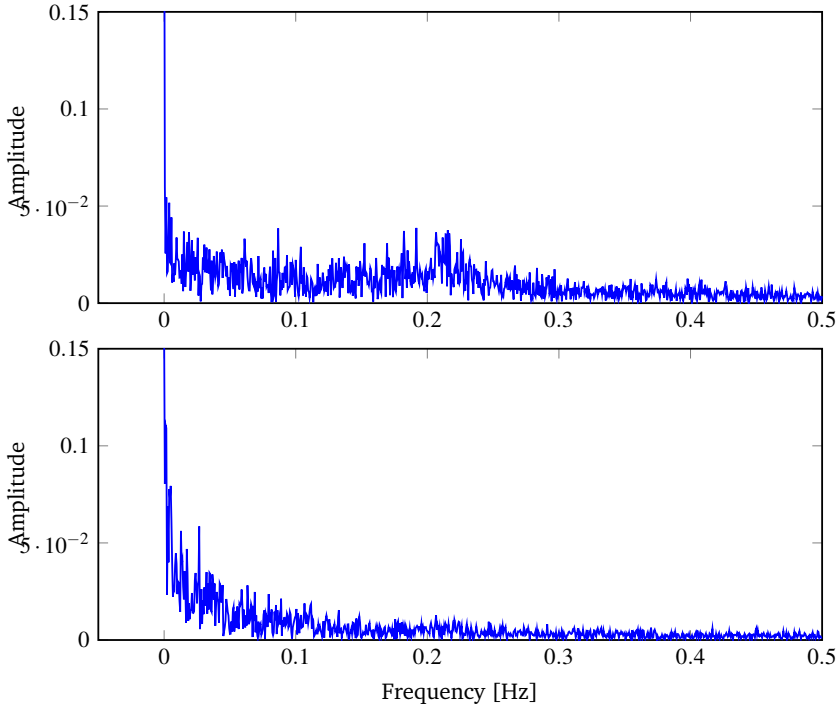

Figure 7.14. Frequency components for the error used to calculate urea dosing for the P controller, with model (top) and experimental (bottom). Legend: Amplitude (——)

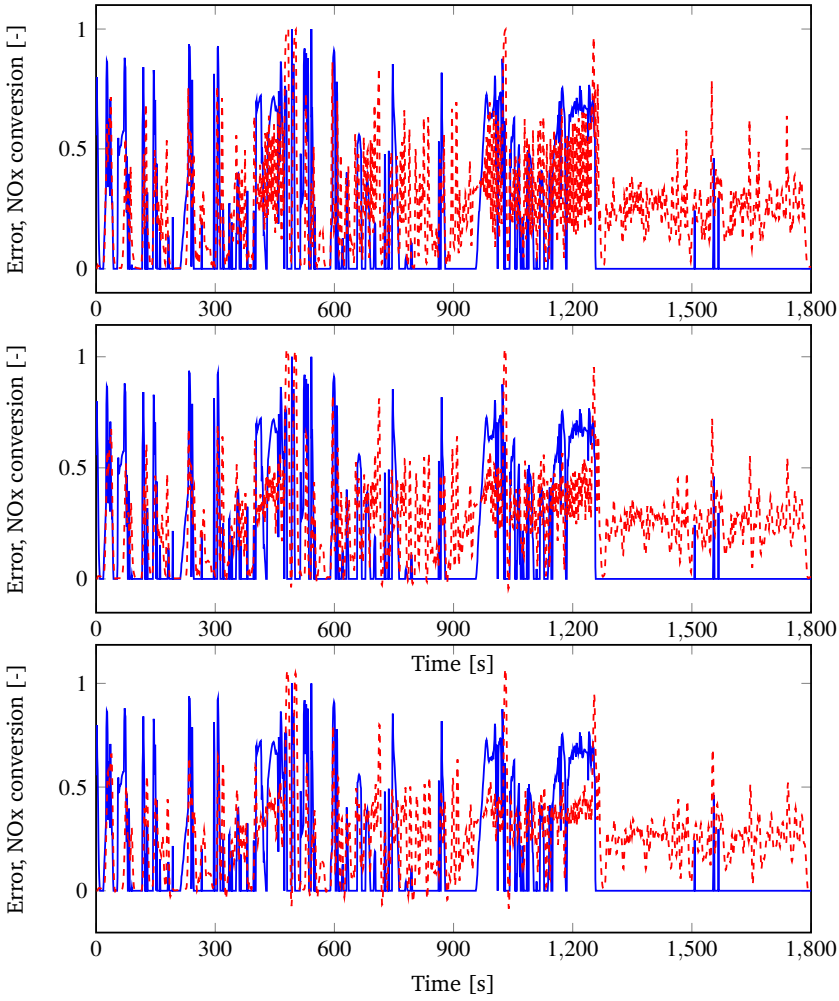

Figure 7.15. Comparison of the error used to calculate urea dosing for the P controller, with experimental and filtered model, for 1st order filter (top), 2nd order filter (middle), 3rd order filter (bottom). Legend: Experimental error (——), Filtered model error (- - -)

7.3.2.3 PI Controllers

Figure 7.16 shows a comparison between the simulated PI controllers with ANR = {0,0.9}, and the experimental data for the same controllers. The parameters for the experimental tests were, without feedforward:
$K_c = \{0.0022, 0.0025, 0.0029, 0.0032, 0.0036, 0.0039\}$
and with feedforward:
$K_c = \{0.0001, 0.0002, 0.0003, 0.0004, 0.0005, 0.0006\}$.
The integral gain was taken as $T_i = 70$ for both the simulated and experimental controllers. The results shows that the experimental pareto front for ANR = 0 has a unexpected shape, where an increase in K_c can result in a significant decrease in NOx slip, but a similar NH_3 slip. This occurs both in the beginning of the pareto front and the end, while in the middle a clear decrease in NOx slip gives a clear increase in NH_3 slip. If the first data point is assumed to be invalid due to catalyst conditioning, the shape of the pareto front has an opposite trend compared to the simulated pareto front, where an increase in K_c gives a lower increase in NH_3 slip for each incremental K_c increase. This would only be valid up to a certain point, where monolith limitations would result in a very high increase in NH_3 slip for a small decrease in NOx slip. If the last data point is assumed invalid, the trend appears correct. The results for ANR = 0 are however in reasonable agreement to the simulated pareto front.

For the case with ANR = 0.9, it can be seen that the model again has over predicted the performance slightly, since the simulated pareto front is closer to the bottom left corner. The difference is however minor, and the model has captured the trend quite well.

7.3.2.4 PD Controllers

Figure 7.17 shows a comparison between the simulated PD controllers with ANR = {0,0.9}, and the experimental data for the same controllers. The parameters for the experimental tests were, without feedforward:
$K_c = \{0.0082564, 0.008974, 0.009692, 0.01041, 0.011128, 0.01184615\}$
and with feedforward:
$K_c = \{0.0005, 0.0015, 0.0026, 0.0036, 0.0046, 0.0056\}$.
The derivative gain was taken as $T_d = 1$ and the filtering factor $N = 15$. The PD controller with ANR = 0 is the case where the model differs the most from the experimental data. The pareto front for the experimental controllers have a better trade-off than the simulated controllers. During simulation, the PD controller

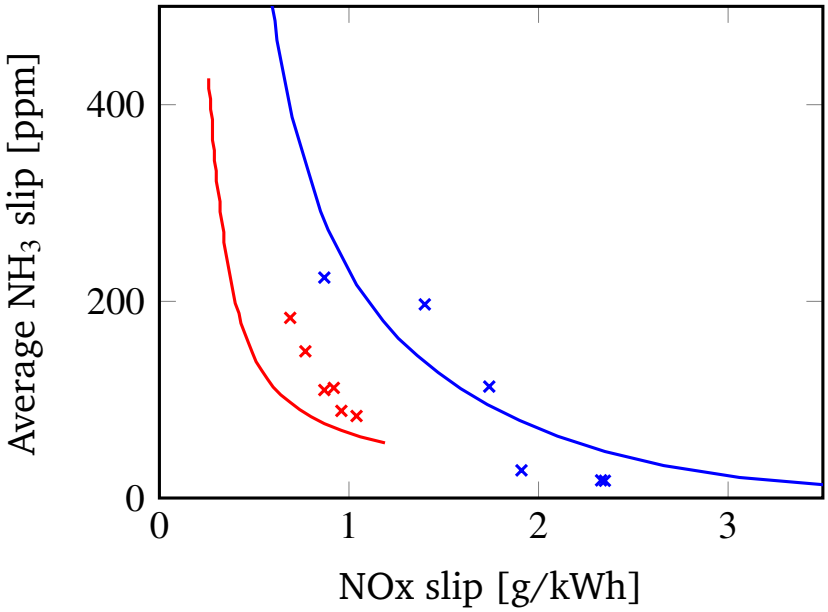

Figure 7.16. Simulated PI controllers with the ETC, compared with experimental data. Legend: Model ANR = 0 (——), Model ANR = 0.9 (——), Data ANR = 0 (×), Data ANR = 0.9 (×)

showed an erratic shape and was the controller that performed the worst, as presented in Section 7.3.1.3. Since the controller shows substantially better performance in experimental results it can be concluded that the model is not able to predict this scenario well. For the case when ANR = 0.9, it can be seen that the trend is very similar for the simulated and experimental controllers. The experimental pareto front lies slightly below the simulated pareto front, however as previously explained, the exact values are not of interest for this work, only that the NOx-NH_3 trade-off can be accurately described, which is the case here. Both experimental pareto fronts has logical trends with no outliers, as was the case for the PI controller in Section 7.3.2.3.

7.3.2.5 PID Controllers

Figure 7.18 shows a comparison between the simulated PID controllers with ANR = {0,0.9}, and the experimental data for the same controllers. The parameters for the experimental tests were, without feedforward:
$K_c = \{0.0021, 0.0026, 0.0031, 0.0036, 0.0041, 0.0046\}$
and with feedforward:

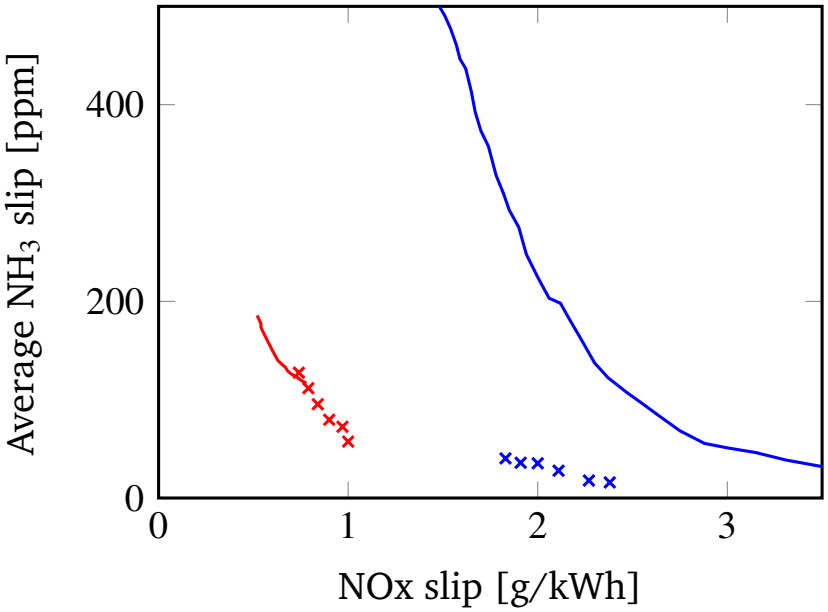

Figure 7.17. Simulated PD controllers with the ETC, compared with experimental data. Legend: Model ANR = 0 (——), Model ANR = 0.9 (——), Data ANR = 0 (×), Data ANR = 0.9 (×)

$K_c = \{0.000433, 0.000867, 0.0013, 0.0017, 0.0022, 0.0026\}$.
The T_i, T_d, and N parameters were taken as the ones for the PI and PD controllers. As with the other controllers, the case when ANR = 0 is when the model differs most from experimental data. The deviation is however not as big as in the P controller and PD controller case. One data point is different from the general trend. The reason for this is not obvious, since it is in the middle of the range, meaning it is not due to catalyst conditioning. The experimental data for ANR = 0 shows that the controller performs better in the experimental setup than when the model is used.

For the case when ANR = 0.9, the difference between model and data is smaller, as was the case for the other controllers as well. For low feedback levels it can be seen that the controller with feedforward performs better than the pure feedback controller. When the feedback action is increased, the difference is however decreasing, and in the end the PID controllers with ANR = 0 and ANR = 0.9 performs equally well. As in the case with the previous controllers, the performance of the controller with ANR = 0.9, is slightly overestimated. In general the difference is however not significant.

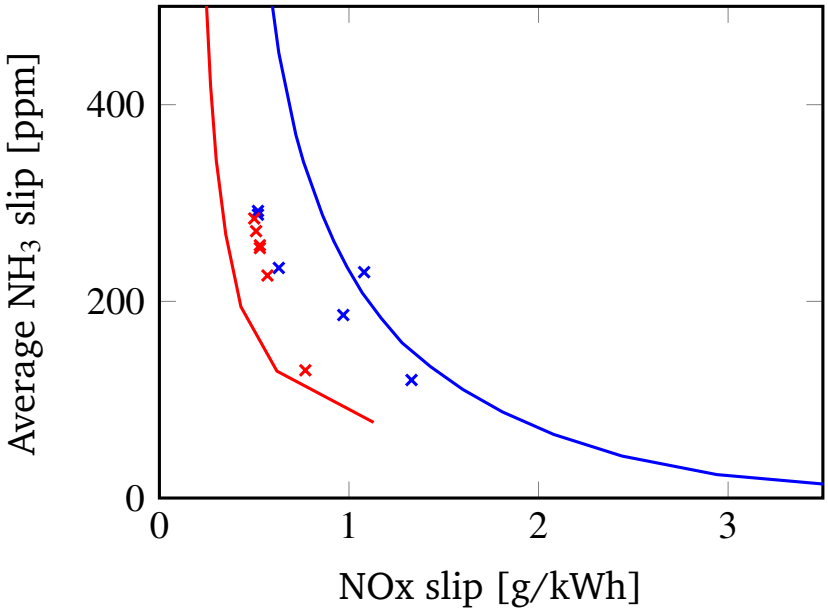

Figure 7.18. Simulated PID controllers with the ETC, compared with experimental data. Legend: Model ANR = 0 (——), Model ANR = 0.9 (——), Data ANR = 0 (×), Data ANR = 0.9 (×)

7.3.2.6 Comparison

Figure 7.19 shows a comparison between all the experimentally tested controllers, both with and without feedforward (ANR = 0.9). It can be seen that the controller that performed the best of all the tested controllers was the PD controller with ANR = 0.9. This is not in agreement with simulation results, where the PI controller with feedforward was the best performing controller. The difference between the PI and PD controllers with feedforward is however quite small. In the simulation results the PD controller was the worst performing controller out of the ones that included feedforward. It can be seen that the difference between the PI and P controllers with feedforward is small, however at low feedback action, the PI controller appears to be the best. Since the model has had difficulties predicting the performance of the PD controller, if it had not been included in the experimental tests, the PI with feedforward would have been the best performing controller both in simulation and experimental tests. It can be noted that all controllers that includes both feedback and feedforward performed better than the pure feedforward controller, which is something that was the case in simulation as well.

For the controllers without feedforward (ANR = 0), the controller that performs

best appears to be the PID controller. A direct comparison is difficult, since some of the controllers have unusual trends in their pareto front. For example the PI controller has several data points that are significantly worse than the rest, however some of them performs on the same level as the P controller. The parameters that were chosen for the PD controller has not been optimal for comparison since the pareto front is too far away from the rest. Any conclusions about the performance of the PD controller in relation to the other controllers is therefore difficult to make. The conclusions drawn from simulation regarding the PID controller is however correct since it was both the best performing controller without feedforward in data and simulation (together with the PI controller).

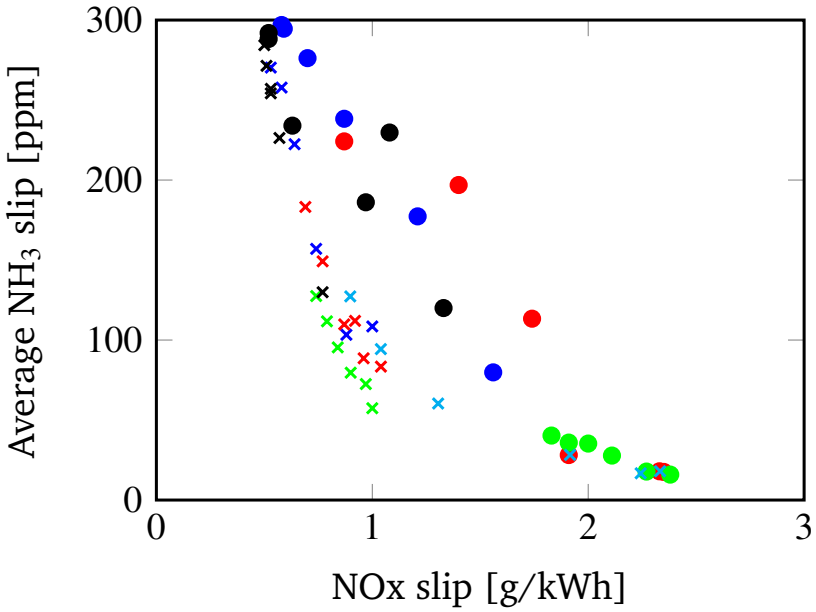

Figure 7.19. Comparison between experimental data for P, PI, PD, PID, and feed forward controllers. Legend: P ANR = 0 (●), P ANR = 0.9 (×), PI ANR = 0 (●), PI ANR = 0.9 (×), PD ANR = 0 (●), PD ANR = 0.9 (×), PID ANR = 0 (●), PID ANR = 0.9 (×), ANR feed forward (×)

7.4 Discussion

The presented methodology provides a way to compare controllers graphically in their whole operational span. Although it has only been applied to P, PI, PD, and PID controllers with feedforward in this work, it can easily be applied to other controllers as well, for example model based controllers, controllers based on NH_3, etc.

For a controller that requires an optimisation problem to be solved, it can be suitable if the user is uncertain about the weights that should be used in the objective function. If the objective function weights are changed and the solutions presented using pareto fronts, the pareto fronts will give an overview of which weights corresponds to the desired controller performance. Due to the large number of parameters that has to be tested to generate the pareto fronts, the methodology would become resource intensive if it was applied experimentally directly. It is thus more suitable for comparing controllers through simulation. The controllers and shape of the pareto fronts can be validated experimentally with a smaller number of experiments, to confirm that the same results can be achieved when dosing delay, cross sensitivity to NH_3, and other factors are considered, that are complicated to include in a model.

From the experimental validation carried out in this work it is clear that some conclusions were valid from the simulation results, and some were not. The main problem was the problems the model had to predict the global cycle wide NOx and NH_3 slip. A reason for this can be the way the model has been calibrated, and how feedback operates. As discussed in Chapters 4 and 5, it is possible that the lack of proper NH_3 adsorption and desorption data has affected the quality of the coverage prediction. A model that should predict the effects of a feedback controller has to be able to correctly predict the dynamics of a longer time-span, compared to a feedforward controller, since feedback controllers act on the current error at the outlet of the system. The feedforward controllers on the other hand does not, to the same extent, depend on the slow dynamics of the system, since the controllers are acting directly on the disturbances on the system. Another possible explanation to why the model is more successful in predicting the effects of feedforward controllers is that the model has been calibrated and validated with feedforward based data. To investigate the differences between some of the results between simulation and experiments, several different analyses were conducted. The low-pass filtration of the error conducted for the P controller showed that it was possible to achieve a model error that is closer to the experimental error. The results suggests that the model does not include certain frequency filtering properties that the experimental system does. The low-pass properties can be a results of either, or both, the monolith and the sensors used to measure the monolith inlet and outlet concentrations. The accuracy of the methodology depends on the accuracy of the model, and with the model used here the major conclusions were transferable from the model simulations, and the methodology therefore has use in practice. Due to the model mismatch the simulation wrongly indicated that the PD controller was unsuitable for the application.

The experimental tests however showed that the PD controller is suitable, and performs similarly to the PI controller. The PD controller is suspected to be successful due to the transient application.

In this work the pareto fronts have been based on entire-cycle based performance by measuring the average NH_3 slip and total NOx slip. The current legislation includes rules about the total NOx slip, the average NH_3 slip over the entire cycle, and the maximum NH_3 peak at any given time. The pareto fronts can be modified to represent the maximum peak slip, or expanded so that all three legislative limits are covered.

The results shown here are general in the sense that changes in catalyst volume or other system parameters would shift the position of the pareto fronts, but will not change the conclusion on the rankings of controllers in relation to performance. This is confirmed in Figure 7.20, where the pareto fronts for the P and PI controllers are plotted for two different volumes. As expected, the larger volume improves the trade-off between NOx slip and NH_3 slip, since more catalyst is available for reaction. The conclusions are still valid as the PI controller performs better than the P controller.

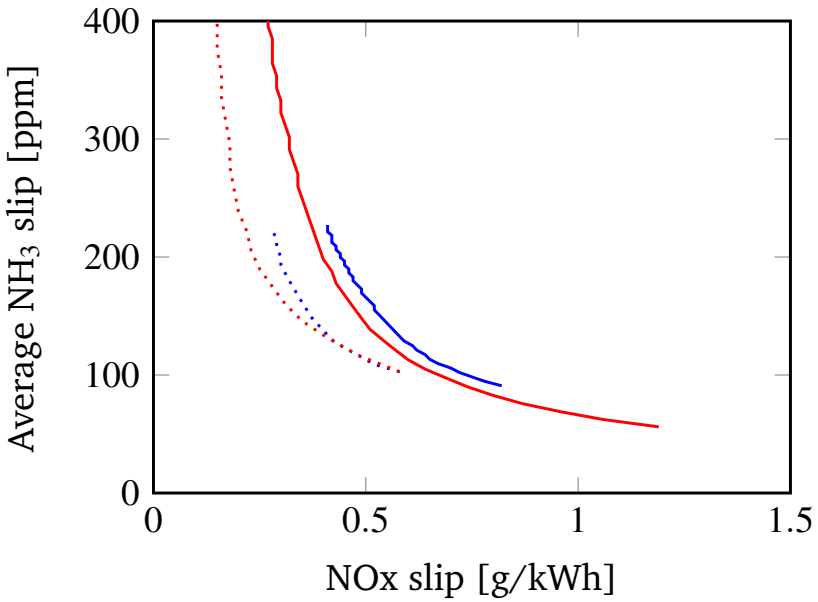

Figure 7.20. Comparison between the 18.7 L catalyst and a 33% bigger monolith for the P and PI controllers with ANR = 1.0. Legend: P ANR = 1.0 (——), PI ANR = 1.0 (——), P ANR = 1.0, 33% bigger monolith (.....), PI ANR = 1.0, 33% bigger monolith (.....)

The study shows that out of the basic control structures, a PI with feedforward is the only structure of interest when balancing performance and complexity. The feedforward is shown to be so important for the overall performance that sensors before the SCR catalyst are required. It is possible to use an engine-NOx map that provides information about the engine outlet NOx levels for different driving conditions. This however suffers from some problems, such as not taking ambient conditions into account.

7.5 Conclusions

A methodology has been presented that uses pareto fronts to analyse how changes in the urea dosing control structure can improve the trade-off between NOx slip and NH_3 slip. The results from the simulation showed that, out of the tested controllers, a PI controller coupled with ANR based feedforward performed the best. In the experimental tests of the controllers, the PD controller with feedforward performed best, however the differences between the controllers was small. Using a combination of feedforward and feedback performed best both in simulation and experimental tests. The methodology enables conclusions to be drawn regarding which control structure performs best. The analysis can be conducted with a simulation model, thereby minimizing experimental effort.

Chapter 8

System Wide Modelling of the Exhaust Gas Cleaning System

A methodology to develop a modular simulation tool capable of simulating the whole catalytic exhaust system is presented. The methodology describes the steps required to go from problem formulation to the final modular simulation tool. Models for the different exhaust gas cleaning catalysts are presented, and the methodology is applied to make a modular simulation tool. The simulation tool is used to simulate various system designs. The main contributions of this chapter are published in (A. Åberg, T. K. Hansen, K. Linde, A. K. Nielsen, R. Damborg, A. Widd, J. Abildskov, A. D. Jensen, J. K. Huusom. A Framework for Modular Modeling of the Diesel Engine Exhaust Gas Cleaning System. Computer Aided Chemical Engineering 37 (2015) 455-460.) and (T. Christiansen, J. Sydney, A. Åberg, J. Abildskov, J. K. Huusom. Methodology for Developing a Diesel Exhaust After Treatment Simulation Tool. Submitted to SAE Technical Papers, 2016)

8.1 Introduction

To be able to fully understand and optimize the aftertreatment system without using too many resources, it is beneficial to be able to simulate the complete system under different scenarios. A modular simulation tool consisting of different blocks representing the different catalysts would be able to simulate almost all configurations of diesel flue gas cleaning systems. The main advantage with a modular structure is that it allows for changes in a single or several blocks. For example, the model structure or the catalyst formulation in one of the catalysts can be changed with minimal effort. Volumes of the catalysts, parameter values, etc. can be changed to investigate the effect the changes will have on the overall system performance. It would be possible to go between different catalyst configurations. It would also be possible to simulate combinatorial dynamic effects, for example how changing one catalyst will affect the dynamics of the whole system. The experimental effort can be reduced substantially if the model accurately can describe the system. To achieve this, models of the catalysts have to be developed or collected from literature and modified in a way so that they can work together.

Modeling of the different catalysts independently has been studied previously in literature. The DOC has been modeled by for example [63], early DPF modeling was done in [12], and a recent review can be found in for example [29]. The SCR has been modeled in this thesis, and for example in [17], and the ASC in [26]. To my knowledge, little effort has been done to develop a methodology to combine independently developed models to create a modular model combining all the catalyst in the system, that is aimed at simulating the complete exhaust system during transient operation. Some software exists that are able to simulate the whole system, for example AVLBoost [13] and Exothermias Axisuite software [103]. Commercial software, while providing excellent user friendliness and performance, is limited with regards to programming language, model structure, and interface, while the presented methodology allows the user to use his or her favourite. This chapter will briefly present four different models that has been used to develop a modular simulation tool. It will present a methodology of the steps needed to make a modular model based on independently developed models.

Relatively simple models are used together with the methodology to illustrate the methodology, however a straight forward extension could be to include more detailed and validated models, to develop a more functional simulation tool.

8.2 Methodology

This section will present a suggested methodology of necessary steps to make a modular model that is able to handle transient simulation. Step 1 through 7 below are the suggested steps.

1. Problem formulation.
2. Model collection and understanding.
3. Data collection.
4. Modification into dynamic formulation.
5. Equalization of the inputs and outputs for the models.
6. Implementation of the models in compatible software.
7. Model validation.

Step 1 involves a proper formulation of the problem: what is the application and how many underlying models are necessary to describe the system. This step will also clearly define if the presented methodology is the correct one to use, since the user should realise if a modular simulation tool is needed. Based on the requirements formulated in 1, the relevant models will be collected in step 2. This involves both channel models and kinetic models. It also concerns understanding the system to such a degree that it can be concluded if a fully dynamic model is necessary, or if the dynamics are so fast that a pseudo-steady state model is enough to handle a transient input. Step 3 involves collection of data for the models. If the models are collected from literature, some physical constants and kinetic constants that are required might be unavailable. Based on the analysis in step 2 and the current configuration of the collected models, step 4 requires the user to modify the models into a dynamic formulation. For the models to be able to work together, the inputs and outputs must be matched in all the underlying models, which is done in step 5. To be able to simulate the models together, step 6 instructs the user to implement the models in compatible software. This is a non-trivial step that requires that the models are implemented in a structured way, to ensure that they can be easily exchanged and modified. Figure 8.1 shows an overview of a suggested model implementation. The call function defines the catalyst properties such as chemical composition and volume. The physical models, kinetic models, and physical parameter models are also defined, ensuring that the correct models are used in

the different model blocks. The call function also specifies the inlet conditions and defines the discretisation methods that should be used to solve the models. Model blocks 1 through 3 represents the different units in the exhaust cleaning system, such as an SCR catalyst or DPF. It can however also represent a urea dosing device, or a piece of tubing between the monoliths. The boxes Kin 1 through 3 represents the kinetic models that should be coupled with the physical models. If the model block represents a catalytic unit, the kinetic model defines the reactions occurring, however if the model block represents a piece of pipe, a kinetic model is not necessarily required. The boxes labelled Phys 1 through 3 represents physical parameter models, such as film transfer coefficients and diffusion coefficients, that are state dependant. Parameters that does not depend on the conditions in the model block, should be defined in the call function instead. If the models are implemented in a way such as this, or similar, the simulation tool becomes highly modular and flexible, and can be used for a multitude of different system simulations.

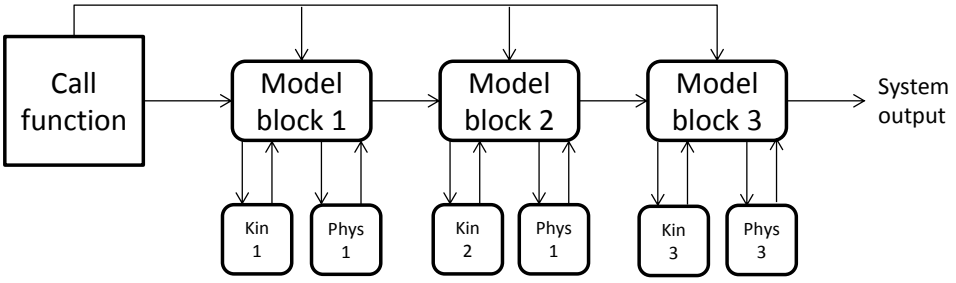

Figure 8.1. Example of how the implementation of the simulation tool can be structured.

When the modular model is working, a recommended step is to validate the model. Since the nature of the model is modular, it will require much experimental effort to validate all configurations, thus it is preferable to use well validated models from the start.

8.3 Models

To apply the methodology four models were taken from literature and coupled with kinetic models from literature. This section will present the models. The channel models for the Diesel Oxidation Catalyst (DOC), SCR, and Ammonia Slip Catalyst (ASC) are structurally similar, since the monoliths are of flow-through design. For the simplified models it was assumed that:

1. The channels are identical and has square shape.

2. There is no heat transport by conduction.

3. There is no heat loss to the surroundings.

4. Temperature, concentrations and velocity are uniformly distributed.

5. All flow in radial direction has been neglected.

8.3.1 DOC Model

The model for the DOC was developed by Kim and Kim [63], and was slightly modified to fit with the presented assumptions. The mass balances can be summarized in the following equations:

$$\frac{\partial C_{i,g}}{\partial t} = -u\frac{\partial C_{i,g}}{\partial x} + \frac{k_{m,i}(x)S}{\phi}(C_{i,s} - C_{i,g}) \tag{8.1}$$

$$\frac{\mathrm{d}C_{i,s}}{\mathrm{d}t} = \frac{k_{m,i}(x)S}{1-\phi}(C_{i,g} - C_{i,s}) + \frac{ap_t}{1-\phi}\sum_{k}^{N_R} v_{i,k}r_k \tag{8.2}$$

where $C_{i,g}$ is the gas concentration in the channel phase for species i, $C_{i,s}$ is the concentration in the solid phase for species i, u is the linear gas velocity, $k_{m,i}$ is the film transfer coefficient for mass for species i, ϕ is the fraction of channel area in the cross sectional area of the monolith channel, S is the geometric surface area, a is the active site surface area, and $i = CO,\ HC,\ NO,\ NO_2,\ O_2$. The temparature equations are:

$$\frac{\partial T_g}{\partial t} = -u\frac{\partial T_g}{\partial x} + \frac{h_t(x)S}{\phi\rho_g c_{p,g}}(T_s - T_g) \tag{8.3}$$

$$\frac{\mathrm{d}T_s}{\partial t} = \frac{h_t(x)S}{(1-\phi)\rho_s c_{p,s}}(T_g - T_s) + \frac{ap_t}{(1-\phi)\rho_s c_{p,s}}\sum_{k}^{N_R} -\Delta H_k r_k \tag{8.4}$$

where T_g is the channel phase gas temperature, T_s is the solid phase gas temperature, h_t is the film transfer coefficient for heat, ρ_g is the gas density, $c_{p,g}$ is the gas heat capacity, ρ_s is the solid phase density, and $c_{p,s}$ is the solid phase heat capacity. The system of equations requires boundary conditions and initial conditions to be

solved. These can be written as:

$$C_{i,g}(x=0,t) = C_{i,g}^{in}(t) \tag{8.5}$$

$$T_g(x=0,t) = T_g^{in} \tag{8.6}$$

$$C_{i,g}(x,t=0) = C_{i,g}^{0}(x) \tag{8.7}$$

$$C_{i,s}(x,t=0) = C_{i,s}^{0}(x) \tag{8.8}$$

$$T_g(x,t=0) = T_g^{0}(x) \tag{8.9}$$

$$T_s(x,t=0) = T_s^{0}(x) \tag{8.10}$$

The kinetic model coupled with the channel model was described by Kim and Kim as well [63]. The kinetic model considered three different chemical reactions, the oxidation of CO into CO_2, the oxidation of HC, which was assumed to be C_3H_6, and the oxidation of NO into NO_2. The kinetic parameters were also taken from Kim and Kim [63].

8.3.2 DPF Model

The model that was used for simulating the DPF was very simplified compared to what can be found in literature. Pressure loses, which is an important state in the DPF for determining when the filters needs to be regenerated, was neglected. It was simply assumed that 99% of the soot was retained in the filter. To include the most significant effect the DPF has on the chemical gas composition, the regeneration reaction where NO_2 oxidises the soot was included. Since no pressure loss was present, the filter mass balance was described using a similar equations structure as presented for the DOC.

$$\frac{\partial C_{i,g}}{\partial t} = -u\frac{\partial C_{i,g}}{\partial x} + \sum_{k}^{N_R} v_{i,k} r_k \tag{8.11}$$

The chemical reaction included was:

$$\mathrm{C} + 2\mathrm{NO_2} \rightarrow \mathrm{CO_2} + 2\mathrm{NO} \tag{8.12}$$

which was modelled using a standard Arrhenius based expression

$$r_{C,ox} = k_0 \exp\left(-E_A/RT\right) C_C C_{NO_2}^2 \tag{8.13}$$

where the kinetic parameters were taken as $E_A = 48.57\mathrm{kJ/mol}$, $k_0 = 3.16 \cdot 10^{13}\mathrm{m^6/mol^2 s}$.

8.3.3 SCR Model

The model that was used for the SCR monolith was not based on the models presented in Chapter 3, but instead the model presented by Opitz et al. was used [95]. The model is structurally similar to model 2 used in this thesis, and can be described as:

$$\frac{\partial C_{i,g}}{\partial t} = -u\frac{\partial C_{i,g}}{\partial x} - \frac{4}{D_h}k_{m,i}(x)(C_{i,g} - C_{i,s}) \tag{8.14}$$

$$\frac{\partial C_{i,s}}{\partial t} = Sk_{m,i}(x) + \sum_{k}^{N_R} v_{i,k}r_k \tag{8.15}$$

$$\frac{\partial T_g}{\partial t} = -u\frac{\partial T_g}{\partial x} - h_t(x)\frac{4}{D_h c_{p,g}\rho_g}(T_g - T_s) \tag{8.16}$$

$$\frac{\partial T_s}{\partial t} = h_t(x)\frac{S}{c_{p,s}\rho_s}(T_g - T_s) + \frac{1}{c_{p,s}\rho_s}\sum_{k}^{N_R} -\Delta H_k r_k \tag{8.17}$$

The boundary and initial conditions required to solve the model were:

$$C_{i,g}(x=0,t) = C_{i,g}^{in}(t) \tag{8.18}$$

$$T_g(x=0,t) = T_g^{in}(t) \tag{8.19}$$

$$C_{i,g}(x,t=0) = C_{i,g}^{0}(x) \tag{8.20}$$

$$C_{i,s}(x,t=0) = C_{i,s}^{0}(x) \tag{8.21}$$

$$T_g(x,t=0) = T_g^{0}(x) \tag{8.22}$$

$$T_s(x,t=0) = T_s^{0}(x) \tag{8.23}$$

where D_h is the hydraulic diameter of the channel, and the rest as previously defined. The kinetic model that was coupled with the channel model was based on a Cu-zeolite SCR catalyst and presented by Pant and Schmieg [96], from which the kinetic parameters were taken as well.

8.3.4 ASC Model

Depending on the physical structure of the ASC, the models for monolith can be different. A common structure is that the ASC has two different washcoat layers, where on acts as a oxidation layer and the other as a SCR layer. This improves the catalysts selectivity towards N_2. The idea is that excess NH_3 from the SCR monolith is oxidised to NO in the bottom layer of the washcoat, and the NO is reacted into N_2 in the SCR layer in the typical SCR reactions. An overview of this can be seen in Figure 8.2. The dual-layer ASC was used here. The two catalytic layers were treated

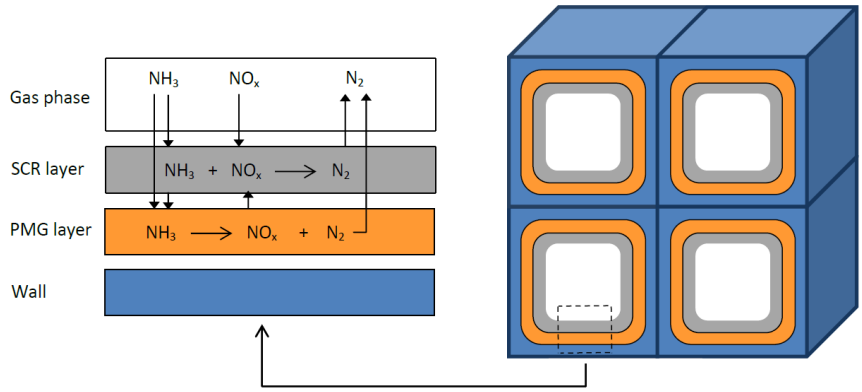

Figure 8.2. Schematic view of a dual-layer ASC monolith.

as surfaces, and assumed to be connected through film transfer. The equations used to model the channel and surface physics were:

$$\frac{\partial C_{i,g}}{\partial t} = -u\frac{\partial C_{i,g}}{\partial x} + k^I_{m,i}S(C^{tl}_{i,s} - C_{i,g}) \tag{8.24}$$

$$\frac{\partial C^{tl}_{i,s}}{\partial t} = \frac{k^I_{m,i}S}{(1-\phi)\varepsilon_{wc}}(C_{i,g} - C^{tl}_{i,s}) + \frac{k^{II}_{m,i}S}{(1-\phi)\varepsilon_{wc}}(C^{bl}_{i,s} - C^{tl}_{i,s}) + \frac{1}{(1-\phi)\varepsilon_{wc}}\sum_k^{N_R} -\nu_{i,k}r^{tl}_k \tag{8.25}$$

$$\frac{\partial C^{bl}_{i,s}}{\partial t} = \frac{k^{II}_{m,i}S}{(1-\phi)\varepsilon_{wc}}(C^{tl}_{i,s} - C^{bl}_{i,s}) + \frac{1}{(1-\phi)\varepsilon_{wc}}\sum_k^{N_R} -\nu_{i,k}r^{bl}_k \tag{8.26}$$

$$\frac{\partial T_g}{\partial t} = -u\frac{\partial T_g}{\partial x} + \frac{h^I_t S}{\rho_g c_{p,g}}(T^{tl}_s - T_g) \tag{8.27}$$

$$\frac{\partial T^{tl}_s}{\partial t} = \frac{h^I_t S}{(1-\phi)\rho_s c_{p,s}}(T_g - T^{tl}_s) + \frac{h^{II}_t S}{(1-\phi)\rho_s c_{p,s}}(T^{bl}_s - T^{tl}_s) + \frac{1}{(1-\phi)\rho_s c_{p,s}}\sum_k^{N_R} -\Delta H^{tl}_k r^{tl}_k \tag{8.28}$$

$$\frac{\partial T^{bl}_s}{\partial t} = \frac{h^{II}_t S}{(1-\phi)\rho_s c_{p,s}}(T^{tl}_s - T^{bl}_s) + \frac{1}{(1-\phi)\rho_s c_{p,s}}\sum_k^{N_R} -\Delta H^{bl}_k r^{bl}_k \tag{8.29}$$

where the superscripts tl means top layer, bl bottom layer, I is the gas-solid interface, II is the solid-solid interface, ε_{wc} is the porosity of the washcoat, and the rest

as previously defined. The boundary and initial conditions are as previously:

$$C_{i,g}(x=0,t) = C_{i,g}^{in}(t) \tag{8.30}$$
$$T_g(x=0,t) = T_g^{in}(t) \tag{8.31}$$
$$C_{i,g}(x,t=0) = C_{i,g}^{0}(x) \tag{8.32}$$
$$C_{i,s}^{tl}(x,t=0) = C_{i,s}^{tl,0}(x) \tag{8.33}$$
$$C_{i,s}^{bl}(x,t=0) = C_{i,s}^{bl,0}(x) \tag{8.34}$$
$$T_g(x,t=0) = T_g^{0}(x) \tag{8.35}$$
$$T_s^{tl}(x,t=0) = T_s^{tl,0}(x) \tag{8.36}$$
$$T_s^{bl}(x,t=0) = T_s^{bl,0}(x) \tag{8.37}$$

The chemistry required to describe the reactions for the ASC requires one model for each catalytic layer. For the top SCR layer, the same kinetic model was used as was presented for the SCR model in Section 8.3.3. For the oxidation layer the kinetic model was based on the model reported by Scheuer et al. [107], from which the kinetic parameters were taken as well.

8.3.5 Implementation

The presented models has been implemented using the earlier described methodology. The main thing to consider when the modular simulation tool is developed is to ensure that the inputs and outputs remains the same for all units. Table 8.1 shows the different inputs and outputs, and in which units they actively take part. The species in the table are always included as inputs and outputs in the simulation tool, however for units where they do not take part, the simply pass through and are treated as inerts.

Table 8.1. Overview of the relevant chemical species and in which unit the actively take part.

Module	DOC	DPF	SCR	ASC
O_2	X		X	X
CO	X			
HC	X			
PM		X		
NO	X	X	X	X
NO_2	X	X	X	X
NH_3			X	X

The models were implemented in the commercial software Matlab [94], in the way that was described in Figure 8.1.

8.4 Results

This section will present results from simulations using the modular simulation tool. The models were initially simulated individually to ensure that the overall trends for the models were realistic. It should be noted that the models were not validated or calibrated in any form, besides the work that were done by the individual authors in the papers where the models were collected. The purpose of these results are therefore not to accurately investigate the effect of each monolith, but rather highlight the advantage of developing a modular simulation tool.

The parameters and inlet conditions that were used for simulation can be seen in Table 8.2.

Figures 8.3 through 8.5 shows the steady-state results from a simulation of the standard exhaust gas cleaning system for Euro VI, at 200, 300, and 400^{o}C. The figures clearly shows that the ratio of NO/NO_2 changes in the DOC, since NO is being oxidized. The DPF uses some of the NO_2 for regeneration, and therefore affects the ratio as well. The temperature affects the amount of NH_3 exiting the SCR catalyst, since the desorption is temperature dependent. Note that since NH_3 oxidation is not included, and that the NOx conversion is close to 100% for all temperatures, the temperature is the only factor affecting the SCR NH_3 outlet. The differences between temperatures are however insignificant in this simulation, indicating that the models has to be calibrated and validated if any proper conclusions should be possible.

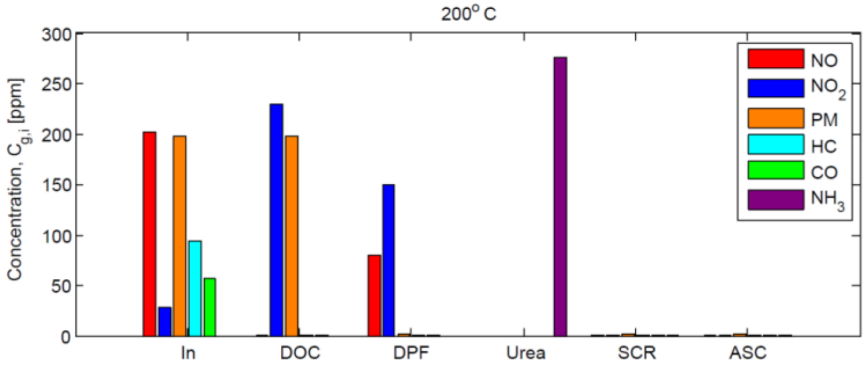

Figure 8.3. Simulation of the standard Euro VI exhaust cleaning system at 200^{o}C. The staples shows the composition of the gases at the outlet of each unit.

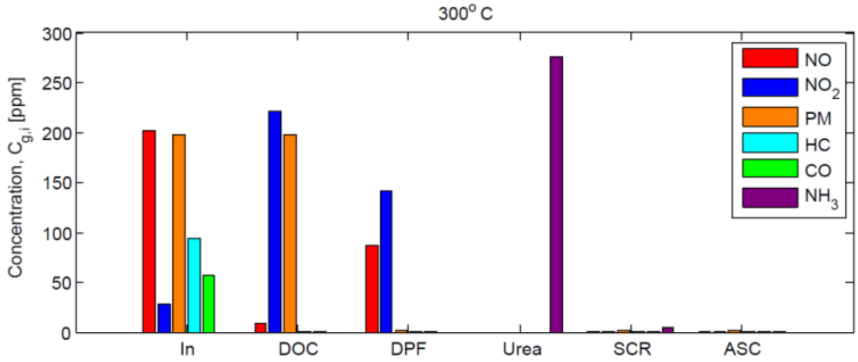

Figure 8.4. Simulation of the standard Euro VI exhaust cleaning system at 300^{o}C. The staples shows the composition of the gases at the outlet of each unit.

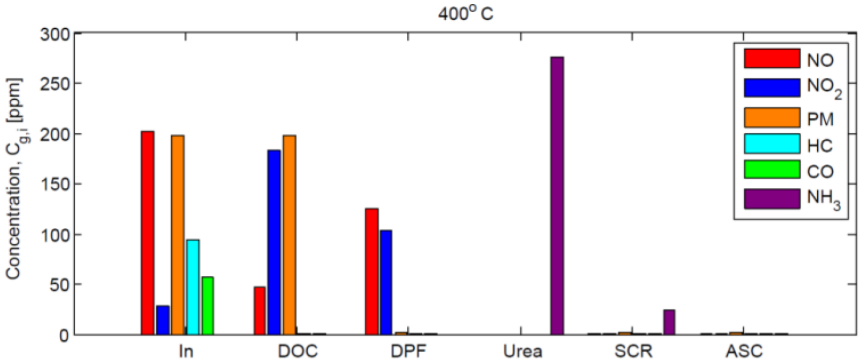

Figure 8.5. Simulation of the standard Euro VI exhaust cleaning system at 400^{o}C. The staples shows the composition of the gases at the outlet of each unit.

An important feature of the program is that the system can be simulated using different configurations of the monoliths. To show this, a simulation has been run where the order is SCR-ASC-DOC-DPF, at 200^{o}C. Figure 8.6 shows the results. If the results are compared to Figure 8.3, it can be seen that the alternative monolith configuration results in different outlet conditions. Since the SCR monolith now is placed directly after the engine, the NO_2/NO ratio is lower, resulting in less of the fast SCR reaction, and therefore not as high NOx conversion. In practice, there would be other effects, such as a faster warm up of the SCR monolith. Since the steady-state results are shown here, the effect of this is not seen.

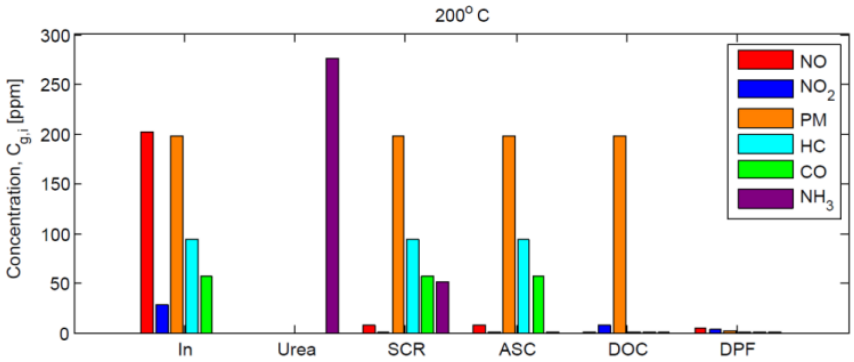

Figure 8.6. Simulation of the standard Euro VI exhaust cleaning system at 400^{o}C. The staples shows the composition of the gases at the outlet of each unit.

8.5 Discussion

The automotive exhast gas aftertreatment system of heavy-duty trucks are complicated systems that consists of several aftertreatment devices, along with other devices such as an AdBlue dosing system, mixers, pipes and sensors for measuring the states. To achieve a simulation tool that can take every part into consideration, all of these things has to be described mathematically. The presented methodology provides instructions on how a modular simulation tool can be developed. The main factor to consider is to ensure that the inputs and outputs of the different parts that are modelled are coherent. The methodology has only been applied to the monoliths of the aftertreatment system, however the same principles applies if other devices should be included as well.

As stated, ensuring that the mathematical models can be integrated into the simulation tool is the main factor to consider. The other problems in developing the simulation tool are mostly related to programming, in ensuring that the tool is easy to use, and is flexible enough to be able to simulate different systems. If the methodology outlined in Figure 8.1 is used, this ensures that the system can handle a broad variety of systems.

By choosing to develop a modular simulation tool, a flexible tool is achieved that can be used for several applications, such as system wide optimisation, investigations of how the system responds to changes in monolith order, investigations of changes to catalyst volume, catalyst composition, etc. The main advantage lies in the fact that the effect on the total system can be analysed for changes in one catalyst. Since the engine exhaust gas in a diesel application changes dramatically

in terms of flow, composition, and temperature as the driving conditions change, detalied studies of the benefits and disadvantages for the aftertreatment system design needs to be tested for a large variety of scenarios, something that can be very resource intensive if a simulation tool is not available. Another application of the simulation tool is to investigate how new innovative units can be integrated into the system. For example, combining the DPF and SCR, or the SCR and ASC. The effect such a combination would have on the overall system performance could easily be investigated, as long as a model is available for the unit. While there are commercial software available that can simulate the aftertreatment system, they are often limited with regards to programming language, and integration into other software. Daimler has reported that the company has developed its own exhaust aftertreatment simulation tool based on Matlab/Simulink [133].

8.6 Conclusions

A methodology to develop a simulation tool for the exhaust gas aftertreatment system has been presented. The methodology describes the steps that are required to ensure that mathematical models describing the different units of the system can be integrated and simulated together. The methodology has been applied by constructing a simulation tool that has been used to simulate the exhaust system at different temperatures with realistic inlet conditions. The uses of the tool has been exemplified by simulating an alternative configuration to the standard Euro VI exhaust system.

Table 8.2. Parameters and inlet conditions used for simulation.

	Factors	Value	Unit
Exhaust gas	p	101 325	Pa
	$c_p \cdot \rho$	$5.0 \cdot 10^4$	J/(m^{3}K)
	C_{CO}^{in}	56.4	ppm
	$C_{O_2}^{in}$	$7.0 \cdot 10^4$	ppm
	C_{HC}^{in}	94.0	ppm
	C_{C}^{in}	197.5	ppm
	C_{NO}^{in}	202.1	ppm
	$C_{NO_2}^{in}$	27.7	ppm
	ANF	1.2	-
DOC	L	0.1016	m
	S	2610	m^2/m^3
	φ	0.5	-
DPF	L	0.1524	m
SCR	L	0.2286	m
	S	2784	m^2/m^3
	D_h	$1.16 \cdot 10^{-3}$	m
	Ω_{max}	95	mol/m^3
	Γ	31	mol-sites/m^3
ASC	L	0.1016	m
	S	1431	m^2/m^3
	φ	0.4	-
	ε_{WC}	0.5	-
	Γ	11.6	mol/m^3
Cordierite	λ	0.85	W/(m K)
	c_p	$1.52 \cdot 10^3$	J/(kg K)
	ρ	140	kg/m^3

Chapter 9

Conclusion

This thesis has focused on increasing the knowledge regarding modelling and control of the SCR monolith. This has been achieved through several different tasks, presented in the previous chapters. The basis was five SCR monolith models that were presented in Chapter 3. Model 1 included the least simplifications, while the other five models included simplifications related to mass and heat transfer. A kinetic model was presented that included most of the relevant reactions taking place inside the monolith. The kinetic model was used together with all the presented channel models. It was concluded that the internal mass transfer in one of the studied models was likely not significant, which was confirmed during the experimental calibration of the kinetic parameters.

A methodology to estimate kinetic parameters using bench-scale reactor data and full-scale transient data was presented. The methodology does not depend on TPD tests, which can compromise the quality of the adsorption and desorption parameters. The methodology was applied to varying extent to the presented models in Chapter 3. The models were able to capture the steady-state behaviour of the small-scale SCR monolith well. The difference between models 1 and 2 was insignificant during calibration, and it was therefore concluded that the internal mass transfer was not significant. Models 2, 3, and 5 were validated using full-scale engine data following the European Transient Cycle (ETC). The results showed that while models 2 and 3 perform satisfactory with regards to NOx prediction, the simplifications of model 5 makes it less suitable for this application. Model 2 can to a satisfactory degree predict the NH_3 slip, however it is underestimated.

To further investigate the effect of the different simplifications, a model analysis has been presented, where the predictive performance related to NOx was investi-

gated for models 2, 3, 4, and 5. The models were first analysed using the kinetic parameters of model 2. This showed, as expected, that model 2 performed best. The performance of model 3 was close to model 2, while the simplifications of models 4 and 5 resulted in a significant information loss. Based on the results, the calibration methodology was applied to models 3 and 5 and the analysis was carried out again. The results showed that using kinetic parameters specific for each model improved the predictive performance for all models. The simplifications related to mass transfer resulted in the smallest information loss.

This thesis has presented a methodology that uses pareto fronts to analyse how changes in the urea dosing control structure can improve the trade-off between NOx slip and NH_3 slip. The methodology can be used to investigate how changes in the control structure improves the NOx-NH_3 trade-off. P, PI, PD, and PID controllers, both with and without Ammonia-NOx-Ratio (ANR) based feedforward were implemented and tested using the methodology. The results showed that, out of the tested controllers, a PI controller coupled with ANR based feedforward performed the best in simulation. In the experimental tests of the controllers, the PD controller with feedforward performed best, however the differences between the controllers was small. The methodology showed that using a combination of feedforward and feedback is necessary for high performance based on both the simulation and experimental data.

The last subject that has been discussed in this thesis is related to system wide modelling of the exhaust gas cleaning system. While modelling and simulating the SCR monolith itself is a good start to gaining insight, the full system is more complex. Several different units are normally present in the system, and it cannot be assumed that the SCR catalyst is the first monolith in the system. To investigate how the entire system can be modelled, a methodology to develop a simulation tool for the exhaust gas aftertreatment system has been presented. The methodology describes the steps that are required to ensure that mathematical models describing the different units of the system can be integrated and simulated together. The methodology has been applied by constructing a simulation tool that has been used to simulate the exhaust system.

The above topics are believed to have further increased knowledge about how the SCR monolith is modelled and controlled. Insight has been achieved regarding how well the presented models can predict the SCR monolith output for a full-scale monolith treating real engine gases, how simplifications related to the channel model affects the predictive performance, and how the NOx-NH_3 trade-off can be

analysed for different control structures.

Bibliography

[1] Diesel exhaust: Critical analysis of emissions, exposure and health effects. Technical report, Health Effects Institute, April 1995.

[2] Proposed identification of diesel exhaust as a toxic air contaminant. Technical report, California Air Resources Board and the Office of Environmental Health Hazard Assessment, 1998.

[3] Commission regulation (eu) no 582/2011. Technical report, European Union, May 2011.

[4] G. H. Abd-Alla. Using exhaust gas recirculation in internal combustion engines: a review. *Energy Conversion and Management*, 43(8):1027–1042, 2002.

[5] A. Åberg, A. Widd, J. Abildskov, and J. K. Huusom. Estimation of kinetic parameters in an automotive scr catalyst model. *Topics in Catalysis*, 59(10-12):945–951, 2016.

[6] A. Åberg, A. Widd, J. Abildskov, and J. K. Huusom. Parameter estimation and analysis of an automotive heavy-duty scr catalyst model. *Chemical Engineering Science*, 161:167–177, 2017.

[7] S. L. Andersson, P. L. T. Gabrielsson, and C. U. I. Odenbrand. Reducing nox in diesel exhausts by scr technique: experiments and simulations. *AIChE Journal*, 40(11):1911–1919, 1994.

[8] J. Ando, H. Tohata, and G. A. Isaacs. Nox abatement for stationary sources in japan. Technical report, U. S. Environmental Protection Agency EPA-600/2-76-013b, 1976.

[9] S. Arnold. Single sequential turbocharger: A new boosting concept for ultra-

low emission diesel engines. *SAE International Journal of Engines*, 1:232–239, 2009.

[10] K. J. Åström and M. Murray. *Feedback Systems: An Introduction for Scientists and Engineers*. Princeton University Press, 2008.

[11] A. M. Beale, F. Gao, I. Lezcano-Gonzalez, C. H. F. Peden, and J. Szanyi. Recent advances in automotive catalysis for nox emission control by small-pore microporous materials. *Chemical Society Reviews*, 44:7371–7405, 2015.

[12] E. J. Bissett. Mathematical model of the thermal generation of a wall-flow monolith diesel particulate filter. *Chemical Engineering Science*, 39:1233–1244, 1984.

[13] AVL Boost. https://www.avl.com/sv/boost, 2014.

[14] S. Brandenberger, O. Kröcher, A. Tissler, and R. Althoff. The state of the art in selective catalytic reduction of nox by ammonia using metal-exchanged zeolite catalysts. *Catalysis Reviews - Science and Engineering*, 50:492–531, 2008.

[15] D ChatterjeJ. Wang. Burkhardt, M. Weibel, and I. Nova. Numerical simulation of zeolite- and v-based scr catalytic converters. *SAE Technical Paper*, 2007-01-1136, 2007.

[16] S. J. Charlton. *Handbook of Air Pollution from Internal Combustion Engines*. Academic Press, 1998.

[17] D. Chatterjee, T. Burkhardt, M. Weibel, I. Nova, A. Grossale, and E. Tronconi. Numerical simulation of ammonia scr-catalytic converters: Model development and application. *SAE Technical Paper*, 2005-01-0965, 2005.

[18] D. Chatterjee, T. Burkhardt, M. Weibel, E. Tronconi, I. Nova, and C. Ciardelli. Numerical simulation of no/no2/nh3 reactions on scr-catalytic converters: Model development and applications. *SAE Technical Papers*, 2006-01-0468, 2006.

[19] C.-T. Chen and W.-L. Tan. Mathematical modeling, optimal design and control of an scr reactor for nox removal. *Journal of the Taiwan Institute of Chemical Engineers*, 43:409–419, 2012.

[20] P. Chen and J. Wang. Control-oriented model for integrated diesel engine and aftertreatment systems thermal management. *Control Engineering Practice*, 22:81–93, 2014.

[21] J. N. Chi and H. F. M. DaCosta. Modeling and control of a urea-scr aftertreatment system. *SAE Technical Paper*, 2005-01-0966, 2005.

[22] S. M. Cho. Properly apply selective catalytic reduction for nox removal. *Chemical Engineering Progress*, 1994.

[23] E. Y. Choi, I. S. Nam, and Y. G. Kim. Tpd study of mordenite-type zeolites for selective catalytic reduction of no by nh3. *Journal of Catalysts*, 161:597–604, 1996.

[24] T. Christiansen, J. Sydney, A. Åberg, J. Abildskov, and J. K. Huusom. Methodology for developing a diesel exhaust after treatment simulation tool. Submitted to SAE Technical Papers, 2016.

[25] M. Colombo, I. Nova, and E. Tronconi. A comparative study of the nh3-scr rreaction over a cu-zerolite and a fe-zeolite catalyst. *Catal. Today*, 151:223–230, 2010.

[26] M. Colombo, I. Nova, and E. Tronconi. A simplified approach to modeling of dual-layer ammonia slip catalysts. *Chemical Engineering Science*, 75:75–83, 2012.

[27] B. J. Cooper, A. C. McDonnald, A. P. Walker, and M. Sanchez. The development and on-road performance and durability of the four-way emission control scrt system. In *US DOE, 9th Diesel Engine Emissions Reduction Conference (DEER), Newport, RI*, 2003.

[28] F. Covassin, M. Preziuso, M. D. Cesare, and G. Serra. A mean value model of the exhaust system with scr for an automotive diesel engine. *SAE Technical Paper*, 2009-24-0131, 2009.

[29] C. Depcik, J. C. Ragone, O. Haralampous, and G. Koltsakis. Catalyzed diesel particulate modeling. *Reviews in Chemical Engineering*, 29:1–61, 2013.

[30] M. Devarakond, G. Parker, J. H. Johnson, and V. Strots. Model-based control system design in a urea-scr aftertreatment system based on nh3 sensor feedback. *International Journal of Automotive Technology*, 10(6):653–662, 2009.

[31] M. Devarakonda, G. Parker, J. H. Johnson, V. Strots, and S. Santhanam. Model-based estimation and control system development in a urea-scr aftertreatment system. *SAE International Journal of Fuels and Lubricants*, 1(1):646–661, 2008.

[32] DieselNet. Available: http://www.dieselnet.com/standards/cycles/etc.php.

[33] Honggyi Dong, Shijin Shuai, and Jianxin Wang. Effect of urea thermal decomposition on diesel nox-scr aftertreatment systems. *SAE Papers*, 2008-01-1544, 2008.

[34] B. L. D. Duffy, H. E. Curry Hyde, N. W. Cant, and P. F. Nelson. Isotopic labeling studies of the effects of temperature, water and vanadia loading on the selective catalytic reduction of no with nh3 over vanadia-titania catalysts. *Journal of Physical Chemistry*, 98:7153, 1994.

[35] J. A. Dumesic, N.-Y. Topsoe, H. Topsoe, Y. Chen, and T. Slabiak. Kinetics of selective catalytic reduction of nitric oxide by ammonia over vanadia/titania. *Journal of Catalysis*, 163:409–417, 1996.

[36] P. Forzatti and L. Lietti. Recent advances in denoxing catalysis for stationary applications. *Heterogeneous Chemistry Reviews*, 3(1):33–51, 1996.

[37] P. Forzatti, I. Nova, and E. Tronconi. Enhanced nh3 selective catalytic reduction for nox abatement. *Angewandte Chemie*, 121(44):8516–8518, 2009.

[38] P. Forzatti, I. Nova, and E. Tronconi. New "enhanced nh3-scr" reaction for nox emission control. *Industrial & Engineering Chemistry Research*, 49(21):10386–10391, 2010.

[39] A. Fritz and V. Pitchon. The current state of research on automotive lean nox catalysts. *Applied Catalysis B: Environmental*, 1, 1997.

[40] G. Froment, J. DeWilde, and K. Bischoff. *Chemical Reactor Analysis and Design*. John Wiley & Sons Inc., 3rd edition edition, 2011.

[41] P. Gabrielsson. Urea-scr in automotive applications. *Topics in Catalysis*, 28:1–4, 2004.

[42] Pär Gabrielsson, Ioannis Gekas, Peter Schoubye, Søren Æ. Mikkelsen, and Svend Frederiksen. Combined silencers and urea-scr systems for heavy-duty diesel vehicles for oem and retrofit markets. *SAE Papers*, 2001-01-0517, 2001.

[43] J. W. Girard, C. Montreuil, J. Kim, G. Cavataio, and C. Lambert. Technical advantages of vanadium scr systems for diesel nox control in emerging markets. *SAE International Journal of Fuels and Lubricants*, 1(1):488–494, 2008.

[44] J. L. Harned. Analytical evaluation of a catalytic converter system. *SAE*

Technical Paper, 720520, 1972.

[45] C. Havenith and R. P. Verbeek. Transient performance of a urea denox catalyst for low emissions heavy-duty diesel engines. *SAE Technical Paper*, 970185, 1997.

[46] D. Hayes. Adblue to help cut diesel exhaust emissions. *Petroleum Review*, 59:10–11, 2005.

[47] R. M. Heck and R. J. Farrauto. Automobile exhaust catalysis. *Applied Catalysis A: General*, 221, 2001.

[48] A. Herman, M.-C. Wu, D. Cabush, and M. Shost. Model based control of scr dosing and obd strategies with feedback from nh3 sensors. *SAE Technical Paper*, 2009-01-0911, 2009.

[49] J. B. Heywood. *Internal Combustion Engine Fundamentals*. McGraw Hill, 1988.

[50] R. Holder, M. Bollig, D. R. Anderson, and J. K. Hochmuth. A discussion on transport phenomena and three-way kinetics of monolithic converters. *Chemical Engineering Science*, 61(24):8010–8027, 2006.

[51] M.-F. Hsieh and J. Wang. A two-cell backstepping-based control strategy for diesel engine selective catalytic reduction systems. *IEEE Transactions on Control Systems Technology*, 19(6):1504–1515, 2011.

[52] M.-F. Hsieh and J. Wang. *Urea-SCR Technology for deNOx After Treatment of Diesel Exhausts, Chapter 14*. Springer, 2014.

[53] J. Hu, Y. Zhao, Y. Zhang, S. Shuai, and J. Wang. Development of closed-loop control strategy for urea-scr based on nox sensors. *SAE Papers*, 2011-01-1324, 2011.

[54] J. Hussain, K. Palaniradja, N. Alagumurthi, and R. Manimaran. Effect of exhaust gas recirculation (egr) on performance and emission characteristics of a three cylinder direct injection compression ignition engine. *Alexandria Engineering Journal*, 51(4):241–247, 2012.

[55] A. Iserles. *A First Cource in the Numerical Analysis of Differential Equations*. Cambridge University Press, second edition edition, 2009.

[56] T. Ishihara, M. Kagawa, F. Hadama, and Y. Takita. Copper ion-exchanged sapo-34 as a thermostable catalyst for selective reduction of no with c3h6. *Journal of Catalysis*, 169(1):93–102, 1997.

[57] N. Ishikawa, T. Uekusa, T. Nakada, and R. Hariyoshi. Di diesel emission control by optimized fuel injection. *SAE Technical Paper*, 952360, 2004.

[58] M. Iwasaki and H. Shinjoh. A comparative study of "standard", "fast" and "no2" scr reactions over fe/zeolite catalyst. *Applied Catalysis A: General*, 390:71–77, 2010.

[59] J. Jansson. *Urea-SCR Technology for deNOx After Treatment of Diesel Exhausts, Chapter 3*. Springer, 2014.

[60] G. D. Jones and K. L. Johnson. Technology assessment report for industrial boiler applications. Technical report, U. S. Environmental Protection Agency EPA-600/7-79-178, 1979.

[61] K. Kamasamudram, N. W. Currier, X. Chen, and A. Yezerets. Overview of the practically important behaviors of zeolite-based urea-scr catalysts, using compact experimental protocol. *Catalysis Today*, 151(3-4):212–222, 2010.

[62] D. Karamitros and G. Koltsakis. *Urea-SCR Technology for deNOx After Treatment of Diesel Exhausts, Chapter 13*. Springer, 2014.

[63] Y.-D. Kim W.-S. Kim. Re-evaluation and modeling of a commercial diesel oxidation catalyst. *Inustrial & Engineering Chemistry Research*, 48:6579–6590, 2009.

[64] M. Koebel and M. Elsener. Determination of urea and its thermal decomposition products by high-performance liquid chromatography. *Journal of Chromatography A*, 689:164–169, 1995.

[65] M. Koebel, M. Elsener, and M. Kleeman. Urea-scr: a promising technique to reduce nox emissions from automotive diesel engines. *Catalysis Today*, 59:335–345, 2000.

[66] M. Koebel, M. Elsener, and T. Marti. Nox-reduction in diesel exhaust gas with urea and selective catalytic reduction. *Combustion Science and Technology*, 121:85–102, 1996.

[67] M. Koebel, G. Madia, and M. Elsener. Selective catalytic reduction of no and no2 at low temperatures. *Catalysis Today*, 73(3):239–247, 2002.

[68] M. Koebel, G. Madia, F. Raimondi, and A. Wokaun. Enhanced reoxidation of vanadia by no2 in the fast scr reaction. *Journal of Catalysis*, 209(1):159–165, 2002.

[69] Y. Kong, C. Huffmeyer, R. Johnson, B. Taylor, W. Crawley, and G. Hayworth.

Applications of an active diesel particulate filter regeneration system. *SAE Technical Paper*, 2004-01-2660, 2004.

[70] O. Kröcher. *Aspects of Catalyst Development for Mobile Urea-SCR Systems - From Vanadia-Titania Catalysts to Metal-Exchanged Zeolites*, volume Chapter 9. Elsevier, 2007.

[71] J. C. Kuo, C. R. Morgan, and H. G. Lassen. Mathematical modeling of co and hc catalytic converter systems. *SAE Technical Paper*, 710289, 1971.

[72] L. Lietti, I. Nova, S. Camurri, E. Tronconi, and P. Forzatti. Dynamic of the scr-denox reaction by the transient-response method. *AIChE Journal*, 43(10):2559–2570, 1997.

[73] L. Lietti, I. Nova, E. Tronconi, and P. Forzatti. Transient kinetic study of the scr-denox reaction. *Catalysis Today*, 45:85–92, 1998.

[74] A. M. Loeb and W. E. Schiesser. Stiffness and accuracy in the method of lines integration of partial differential equations. In *Proceedings of the 1973 Summer Computer Simulation Coference*, volume 2, pages 25–39, 1973.

[75] G. Madia, M. Koebel, M. Elsener, and A. Wokaun. The effect of an oxidation precatalyst on the nox reduction by ammonia scr. *Industrial & Engineering Chemistry Research*, 41:3512–3517, 2002.

[76] G. Madia, M. Koebel, M. Elsener, and A. Wokaun. Side reactions in the selective catalytic reduction of nox with various no2 fractions. *Industrial & Engineering Chemistry Research*, 41(16):4008–4015, 2002.

[77] Y. Mao, H.-F. Wang, and P. Hu. Theoretical investigation of nh3-scr processes over zeolites: A review. *International Journal of Quantum Chemistry*, 115(10):618–630, 2015.

[78] P. Markatou, J. Dai, A. Johansson, W. Klink, M. Castagnola T. C. Watling, and M. Tutuianu. Fe-zeolite scr model development, validation and application. *SAE Technical Paper*, 2011-01-1304, 2011.

[79] Thomas L. McKinley. *Adaptive Model Predictive Control of Diesel Engine Selective Catalytic Reduction (SCR) Systems*. PhD thesis, University of Illinois at Urbana-Champaign, 2009.

[80] A. Messerer, R. Niessner, and U. Poschl. Comprehensive kinetic characterization of the oxidation and gasification of model and real diesel soot by nitrogen oxides and oxygen under engine exhast conditions: Measure-

ment, langmuir-hinshelwood, and arrhenius parameters. *Carbon*, 44:307–324, 2006.

[81] A. Messerer, R. Niessner, and U. Poschl. Comprehensive kinetic characterization of the oxidation and gasification of model and real diesel soot by nitrogen oxides and oxygen under engine exhaust conditions: Measurement, langmuir-hinshelwood, and arrhenius parameters. *CARBON*, 44(2):307–324, 2006.

[82] A. Miyamoto, M. Inomata, Y. Yamazaki, and Y. Murakami. Mechanism of the reaction between no and nh3 on v2o5 in the presence of oxygen. *Journal of Catalysis*, 57(3):526–527, 1979.

[83] A. Miyamoto, K. Kobayashi, M. Inomata, and Y. Murakami. Nitrogen-15 tracer investigation of the mechanism of the reaction of no with nh3 on vanadium oxide catalysts. *Journal of Physical Chemistry*, 86:2945–2950, 1982.

[84] W. Müller, H. Ölschlegel, A. Schäfer, N. Hakim, and K. Binder. Selective catalytic reduction - europe's nox reduction technology. *SAE Technical Paper*, 2003-01-2304, 2003.

[85] I. Nova, D. Bounechada, R. Maestri, E. Tronconi, A. K Heibel, T. A. Collins, and T. Boger. Influence of the substrate properties on the performances of nh3-scr monolithic catalysts for the aftertreatment of diesel exhaust: An experimental and modeling study. *Industrial & Engineering Chemistry Research*, 50(1):299–309, 2011.

[86] I. Nova, L. Lietti, E. Tronconi, and P. Forzatti. Transient reponse method applied to the kinetic analysis of the denox-scr reaction. *Chemical Engineering Science*, 56:1229–1237, 2001.

[87] I. Nova and E. Tronconi. Kinetic study of the no/no2-nh3 scr rreaction over a v2o5-wo3/tio2 commercial catalyst for the after treatment of diesel eengine exhausts. In *Proceedings of the 2009 IFAC Workshop on Engine and Powertrain Control, Simulation and Modeling*, pages 183–190, 2009.

[88] S. H. Oh and J. C. Cavendish. Transients of monolithic catalytic converters: response to step changes in feedstream temperature as related to controlling automobile emissions. *Industrial & Engineering Chemistry Research*, 37:21–29, 1982.

[89] L. Olsson, H. Sjövall, and R. J. Blint. A kinetic model for ammonia selective catalytic reduction over cu-zsm-5. *Applied Catalysis B: Environmental*,

81:203–217, 2008.

[90] L. Olsson, H. Sjövall, and R. J. Blint. A kinetic model for ammonia selective catalytic reduction over cu-zsm-5. *Applied Catalysis B: Environmental*, 81:203–217, 2008.

[91] Online. https://www.dieselnet.com/tech/diesel_engines.php.

[92] Online. https://www.dieselnet.com/tech/engine_design.php.

[93] Online. www.ni.com/labview?

[94] Online. https://www.mathworks.com/.

[95] B. Opitz, M. Bendrich, A. Drochner, and H. Vogel. Simulation study of scr catalysts with individually adjusted ammonia dosing strategies. *Chemical Engineering Journal*, 264:936–944, 2015.

[96] A. Pant and S. J. Schmieg. Kinetic model of nox scr using urea on commercial cu-zeolite catalyst. *Industrial & Engineering Chemistry Research*, 50(9):5490–5498, 2011.

[97] J. Patchett, R. Verbeek, K. Grimston, G. Rice, J. Calabrese, and M. van Genderen. Control system for mobile nox scr applications. *U. S. Patent 6 581 374*, 2003.

[98] B. E. Poling, J. M. Prausnitz, and J. P. OConnel. *The Properties of Gases and Liquids*. McGraw-Hill International Editions, 5th edition edition, 2001.

[99] H. F. P. Purday. *Diesel Engine Design*. D. Van Nostrand Company, 1919.

[100] K. Ramanathan, V. Balakotaiah, and D. H. West. Light-off criterion and transient analysis of catalytic monoliths. *Chemical Engineering Science*, 58:1381–1405, 2003.

[101] A. R. Ravishankara, J. S. Daniel, and R. W. Portmann. Nitrous oxide (n2o): The dominant ozone-depleting substance emitted in the 21st century. *Science*, 326(5949):123–125, 2009.

[102] L. Rodriguez-Gonzales, F. Hermes, M. Bertmer, E. Rodriguez-Castellon, A. Jimenez-Lopez, and U. Simon. The acid properties of h-zsm-5 as studied by nh3-tpd and al-mas-nmr spectroscopy. *Applied Catalysis A: General*, 328:174–182, 2007.

[103] Exothermia SA, 2014.

[104] B. Scarnegie, W. Miller, B. Ballmert, W. Doelling, and S. Fisher. Recent

dpf/scr results targeting us2007 and euro 4/5 hd emissions. *SAE Technical Paper*, 2003-01-0774, 2003.

[105] C. Schär, C. Onder, and H. Geering. Control of an scr catalytic converter system for mobile heavy-duty application. *IEEE Transactions on Control Systems Technology*, 14:641–653, 2006.

[106] C. M. Schär, C. H. Onder, and H. P. Geering. Control-oriented model of an scr catalytic converter system. *SAE Technical Paper*, 2004-01-0153, 2004.

[107] A. Scheuer, W. Hauptmann, J. Gieshoff, M. Votsmeier, A. Drochner, and H. Vogel. Dual layer automotive ammonia oxidation catalysts: experiments and computer simulation. *Applied Catalysis B: Environmental*, 111-112:445–455, 2012.

[108] K.-P Schindler. Why do we need the diesel? *SAE Technical Paper*, 972684, 1997.

[109] S. Schmieg. Aspects of hc-scr catalyst durability for lean-burn engine exhaust aftertreatment. *SAE International Journal of Fuels and Lubrication*, 3:691–709, 2010.

[110] D. Seher, M. Reichelt, and S. Wickert. Control strategy for nox - emission reduction with scr. *SAE Papers*, 2003-01-3362, 2003.

[111] T. Selleri, I. Nova, and E. Tronconi. Control oriented modeling of low temperature nh3-scr. In *Poster presentation, MODEGAT IV*, 2015.

[112] F. Shakeri and M. Dehghan. The method of lines for solution of the one-dimensional wave equation subject to an integral conservation condition. *Computers & Mathematics with Applications*, 56(9):2175–2188, 2008.

[113] L. Sharifian, Y. M. Wright, K. Boulouchos, M. Elsener, and O. Kröcher. Simulation of nox reduction in an ammonia-scr system with an fe-zeolite catalyst and calibration of related parameters. In *ASME Conference Publications*, 2010.

[114] L. Sharifian, Y. M. Wright, K. Boulouchos, M. Elsener, and O. Kröcher. Transient simulation of nox reduction over a fe-zeolite catalyst in an nh3-scr system and study of the performance under different operating conditions. *SAE Technical Paper*, 2011-01-2084, 2011.

[115] X. Song, G. Parker, J. Johnson, and J. Naber. A modeling study of scr reaction kinetics from reactor experiments. *SAE Papers*, 2013-01-1576, 2013.

[116] S. Stadlbauer, H. Waschl, and L. del Re. Scr ammonia dosign control by a nonlinear model predictive controller. In *Proceedings of the 19th World Congress of the International Federation of Automatic Control*, 2014.

[117] S. Stadlbauer, H. Waschl, and L. del Re. Adaptive scr model for mpc control including aging effects. *SAE Technical Paper*, 2015-01-1045, 2015.

[118] S. Stadlbauer, H. Waschl, and L. del Re. Black box scr modeling and control for small ci engines. *IFAC-PapersOnLine*, 49(11):28–33, 2016.

[119] T. Su, C. Chang, R. Reitz, and P. Farrell. Effects of injection pressure and nozzle geometry on spray smd and d.i. emissions. *SAE Technical Paper*, 952360, 1995.

[120] N. Y. Topsoe, T. Slabiak, B. S. Clausen, T. Z. Srnak, and J. A. Dumesic. Influence of water on the reactivity of vanadia/titania for catalytic reduction of nox. *Journal of Catalysis*, 134:742, 1992.

[121] K. Toyoda, W. Ibabashi, N. Iiyama, and Y. Seo. The quantitative analysis of multi-reactions on scr process. *Studies in Surface Science and Catalysis*, 121:363–366, 1999.

[122] E. Tronconi, A. Cavanna, and P. Forzatti. Unsteady analysis of no reduction over selective catalytic reduction - de-nox monolith catalysts. *Industrial & Engineering Chemistry Research*, 37:2341–2349, 1998.

[123] E. Tronconi, L. Lietti, P. Forzatti, and S. Malloggi. Experimental and theoretical investigation of the dynamics of the scr-de-nox reaction. *Chemical Engineering Science*, 51:2965–2970, 1996.

[124] E. Tronconi, I. Nova, C. Ciardelli, D. Chatterjee, B. Bandl-Konrad, and T. Burkhardt. Modelling of an scr catalytic converter for diesel exhaust after treatment: Dynamic effects at low temperature. *Catalysis Today*, 105:529–536, 2005.

[125] D. Tsinoglou, O. Haralampous, G. Koltsakis, and Z. Samaras. Model-based optimization mmethod of combined dpf-scr systems. *SAE Technical Paper*, 2007-01-0098, 2007.

[126] T. L. Ullman, L. R. Smith, J. W. Anthony, W. J. Slodowske, B. Trestrail, A. L. Cook, W. B. Bunn C. A. Lapin, K. J. Wringht, and C. R. Clark. Comparison of exhaust emissions, including toxic air contaminants, from school buses in compressed natural gas, low emitting diesel, and conventional diesel engine

configurations. *SAE Papers*, 2003-01-1381, 2003.

[127] J. Vardi and W. F. Biller. Thermal behaviour of exhaust gas catalytic convertor. *Industrial & Engineering Chemistry Process Design and Development*, 7:83–90, 1968.

[128] I. E. Wachs, G. Deo, B. M. Wechhuysen, A. Andreini, M. A. Vuurman, M. de Boer, and M. D. Amiridis. Selective catalytic reduction of no with NH_3 over supported vanadia catalysts. *Journal of Catalysis*, 161:211–221, 1996.

[129] D. Y. Wand, S. Yao, M. Shost, J. Yoo, D. Cabush, and D. Racine. Ammonia sensor for closed-loop scr control. *SAE Papers*, 2008-01-0919, 2008.

[130] David H. West, Vemuri Balakotaiah, and Zoran Jovanovic. Experimental and theoretical investigation of the mass transfer controlled regime in catalytic monoliths. *Catalysis Today*, 88:3–16, 2003.

[131] B. Westerberg, C. Knunkel, and I. Odenbrand. Transient modelling of a hc-scr catalyst for diesel exhaust aftertreatment. *Chemical Engineering Journal*, 47(1-3):27–39, 2003.

[132] A. Widd and M. Lewander. Efficient exhaust gas aftertreatment solutions for eu iv and beyond. *SAE Technical Paper*, 2015-26-0103, 2015.

[133] M. Wiebel, V. Schmeißer, and F. Hofmann. *Urea-SCR Technology for deNOx After Treatment of Diesel Exhasts, Chapter 22*. Springer, 2014.

[134] F. Willems, R. Cloudt, E. van den Eijnden, M. van Genderen, R. Verbeek, W. Boomsma B. de Jager, and I. van den Heuvel. Is closed-loop scr control required to meet future emission targets? *SAE Papers*, 2007-01-1574, 2007.

[135] R. Willi, B. Roduit, R. A. Koeppel, A. Wokaun, and A. Baiker. Selective reduction of no by nh3 over vanadia-based commercial catalyst: Parametric sensitivity and kinetic modelling. *Chemical Engineering Science*, 51:2897–2902, 1996.

[136] Jimmie L. Williams. Monolith structures, materials, properties and uses. *Catalysis Today*, 69:3–9, 2001.

[137] A. P. E. York, T. C. Watling, J. P. Cox, I. Z. Jones, A. P. Walker, P. G. Blakeman, T. Ilkenhans, R. Allansson, and M. Lavenius. Modeling and ammonia scr denox catalyst: Model development and validation. *SAE Technical Paper*, 2004-01-0155, 2004.

[138] X. Yuan, H. Liu, and Y. Gao. Diesel engine scr control: Current development and future challenges. *Emission Control Science and Technology*, 1:121–133, 2015.

[139] B. K. Yun and M. Y. Kim. Modeling the selective catalytic reduction of nox by ammonia over a vanadia-based catalyst from heavy-duty diesel exhaust gases. *Applied Thermal Engineering*, 50:152–158, 2013.

[140] G. Zanardo, S. Stadlbauer, H. Waschl, and L. del Re. Grey box control oriented scr model. *SAE Technical Paper*, 2013-24-0159, 2013.

[141] Ming Zheng, Graham T. Reader, and J. G. Hawley. Diesel engine exhaust gas recirculation - a review on advanced and novel concepts. *Energy Conversion and Management*, 45:883–900, 2004.

Department of Chemical and Biochemical Engineering
Technical University of Denmark
Søltofts Plads, Building 229
2800 Kgs. Lyngby
Denmark

Phone: +45 45 25 28 00
Web: www.kt.dtu.dk/